2019

Ultra-High Performance Concrete for Precast Seismic Bridge Column Connection

Titchenda Chan
University of Central Florida

ULTRA-HIGH PERFORMANCE CONCRETE FOR PRECAST SEISMIC BRIDGE COLUMN CONNECTION

by

TITCHENDA CHAN
B.S. Institute of Technology of Cambodia, 2008
M.S. University of Central Florida, 2014

A dissertation submitted in partial fulfilment of the requirements
for the degree of Doctor of Philosophy
in the Department of Civil, Environmental and Construction Engineering
in the College of Engineering and Computer Science
at the University of Central Florida
Orlando, Florida

Summer Term
2019

Major Professor: Kevin R. Mackie

ABSTRACT

Accelerated bridge construction (ABC) utilizes prefabricated bridge elements constructed off-site, delivered, and assembled on-site to expedite construction time and reduce traffic disruption. ABC has been increasingly used for super- and sub-structure elements in low seismic regions. However, its application in medium and high seismic regions remain limited, particularly for precast columns where connections typically coincide with plastic hinge (PH) regions. Ultra-high performance concrete (UHPC), characterized by high compressive and tensile strength, and superior bond properties, is a potential material that can mitigate PH damage and enhance load transfer. This research proposes a new and simple damage tolerant precast column connection for use in medium and high seismic regions. The connection laps the column longitudinal reinforcement with footing dowels using a short splice length, a practical concrete cover, no shear reinforcement, and the shifted PH concept to prevent footing damage. Two 0.42-scale precast columns with different shear span ratios were tested under reversed cyclic loading to investigate the proposed connection relative to previously tested cast-in-place specimens. Results showed the connection performed well in shear, developed column longitudinal bars, shifted PH formation above the UHPC connection, and exhibited high lateral capacity and ductility. Twenty-seven pullout and lap splice beams were tested to study the bond of reinforcement in UHPC under different parameters and stress states. Results indicated significant bond strength improvement and splice length reduction compared with conventional concrete. The pullout specimens were simulated using the OpenSees framework to propose reinforcing steel in UHPC bond-slip models where existing studies in the literature were limited. The models were incorporated into the numerical modeling of the precast columns using one-dimensional fiber-section and two-dimensional plane stress nonlinear analyses. Results from the two modeling methods showed good agreement with the experiments, with the calibrated bond-slip models providing a good

representation of load transfer in the connection.

To my beloved mother,

who has always offered me with her unconditional love, encouragement and supports.

ACKNOWLEDGMENTS

First, I would like to express my sincere gratitude to my academic advisor, Dr. Kevin R. Mackie, for his invaluable guidance, continuous support, and sharing of extensive knowledge. This dissertation would not be possible without his mentorship. I would like to thank the dissertation committee members, Dr. Necati Catbas, Dr. Manoj Chopra, and Dr. Yuanli Bai for their time, constructive comments and essential suggestions.

King Construction Products are thanked for donating UHPC materials. The technical assistance from Julian Pena Cruz during the construction of the UHPC connection is greatly appreciated. The author thanks MMFX Technologies for providing high strength reinforcing steel. The author would like to thank Neptune Research Inc. for the opportunity to work on the fiber-reinforced polymers for concrete strengthening project that was also conducted during the time at UCF.

Special thanks are expressed to my friends and colleagues Kushal Nagarsheth, Bolivar Perez, Lianne Brito, Yousef Alhabi, and Mohammad Khawaji for spending a great amount of their time, always with high motivation, to help finish the laboratory work. The thank also goes to the lab coordinator, Mr. Yeong-Ren Lin, for his technical assistance and kindness that made the construction and testing of the experimental specimens possible.

TABLE OF CONTENTS

LIST OF FIGURES

LIST OF TABLES

CHAPTER 1: INTRODUCTION

1.1 Background

Infrastructure repair and renewal in the US is a multi-billion dollar endeavor, costing the US government approximately $17.5 billion in 2012 alone. According to the 2017 ASCE report card, 9.1% of bridges were structurally deficient and 13.6% were functionally obsolete in 2016. More importantly, while current federal estimates place the nation's backlog of bridge rehabilitation needs at $123 billion, the cost is projected to substantially increase [1]. The bridge rehabilitation requires extensive construction that would cause road closure, traffic congestion, and traffic delay. To put travel interruption in perspective, a recent report issued by INRIX indicated that America lost $87 billion in time annually due to traffic congestion [2].

Typical bridge construction in the US employs conventional cast-in-place (CIP) reinforced concrete (RC) components. CIP construction requires time-consuming procedures such as shoring, formwork construction, reinforcement placement, and concrete pouring and curing. If the upcoming bridge construction is to follow these conventional practices, traffic congestion and its indirect cost will significantly increase. These challenges require stakeholders and engineers, such as federal transportation agencies, researchers, engineers, and contractors, to develop the more innovative and cost-effective techniques. Accelerated bridge construction (ABC) has become popular in bridge construction in the past decade. ABC is the use of prefabricated bridge elements and systems (PBES) constructed off-site, delivered, and assembled on-site to reduce traffic disruption, expedite construction time, increase quality control, and provide promising cost-effective long-lasting bridge. The idea of precast modular solutions for bridge construction started over 50 years ago with the use of prestressed bridge girders, but has since evolved to other precast elements such as deck, pier,

abutment, wall, parapet, spread footing, column and bent-cap [3].

The existing precast super- and sub-structure options have been mostly used in low seismic regions, while applications and technologies in medium and high seismic regions (particularly for precast columns) have seen limited use. Challenges include the lack of design and construction specifications and uncertainty in seismic performance of substructure connections under high seismic loading [4]. Connections of precast column-to-footing and precast column-to-bent cap typically coincide with the plastic hinge (PH) regions, where maximum moment, inelastic deformation, high strain penetration and major damage occur during a high seismic event. To mitigate the damage and accommodate the high nonlinear behavior due to the reversed cyclic loading, the connections are required to exhibit high energy dissipation and high ductility capacity. A number of connections have been proposed that show good seismic performances but can have complex operation techniques.

Advancements in concrete materials technology provide an ideal opportunity to enhance the seismic performance of precast bridge substructure connections. Ultra-high performance concrete (UHPC) is one such advancement that has gained substantial interest from researchers and design professionals. UHPC are characterized by high compressive and tensile strength, excellent durability, and high ductility. The material also exhibits superior bond properties that significantly reduce rebar embedment and splice length. UHPC has been used in various civil-structural applications (Fig. 1.1) such as the first pedestrian bridge in Canada [5], arch bridge in South Korea [6], overpass bridge in France [7], and the first highway bridge in Wapello County, Iowa, US [8]. Investigations on the use of UHPC fall into a broad range of topcis including beams without transverse reinforcement, composite decks, bridge piles, and wind turbine towers. Most recently, UHPC is commonly used in specific locations, such as connections between precast superstructures due to its initial high cost [10].

(a) Sherbrooke pedestrian bridge [9]

(b) Footbridge of Peace, Seoul [9]

(c) Bourg-Les-Valence overpass bridge [7]

(d) The Mars Hill bridge, Wapello County [8]

Figure 1.1: UHPC for various civil-structural applications

1.2 Previous Research on ABC Substructure Connections in Seismic Regions

In recent years, various precast substructure connections, both emulative and non-emulative, have been developed and evaluated for use in medium and high seismic regions [11]. Emulative connections allow the precast concrete systems to mimic the CIP systems. The connections include grouted duct, pocket, member socket, and bar coupler connections. Past investigations have shown that these connections allow precast columns to exhibit acceptable seismic behavior and comparable performance to geometrically similar cast-in-place (CIP) bridge columns. However, the connections can require large rebar embedment lengths or tight construction tolerances. On the other hand, the precast concrete systems with non-emulative connections (also called hybrid connections) do not emulate the CIP systems. The connections were developed to minimize damage and reduce residual drift of precast column.

1.2.1 Bar Coupler Connections

Bar coupler connections provide direct load transfer from one bar to another using a mechanical coupler. This allows resemblance of reinforcement details between precast column using bar coupler and the conventional CIP column. Several couplers are commercially available in the US market including threaded sleeve, headed bars with separate sleeves, external clamping screws, and grouted sleeves (GS), among which GS coupler has gained the most attention because it provides good construction tolerance. In recent years, the use of bar coupler for substructure connection in moderate and high seismic regions have been extensively studied.

Haber et al. [12] investigated the seismic behavior of two different coupler connections, headed bar and GS, through experimental testing of four half-scale precast columns subjected to slow reversed-cyclic loading using cantilever test setup. Each coupler type was

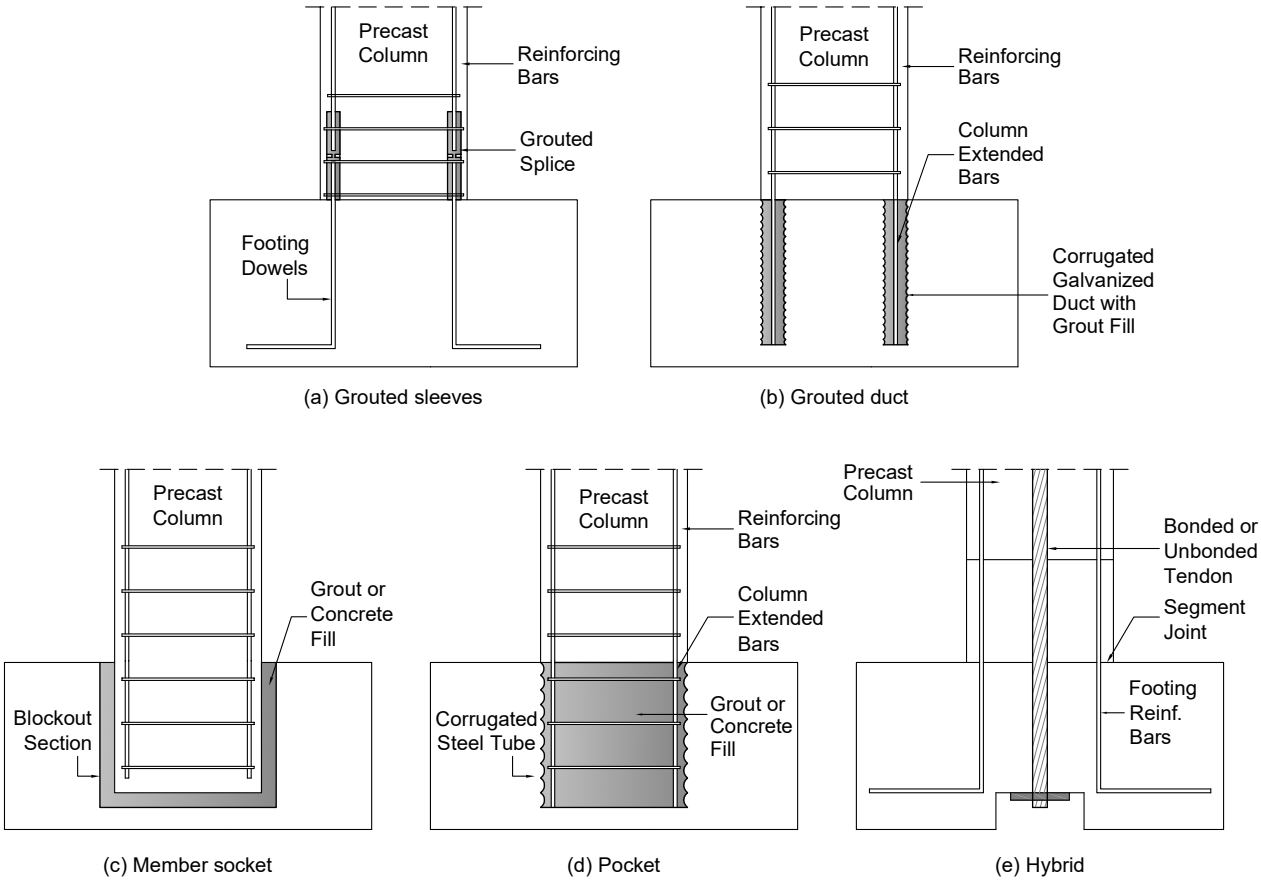

Figure 1.2: Emulative columns utilizing UHPC

incorporated into two column models. In the first model, the precast column was connected directly to the precast footing. The second model comprised of a precast pedestal between the column and footing, which was utilized to reduce moment demand in the PH region. Responses of the precast columns were compared with a reference conventional CIP column. Results indicated that all four precast columns exhibited similar lateral load capacity, damage progression, and energy dissipation to the CIP column. However, three of the precast columns experienced reduction of displacement ductility between 28% to 36% due to the large strain concentration at the column-footing interface and the disrupted PH created by additional stiffness of the precast pedestal and GS couplers. Similar reduced ductilities up to

40% were observed in the study of seismic performance of GS connections located at different regions of three half-scale precast columns by Ameli et al. ([13] and [14]). The GS connectors were placed inside the PH region of two precast columns with and without debonding in the footing (denoted GGSS-1 and GGSS-3, respectively), and inside the footing of the third column (GGSS-2). Results showed consistent damage patterns between CIP column and GGSS-2, while debonding in the footing improved ductility of the precast columns from $\mu = 5.4$ for GGSS-1 to μ =6.8 for GGSS-3.

Tazarv et al. [15] improved the seismic performance of GS connection by debonding the longitudinal PH reinforcement within CIP pedestal to increase the plastic rotation capacity of the PH. The precast column only exhibited a 15% reduction in displacement ductility compared with a CIP column. Haber et al. [16] used a shifted plastic hinging (SPH) design concept with GS connection to relocate PH formation above the connection region. The precast columns were designed to reduce strain concentration at the column-footing interface and maintain linear elastic performance of the footing utilizing high-strength steel as footing dowels. The connection further improved ductility and reduced footing damage compared with previous studies on GS connections.

1.2.2 Grouted Duct Connections

In a grouted duct (GD) connection, each extending bar of a precast element is inserted into a separate galvanized steel duct that was encased inside the other member prior to filling with cementitious grout. Different from bar coupler connection where stress is transferred from one bar to another, stress of the extending bar in GD connection is transferred to the surrounding hardened grout, which in turn, transfers stress to the outside of the duct. GD connection may require shorter splice length than CIP column due to the confinement offered by galvanized steel duct. The connection provides larger construction tolerance compared with GS connection, but requires larger space in the reinforcement cage of the adjacent

precast element.

Matsumoto et al. [17] initially conducted a series of pullout test and a full-scale CIP column-bent test to study the non-seismic performance of GD connection. The pullout test used #11 epoxy-coated rebar grouted inside a 4-in diameter steel corrugated duct under different embedment depth, grout brand and bar anchorage. Results from the component-level test indicated that GD was able to develop both the epoxy-coated straight and upset-headed #11 bars with the embedment length of $13d_b$. The different bar anchorage did not appear to provide benefit at the embedment length required for bar yield. GD responses including cracking, load-slip, and loading capacity were affected significantly by grout strength and brand. The general behavior of GD in pullout test was characterized by a well-distributed stress along the bar length accompanied by splitting cracks in the surrounding concrete and pullout of bar-grout mass from the duct at failure. No slip at the duct-concrete interface was observed. Results from the full-scale column-bent test showed that the use of GD with straight bars having $13d_b$ of embedment length provided similar strength and ductility to a conventional CIP column. At failure, no splitting cracks was observed in the grouted ducts and slip was minor. Matsumoto [18] further investigated the seismic performance of GD connection by testing a 0.42-scale precast column-bent specimen under quasi-static force control and displacement control sequences in comparison with a benchmark CIP column. Results showed that the precast specimen exhibited stable hysteretic response without significant strength and stiffness degradation. The precast specimen failed at 5.2% drift with ductility μ=8 compared with 5.9% drift and μ=10 of CIP column.

Pang et al. [19] tested three 0.4-scale precast column-to-cap beam specimen and a geometrically comparable CIP specimen to evaluate the seismic performance of GD connection. The precast columns comprised of 12 #3 and 6 #8 longitudinal bars, yet to allow faster erection and better field tolerance only the 6 large bars were inserted and grouted inside cap beam. Two precast specimens were debonded $8d_b$ long at the column-beam interface and

another is fully bonded. Results indicated that all four columns exhibited very similar behavior in terms of energy dissipation and force-deformation relationship in which lateral load began to drop at 5% drift at the onset of bar buckling and fracture. A noticeable difference between the precast and CIP specimens was the damage progression where localized flexural cracks were concentrated at the beam-column interface for all three precast specimens, while uniformly distributed cracks were observed on CIP columns. Debonding did not appear to produce changes to the responses of the precast specimens.

1.2.3 Pocket Connection

Pocket connections require the extending bars from a precast column to be inserted into a single pocket of another element such as footing or cap beam. The pocket is subsequently filled with CIP concrete or grout. Force between elements is transferred from the reinforcing bars to the surrounding concrete and the pocket perimeter through bond. Extensive studies have been conducted on pocket connections, one of which was the investigation by Restrepo et al. [4]. Two types of pocket connections CPFD and CPLD were studied. CPFD was designed to have high ductility intended to be applied in high seismic regions, while CPLD was designed for low to moderate seismic regions. CPFD specimen had higher reinforcement ratio both in the joint and bent cap than CPLD specimen. Two 0.42 bent-cap specimens were tested under cyclic loading to study connections. Results indicated that both precast specimens exhibited similar responses to a CIP specimen with stable hysteresis loops, high displacement ductility (μ=8 compared with μ=10 for CIP), insignificant strength and stiffness degradation, but with exception of damage patterns. CPFD failure was characterized by concentrated PH damage at the column-bent cap interface and minor joint and cap beam damage. CPLD specimen experienced less critical PH damage at the column-bent cap interface but exhibited critical shear crack in the joint and cap beam.

Mehraein [20] investigated two 0.27-scale two-column bent subjected to earthquake

load using a shake table test. The columns were connected at the top to a post-tensioning precast cap beam incorporating pocket connections and at the bottom to pedestals that simulated pile-shafts. Two pin connections were used at the column base to eliminate bending moment demand including pipe-pin connections and rebar-pin that were used on a separate two-column bent specimen. Good seismic performance was observed on both specimens in which the post-tensioning cap beam exhibited elastic performance.

1.2.4 Member Socket Connection

Member socket connections are constructed by embedding an entire precast member inside an adjacent member. The adjacent member either incorporates a preformed socket to be filled with grout or concrete, or reinforcement cage to be casted entirely. Its applications and force transfer are similar to pocket connections. Sufficient embedment length in the connection is required and necessary to fully develop the precast member. Haraldsson et al. [21] tested three 0.42-scale precast columns connected to CIP footings to evaluate the performance of socket connection. All three precast columns had the same reinforcement and geometry, but depth and reinforcement of the footings were varied. The first two columns (SF-1 and SF-2) were inserted into CIP footings that had the same embedment length of 1.1 times column diameter, but different reinforcement ratio. The third column was embedded into a shallow footing with depth of one-half column diameter. The specimens were subjected to axial load and cyclic loading. The three specimens showed promising seismic performance. SF-1 and SF-2 displayed similar hysteretic behavior with noticeable strength drop at the drift ratio of 7%, and similar damage progression where PH formed above the interface, the footings exhibited minor cracks, but no sign of damage on the connection. On the other hand, SF-3 showed degraded strength after 2.5% drift, yet the drop was gradual. Damage on the footing of SF-3 was critical and at failure punching shear occurred.

Mehrsoroush and Saiidi [22] investigated a 0.33-scale two-column bent subjected to

cyclic loading. The columns were connected at the top to a post-tensioned precast cap beam incorporating socket connections and at the bottom to pipe-pin connections. Good seismic performance was observed. The bent failed at 10.3% drift having a displacement ductility of 8.7. PH was developed below the cap beam which remained under elastic performance. Only minor damage was observed at the column base assisted by the use of pipe-pin connection. A shake table test was conducted by Motaref et al. [23] on a two-column bent that was connected to the footing using socket connections. The PH region of one column was constructed with engineered cementitious composite and another with a concrete-filled fiber reinforced polymer tube. The bent exhibited a large displacement capacity with no damage observed in the connection.

1.2.5 Hybrid Connection

Hybrid connections use hybrid actions of an unbounded prestressing tendon, mild steel reinforcement and other energy-dissipating materials such as fiber-reinforced concrete or high-performance concrete in the plastic hinge region. Each material in this connection provides distinguished benefits for seismic performance. The unbonded prestressing tendons gives a self-centering mechanism, provides equal strain distribution to avoid critical strain concentration and ensures elastic behavior of the tendon. This minimizes residual drift after a seismic event. Meanwhile, mild steel reinforcement placed in the PH region increases energy dissipation of the column. Although the concept of hybrid connections work in laboratory setting, its application on site is still questioning and requires further investigation. Several drawbacks of these connections include the time-consuming operation for on-site post-tensioning, difficulty in installing anchorages at the footing, and the corrosion of unbonded tendons.

Restrepo et al. [4] tested three hybrid column-bent specimens under cyclic loading. All specimens incorporated unbonded post-tensioning tendons at center of the columns.

The first specimen HYB1 used reduced longitudinal reinforcement with conventional spiral at column end. The second specimen HYB2 used a full-height steel shell with conventional longitudinal reinforcement only inside the column head and extended slightly inside the shell. The third specimen HYB3 was similar to HYB2 but incorporated additional RC shell. Results of the three hybrid bents were compared with a CIP specimen. All hybrid specimens exhibited higher lateral load capacity than the CIP bent, which was contributed by the post-tensioning tendons. HYB1 appeared to have more stable hysteretic response with significant load drop only at failure. HYB2 and HYB3 exhibited gradual lateral capacity reduction after 2% drift. However, all three specimens were able to undergo lateral displacement until 6% drift. At failure, all hybrid specimens exhibited significantly lower residual drift and damage compared with the CIP specimen and were dominated with localized end rotation at the bedding layer. Other investigations on hybrid bridge column specimens that showed high displacement capacity, minimal residual drift and minimal PH damage include Marriott et al. [24] and Yamashita and Sanders [25].

1.3 Previous Research on Seismic Substructure Using UHPC

The development of UHPC and seismic substructure connections are both recent topics. The use of UHPC for substructure connections in high seismic regions is therefore very limited. However, with high strength, excellent confinement, and superior bond properties that satisfy the required material characteristics subjected to seismic loading, UHPC has been utilized in the investigations of seismic precast column and pier connections in both emulative and non-emulative systems by a number of researchers. Those investigations mainly utilized this innovative material in the PH region to minimize the critical damage observed in previously developed seismic connections, and to improve displacement ductility capacity of the substructure elements.

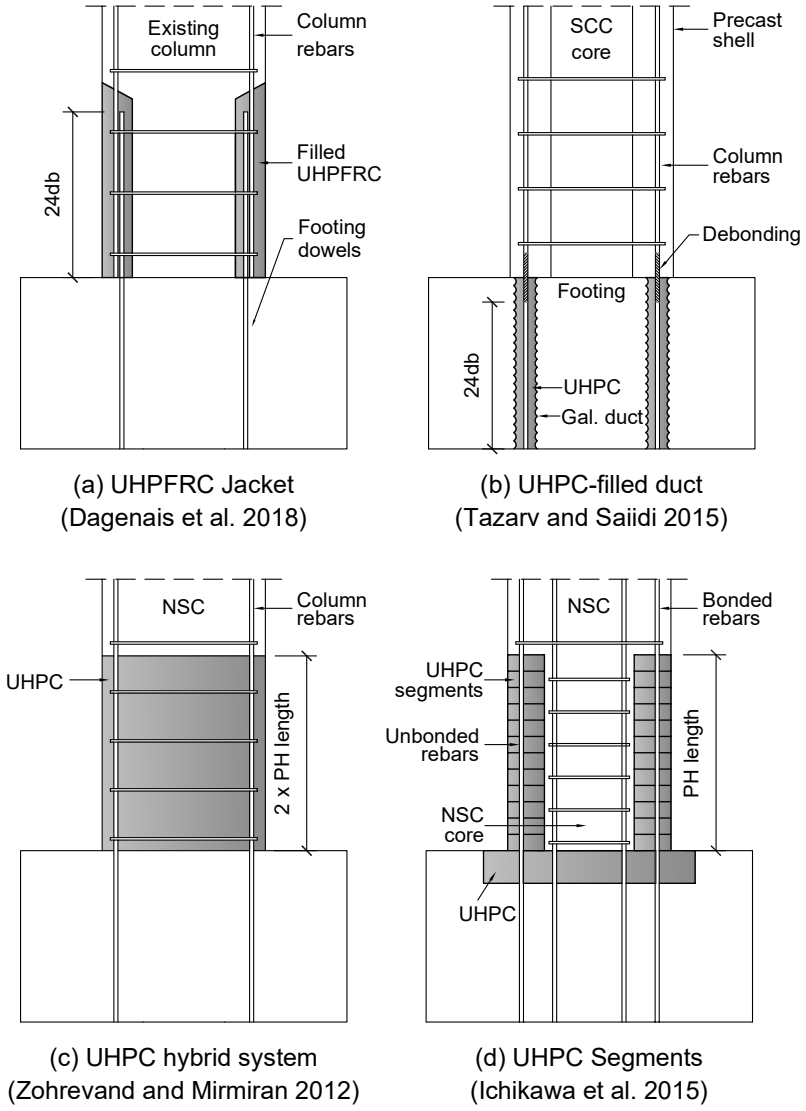

Figure 1.3: Emulative columns utilizing UHPC

1.3.1 Emulative Systems Utilizing UHPC

It is evident since the earthquake event in 1970 that most existing bridge columns and piers incorporating lap splice details were not adequately designed to resist high seismic loading. This requires the repair or replacement of the bridge elements, in particular for rectangular bridge pier where conventional retroffiting techniques such as steel or FRP jackets

to increase concrete core confinement are ineffective. Vachon and Massicotte [26] proposed the use of SFRC with 1.2 in (30 mm) long hook fibers to replace the removed concrete portion for a 4:1 rectangular column. The technique was effective but significant removal of cover and core concrete was required. Dagenais et al. [27] proposed similar jacketing technique using ultra-high performance fiber reinforced concrete (UHPFRC) with 3% of steel fibers as a retrofitting material. Only a distance of one rebar diameter (d_b) behind the splice bars of normal strength concrete (NSC) was demolished to be replaced with UHPFRC. Rebar splice length of $24d_b$ was used. In the first phase, two 79 x 20 in (2000 x 500 mm) bridge piers (one control specimen designed to support gravity load and one retrofitted) were tested. The control specimen displayed almost no ductility and experienced brittle failure due to the loss of bond and critical splitting cracks in the spliced region. On the other hand, the retrofitted pier prevented splitting cracks, exhibited displacement ductility of 4.6, allowed PH formation at the pier base, and shifted the failure mode to rebar fracture. Four additional full-scale rectangular piers with different rebar sizes designed based on modern seismic requirements were retrofitted with the same UHPFRC jacketing method and tested under cyclic loading. The specimens obtained displacement ductility between 6.8 and 8. Minor damage on UHPFRC portion and no concrete cover spalling were observed.

To allow application of filled duct connection between precast column and footing where rebar embedment length is small, Tazarv and Saiidi [28] proposed the use of UHPC having compressive strength f'_c of 22.97 ksi (158.4 MPa) as the filled material. The embedded length of #25 rebar in the connection was 24 d_b. NSC with f'_c of 3.29 and 5.48 ksi (22.7 and 37.8 MPa) was used for the precast column shell and precast footing, respectively. Self-consolidating concrete with $f'_c = 9.51$ ksi (65.6 MPa) was utilized to fill the column core after the column shell was connected to the footing. The column was reinforced longitudinally with grade 60 normal strength (NS) steel and transversely with #10 spiral. Column longitudinal bars were debonded at a distance of $8d_b$ at the column-footing interface to reduce strain

concentration. The precast column was compared to a reference CIP column. Results showed that the precast column was emulative to the conventional CIP column, achieving almost the same lateral load capacity and similar displacement ductility of 6.30 compared with 7.36 of CIP column. No damage of UHPC-filled duct connection was observed. Tazarv and Saiidi [29] also implemented the UHPC-filled duct connection on a precast column having the same geometry to the previous column, yet NSC and NS rebar in PH region were replaced with engineered cementitious composite (ECC) and shape memory alloy (SMA), respectively. The precast column was able to reach 12% drift ratio with no damage in the UHPC-filled duct connection observed. ECC and SMA were effective in reducing damage in the PH region and residual displacement, respectively.

UHPC was utilized in two quarter-scale columns studied by Zohrevand and Mirmiran [30]. Both columns used UHPC within twice the PH length and conventional concrete for the remaining portion. The first column (RUHPC) used NS reinforcement within the two concrete materials, while the second column (UHPCFFT) encased the two concrete materials by a fiber reinforced polymer (FRP) tube and eliminated the use of NS reinforcement. The two columns were also compared with a conventional RC column and an unreinforced concrete column encased by an FRP tube. RUHPC, UHPCFFT, and RC columns exhibited displacement ductilities of 4.8, 3.0, and 5.4, respectively. Although the use of UHPC in PH region can significantly increase strength and initial stiffness, and minimize damage in PH region, the high compressive strength of UHPC may prevent the material from attaining the full dilation and crushing strain capacity, resulting in reduced displacement ductility.

Two 1/5-scale energy-dissipating columns were investigated by Ichikawa et al. [31]. The columns comprise of a solid RC core encased by 12 dry-joint 2-in (50 mm) thick hallow UHPC segments in the PH region. Thirty-six unbonded NS rebars were inserted inside the pre-formed holes around UHPC segments. The unbonded NS rebars and UHPC segmental jackets were utilized avoid strain concentration and minimize the PH damage when subjected

to extreme ground motion. The first and second columns were tested with bilateral cyclic loading (RC-UHPC) and hybrid loading that simulated the 1995 Kobe Earthquake (HY-UHPC), respectively. The columns showed good performance under both seismic loading scenarios. RC-UHPC was able to carry up to 6.5% drift with minor UHPC segments spalling. Damage up to 2.1 in (53 mm) in the RC core was observed and failure occurred due to rebar fracture. On the other hand, HY-UHPC reached 7.8% drift at North-South direction and 11.1% in the East-West direction before failure. Failure occurred due to crushing of UHPC bottom segments and rebar fracture. The damage of both columns was also attributed to the twisting effect of bilateral loading and gap opening of the UHPC segments.

1.3.2 Non-emulative Systems Utilizing UHPC

In addition to the RC-UHPC and HY-UHPC columns, Ichikawa et al. [31] tested a 1/5-scale non-emulative column (PC-UHPC) that incorporated the same UHPC segment configuration in the PH region but without the RC core. The UHPC segments with unbonded rebar was combined with unbonded post-tensioning rebar at the center of the column. Friction between UHPC segments generated by the post-tensioning force provided additional shear strength to the column. The column was subjected to same bilateral cyclic loading as the RC-UHPC column. PC-UHPC column suffered significant torsion and failed at 3.5% drift when the UHPC was crushed at the bottom segment.

Yang and Okumus [32] utilized precast UHPC segment to eliminate damage of post-tensioned self-centering precast piers. Three large-scale precast segmental piers were tested under quasi-static cyclic lateral loading. Each specimen consisted of five 25 x 25 x 24 in (635 x 635 x 610 mm) precast segments that incorporated ducts for post-tensioned tendons. Four of the precast segments were constructed using the conventional concrete with NS rebars. The bottom precast segment above the footing surface was the only varying detail between the three specimens. Two specimens used UHPC with and without NS reinforcement

and another used conventional concrete with NS reinforcement. The hysteretic responses and damage patterns between the three specimens were compared. Yang and Okumus [32] concluded that all three rocking columns exhibited good seismic performance exceeding the seismic demands, and residual displacement remained less than 20% at failure . The use of UHPC, both with and without NS rebars, increased pier strength and stiffness. Damage of both reinforced and unreinforced precast UHPC segments were limited to 4% of the segment height indicating that no repair and no reinforcement is required. On the other hand, the conventional concrete segment experienced significant cover spalling and edge crushing up to 40% of the segment height.

Mohebbi et al. [33] combined the use of UHPC up to $80d_b$ high in PH region and unbonded carbon fiber-reinforced polymer (CFRP) as post-tensioned tendons in a shake table study of a large-scale precast bridge column connected to a precast footing via pocket connection. UHPC successfully prevented PH major damage and yielding of mild reinforcement in the NSC region. The column reached a maximum drift ratio of 6.9% corresponding to a displacement ductility of 13.8 and 200% design earthquake. The column failed due to fracture of longitudinal bars at the footing-column interface. Residual displacement was negligible.

1.4 High-Performance Materials

Conventional concrete and NS reinforcing steel remain largely used for CIP elements in building and infrastructure construction. However, as the design and construction methods are shifted to the modern accelerated construction, advanced materials are required. This study utilized two high-performance materials including UHPC and HS reinforcing steel. Mechanical properties and past research on the two materials are briefly described.

1.4.1 Ultra-High Performance Concrete

1.4.1.1 Definition and Constituents

UHPC-class materials are characterized by high compressive strength, 22 ksi (150 MPa) and above, high tensile strength, and excellent durability properties. UHPC-class materials are commonly reinforced with high volume fractions (between 2% and 4%) of high-strength steel fibers. UHPC uses finely graded granular materials and low water-to-cement ratio (0.2) to help promote the high compressive strength and durability. The granular materials including fine sand, cement, and crushed quartz have an average dimension between 0.006 and 0.0236 in (150 and 600 μm), 0.0006 in (15 μm), and 0.0004 in (10 μm), respectively. Void spaces between aggregates are filled by silica fume. Super-plasticizer is utilized to obtain better workability. Steel fiber reinforcement can have a nominal length of 0.5 to 1.18 in (12.7 to 30 mm), nominal diameter of 0.008 to 0.022 in (0.2 to 0.55 mm), and tensile yield strength between 160 and 399 ksi (1100 to 2750 MPa) [34]. Steel fibers are used to increase tensile strength and allow extensive post-cracking tensile ductility prior to discrete crack localization.

Multiple types of UHPC are commercially available in North America and European markets. Haber et al. [34] evaluated five different UHPC-class materials. The UHPC used in this research is UP-F2 developed by King Packaged Materials Company [35] containing constituents as listed in Table 1.1 and depicted in Fig. 1.4. The constituents necessary for batching of UP-F2 supplied by the manufacturer include: a pre-blended and pre-packaged dry powder that contain all granular materials, two types of liquid admixture, and steel microfiber reinforcement with individual fiber having a nominal length and diameter of 0.5 in (13 mm) and 0.008 in (0.2 mm), respectively and a tensile strength of 399 ksi (2750 MPa).

Table 1.1: UHPC constituents (UP-F2)

Constituents	lb/yd^3	kg/m^3
Prepackage dry components (premix)	3223.9	1912.6
Water and/or ice	331.1	196.4
Liquid admixture "A"	80.8	48.0
Liquid admixture "B"	42.4	25.1
Steel fibers	263	156
Total mass	3941.2	2338.1

Note: Steel fiber is 2% of volume fraction

(a) UHPC dry component

(b) Steel fiber

(c) Admixture A

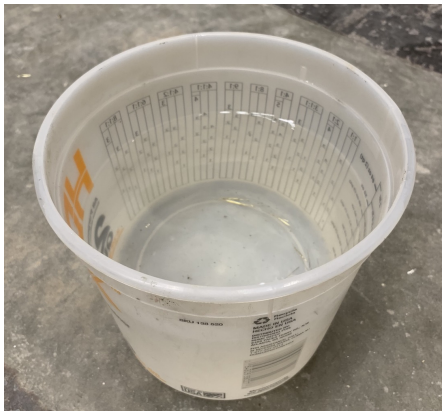

(d) Admixture B

Figure 1.4: UHPC constituents

1.4.1.2 Mixing Procedures

Different classes of UHPC may require different mixing procedures. The UHPC used in this study was mixed following the mixing procedures as listed in Table 1.2. The total mixing time per batch varied between 17 and 19 minutes.

Table 1.2: UHPC mixing procedures

Step	Constituent to introduce	Action	Mixer speed	Start (min)	End (min)
1	UP-F2 Poly premix	Start mixer and introduce UP-F2 Poly premix bags	Low	-	-
2	-	Mix (30 seconds)	Low	0:00	0:30
3	50% of mixing water & 100% of Admixture A	Slowly introduce the water and Admixture A (blended) into the mixer during mixing (30 seconds)	Low to medium	0:30	1:00
4	50% of mixing water	Slowly introduce the remainder of the water (30 seconds)	Medium to high	1:00	1:30
5	-	Mix (3 minutes)	High	1:30	4:30
6	100% of Admixture B	Slowly introduce Admixture B (30 seconds)	High	4:30	5:00
7	-	Mix (1 minute)	High	5:00	6:00
8	Steel fibers	Gradually add the steel fibers at a rate of 15 Kg-20 Kg per minute (33lb-44lb per minute)	High	6:00	7:00
9	-	Continue mixing (3 minutes)	High	7:00	10:00
10	-	Stop the mixer and check for homogeneity. Scrape off the mixer paddles and tank (3 minutes)	-	10:00	13:00
11	-	Restart the mixer and continue mixing until a homogeneous mixture is obtained (min. 4 minutes; max. 6 minutes)	High	13:00	17:00 to 19:00

1.4.1.3 Compressive Strength and Elastic Modulus

Compressive strength of UHPC was investigated by Graybeal [36] in an extensive study to characterize mechanical properties of UHPC. More than 1000 cylinders were tested and several factors affecting UHPC compressive strength were examined including specimen geometry, fiber effect, loading rate, treatment effect, and demolding age. The first three factors did not significantly affect UHPC compressive strength with only a maximum difference of 8% attributed to different geometry (smaller cylinder sizes and cubes). UHPC was affected by treatment methods in which the compressive strength with a 95% confidence interval of stream-treated and untreated cylinders were of 28 and 18.3 ksi (193 and 126 MPa), respectively. Results also indicated that early demolding as soon as the integrity allowed (at 28 hours) can reduce UHPC compressive strength between 25 and 30% (compared to 47 and 55 hours) caused by the loss of moisture allowed for hydration. The testing of 30 cylinders resulted in the average elastic modulus of 7650 and 6200 ksi (52.8 and 42.8 GPa) for stream-treated and untreated UHPC, respectively. Slightly higher compressive strength of 28.6 ksi (197 MPa) and elastic modulus between 8270 and 8905 ksi (57 to 61.4 GPa) were observed by Association Francaise de Genie Civil [37]. UHPC is known for high strength gain at early age. After 3 days, steam-treated and untreated UHPC cylinders gained compressive strength of approximately 24 and 10 ksi (170 and 70 MPa), respectively [36]. All five untreated UHPC materials studied by Haber et al. [34] reached the compressive strength of 14 ksi (96 MPa) after 7 days of casting.

1.4.1.4 Tensile Properties

UHPC tensile behavior can be categorized into three separate responses including linear elastic, strain-hardening, and strain softening behavior. The linear elastic response is dominant prior to the first cracking occurs. After that UHPC undergoes formation of

microcracks due to fiber bridging effect and partial fiber debonding, resulting in strain-hardening response. Strain softening initiated as cracks (or deformation) localized. A lot of experimental and analytical investigations have been conducted to evaluate UHPC tensile properties from discrete first cracking tensile strength, ultimate tensile strength to the complete stress-strain relationship.

Four-point bending test of 2.75 x 2.75 x 11 in (70 x70 x 280 mm) notch beams were suggested by Chanvillard and Rigaud [38] and AFGC [37]. Load-crack mouth opening was recorded and UHPC tensile stress-strain relationship was obtained using back analysis to correlate the test data though curve fitting. The beam test had simple test setup, but exhibited several shortcomings that may prevent determination of true UHPC tensile stress-strain. First, beam test is size-dependent. The notch induces stress concentration that may prevent the multiple cracking behavior of UHPC. Back analysis is made possible with additional assumptions and requires complex computations.

Graybeal [36] used four different tension tests such as flexural prism test, split cylinder test, direct tension test, and mortar briquette test. Based on the results from the four tests, first crack tensile strength of 1.3 and 0.9 ksi (9 and 6.2 MPa) were suggested for heat-treated and untreated UHPC, respectively, but all the four tests were unable to determine the post-cracking tensile strength and relationship. Graybeal and Baby [39] developed a simple direct tension test setup using a square prism. The test was able to identify different phases of UHPC tensile response including elastic behavior, repeated inelastic cracking of the cementitious matrix, straining within discrete cracks, and localization at a single crack. Direct tension specimen with the dimension of 2 x 2 x 17 in (51 x 51 x 432mm) was suggested.

Zhou and Qiao [40] analytically and experimentally investigated UHPC tensile responses using dog-bone specimens subjected to direct tension test. A specimen with a total length of 18 in (457 mm), a thickness of 2 in (51 mm), and a width of 3 in (76 mm) at the two ends and 2 in (51 mm) at middle portion with the gauge length of 6 in (152 mm) was

recommended. The specimen had a concave curved length of 1.73 in (44 mm) with a large curvature radius of 6 in (152 mm) used to transit between the end and middle sections and avoid high stress concentration. A steel threaded rod with 0.5 in (13 mm) diameter was embedded 4 in (102 mm) at both ends to provide a simple gripping mean for tension test. A trilinear tensile stress-strain curve that includes linear elastic, strain hardening, and strain softening was suggested.

1.4.1.5 Bond Properties

The dense properties and steel fiber of UHPC not only increase its compressive and tensile strength, but also significantly improve bond performance. Previous studies indicated that UHPC could reduce up to 70% of tension reinforcement embedment length required by AASHTO and LRFD bridge design specifications when NSC and grout are used. Bond responses of reinforcing steel embedded in UHPC are affected by various parameters including side cover, splice length, bar size, bar strength, confinement level, and states of stress. Detailed literature on this topic is reviewed in Chapter 4.

1.4.2 High-Strength Steel

To utilize the full compressive strength of UHPC, complementary tension reinforcement having high yield strength is required. Micro-composite multi-structural formable Steel (MMFX) grade 100 is utilized for high-strength (HS) steel in this research study. MMFX grade 100 exhibits a nominal yield strength of 100 ksi (690 MPa) and an ultimate strength between 165 and 174 ksi (1138 and 1205 MPa) which by far exceeds the mechanical properties of ASTM A615 grades 60 and 80 and exceeds ASTM A1035 and AASHTO MP 18 requirements, but maintains similar ductility. With almost twice the yield capacity compared with conventional reinforcement, using MMFX can significantly reduce longitudinal reinforcement ratio of RC structural elements as shown in Fig. 1.5. MMFX steel has 3

times more corrosion resistance than NS steel and requires thinner concrete cover for corrosion protection. This can result in longer arm of leverage and larger flexural capacity of structural elements. Berke [41] and Williamson et al. [42] described MMFX when using in low-permeability concrete as a rebar having service life greater than 100 years and 200 years, respectively.

MMFX Conventional steel

Figure 1.5: Reinforcement ratio comparison between MMFX and conventional steel

MMFX bars were utilized as reinforcement for bridge decks in various field applications such as the Iowa and Kentucky Departments of Transportation. The reinforcement was also used with UHPC and NSC in multiple research investigations. Ansley [43] compared the performance of MMFX and NS Gr. 60 reinforcing steel using four RC girders reinforced longitudinally with #6 (M16) bars having continuous length, 10 in splice length, 30.5 in splice length, and #10 (M32) continuous bars to induce shear failure. All four girders reinforced with MMFX exhibited higher loading capacity, yet had limited ductility compared with specimens reinforced with Gr. 60 bars due to the lack of a well-defined yield point of

MMFX. Additional design and detailing consideration were suggested when using MMFX. Saleem et al. [44] investigated the use of UHPC with MMFX as light-weight deck system to replace open-grid steel deck of Florida movable bridges. MMFX was considered due to its high strength and high corrosion resistance. The deck showed promising results and satisfied the strict self-weight limit of movable bridges. Haber et al. [16] showed that the use of MMFX as footing dowels was effective in limiting the high strain penetration of seismic column longitudinal rebars into footing, and ensured linear elastic behavior and reduced damage of the footing.

1.5 Objectives and Scopes

The objective of this research is to experimentally and analytically investigate the seismic performance of a new and simple damage-tolerant precast column connection for use in medium and high seismic regions utilizing UHPC. The connection laps the longitudinal reinforcement from a precast column with dowel bars from a precast footing using a short splice length, a practical rebar cover, and no shear reinforcement within the connection region. The connection is designed to shift the PH formation above the connection region and maintain linear-elastic response within the footing. This research study can be categorized into three main sections including (1) large-scale column testing, (2) bond investigation using component-level specimens, and (3) analytical modeling.

In the first and primary section of this research, two 0.42-scale circular precast columns with different aspect ratios (AR) of 4.0 and 2.5 were tested under a reversed cyclic loading. The two precast columns were utilized to investigate the effects of different shear intensity, rebar size, and splice length. Results were compared with two reference CIP columns from a previous study. Detailed design, construction, test setup, and experimental results were presented with focus on: column strength and displacement ductility, lap splice devel-

opment and shear performance of the connection, strain penetration into the footing and top of UHPC connection, and PH formation location.

The second section of this research is the testing of component-level specimens to study the local bond behavior of reinforcing steel embedded in UHPC. Two types of experimental tests that contain 21 modified direct tension pullout specimens and 6 lap-splice beam specimens were conducted. This component-level study focuses on reinforcing bars embedded in UHPC that has small side cover where existing data is inadequate. Several parameters were considered including splice length, side cover, bar size, and bar strength. The experimental data was used to recommend the required development length and bond strength under unconfined conditions.

Analytical investigation of the two precast columns was performed in the third and final section. Initially, the uniaxial direct tension pullout test was simulated. Bond-slip model obtained from the modeling and least optimization was utilized in the column simulation. One-dimensional (1D) fiber-section and two-dimensional (2D) plane stress finite element method (FEM) were used to model the precast columns. The 1D modeling used rotational spring elements to account for bond-slip rotation effects. The 2D FEM provides a more realistic modeling of slip between reinforcement and UHPC using link elements. Results of the two modelings were compared with the experiments.

1.6 Dissertation Outline

This dissertation is divided into six chapters and begins with introduction chapter that describes the background and previous research on ABC and UHPC for substructure in seismic regions. The chapter also introduces the high-strength materials used in this research and lists the research objectives. Experimental program of the large-scale precast columns which includes the design concept, design procedures, construction processes, material prop-

erties, and test setup and loading protocols are presented in chapter 2. Chapter 3 discusses the testing results of the AR = 4.0 and AR = 2.5 precast columns separately in comparison with the benchmark CIP columns. The results show detailed column responses that include damage progress, force-displacement relationship, energy dissipation, PH curvature deformation and strain profiles, and stress transfer in the splice region.

Chapter 4 covers the experimental investigation on bond behavior of reinforcing steel embedded in UHPC under several varying parameters using direct tension pullout and lap-splice beam test setups. Analytical modeling of the precast columns using 1D fiber section and 2D plane stress FEM are presented in chapter 5 and compared with the precast column experimental results. Selection of material constitutive models, bond slip model, and element types are described in detail. Chapter 6 summarizes the research findings, provides conclusions and recommendation with discussion of the required future work.

CHAPTER 2: LARGE-SCALE COLUMN EXPERIMENTAL PROGRAM

2.1 Introduction

Past research on seismic GS connections observed the reduced precast column ductilities that were caused by large strain concentration at the column-footing interface and additional stiffness from connection materials in PH regions ([12], [13], and [14]). Debonding the column-footing interface [15] and the use of shifted plastic hinge (SPH) concept to relocate the typical failure mode at the column-footing interface of precast columns [16] were able to improve the column ductilities. Grouted duct, pocket and member socket connections for precast columns showed good seismic performance but required large embedment length. The use of UHPC-filled duct could reduce the required embedment length (l_d) to $24d_b$ [28]. Dagenais et al. [27] effectively retrofitted rectangular RC columns having deficient splice length (l_s) of $24d_b$ utilizing UHPC jacketing to replace NSC in PH region. The retrofitted columns exhibited high ductility and PH damage was minimized. Reduction of PH damage was also observed by Zohrevand and Mirmiran [30] with the use of UHPC twice the PH length, but the high compressive strength of UHPC prevented the material from attaining the full dilation and crushing strain capacity, resulting in reduced column displacement ductility. On the other hand, extensive static pullout test studies of UHPC-reinforcement (Graybeal [46]; Yuan and Graybeal [47]) showed that the use of minimal l_d was able to develop deformed steel reinforcement. Approximately two-third of l_d can be reduced using UHPC compared with the minimum l_d of $24d_b$ required by AASHTO and LRFD bridge design specifications when conventional grout or NSC is used.

The large-scale column tests and bond investigation of reinforcement in UHPC summarized above suggest the potential in developing a new damage-tolerant seismic connection

for precast columns that uses short bar splice length with UHPC. Meanwhile, the SPH concept has shown promising results in improving precast column ductility. The experimental program in this chapter utilizes UHPC lap splice and SPH concept to test two large-scale precast bridge columns. The columns had the same diameter but different aspect ratios (AR) used to study the connection performance under different shear demand. The chapter covers additional details on the experimental program discussed in Chan et al. [45].

2.2 Design Concept

Fig. 2.1 depicts the design concept of the precast columns using the proposed UHPC connection and SPH. The primary design objective is to avoid the high strain penetration into the footing by shifting the PH above the connection region and maintaining the linear elastic response of the footing. In the proposed connection, UHPC was used to resist three force components. Tension force was initially transferred from NS bars through UHPC bond strength, which in turn ensured the force transfer to the HS footing dowels. Compression and shear forces were resisted by the high compressive and tensile strength of UHPC. Past studies using UHPC with lap splice [27] and embedded bar [28] showed that failure typically occurred due to rebar fracture at the column-footing interface where the moment demand was high. To ensure the shift of PH formation, the plastic moment capacity at the column-footing interface was increased relative to the section slightly above UHPC region that took the role as the critical section. SPH was realized by using HS steel bars as the footing dowels and normal strength (NS) bars as the precast column longitudinal reinforcement. The HS steel increases yield strength and minimizes energy dissipation of the column-footing interface. The precast column shaft is expected to behave similarly to a typical CIP bridge column, where ductility is ensured due to the displacement contribution coming from slip between UHPC and the lapped bars, rather than strain penetration into the footing.

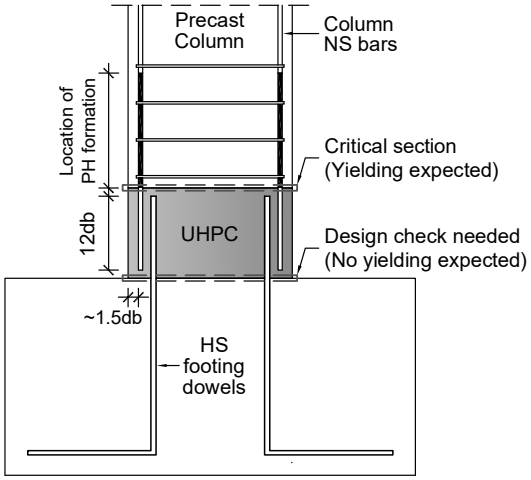

Figure 2.1: Proposed UHPC lap splice connection

2.3 Specimen Details

Two 0.42-scale precast bridge columns were constructed and tested using reversed cyclic loading at the structures laboratory of the University of Central Florida; this assumes that a full-scale bridge column has a diameter of 48 in (1219 mm). The two columns had different reinforcing ratios, bar sizes, connection heights, and AR. AR is herein defined as the ratio of the column height to diameter. Table 2.1 shows the test matrix of the precast columns and the reference CIP columns investigated by Al-Jelawy et al. [48], which are used for comparison purposes. To ease referral of the CIP columns, C-40 and C-25 are hereinafter re-abbreviated as CIP40 and CIP25, respectively. PCU40 was a flexurally dominant column with an AR of 4.0. The column diameter was 20 in (508 mm). The column height was 80 in (2032 mm) measured from the footing surface to the center of the loading head. CIP40 was the benchmark flexural column for PCU40. PCU25 had an AR of 2.5 and the same diameter as PCU40, but was a flexural-shear column. PCU25 had a column height of 50 in (1270 mm). CIP25 was the benchmark flexural-shear column for PCU25. Fig. 2.2 and 2.3 show schematics of AR = 4.0 and AR = 2.5 columns, respectively.

Table 2.1: Column test matrix

Column models	Column Type	Diameter (in)	Aspect ratio (AR)	Reinforcing ratios		Longitudinal bar sizes		Connection sizes	
				Longitu-dinal	Trans-verse	Footing dowels	Column shaft bars	Diameter (in)	Height (in)
PCU40	Precast	20	4	1.43%	0.74%	#7 HS	#6 NS	20	12.5
CIP40	CIP	20	4	1.95%	0.74%	-	#7 NS	-	-
PCU25	Precast	20	2.5	1.00%	0.81%	#6 HS	#5 NS	20	11.0
CIP25	CIP	20	2.5	1.41%	0.50%	-	#6 NS	-	-

NS denotes normal strength bars conforming to ASTM A615 Grade 60 ksi.
HS denotes high strength bars conforming to ASTM A1035 Grade 100 ksi.
Notes: US #7 = 22M, US #6 = 19M, US #5 = 16M, 1 in. = 25.4 mm, 1 ksi = 6.9 MPa.

2.4 Design Procedures

2.4.1 Cast-in-Place Columns

The two CIP columns were designed using Caltrans Seismic Design Criteria (SDC) [49] to obtain the target displacement ductility capacity of 7.0 subjected to the design axial load of 126 kips (560 kN) [48]. Displacement ductility capacity μ of a cantilever column is defined as the ratio between the ultimate column displacement Δ_u and the idealized yield displacement of the column Δ_y, where Δ_u is the summation of Δ_y and plastic displacement Δ_p determined based on column curvature capacity using Eq. 2.1 to 2.3. The idealized yield curvature ϕ_y and plastic curvature ϕ_p can be obtained from moment-curvature (M - ϕ) analysis. L_p is the PH length calculated from Eq. 2.4, L is the total column length, and f_y is the reinforcement yield strength.

CIP40 was longitudinally reinforced with ten US#7 (22M) ASTM A615 Grade 60 rebar corresponding to 1.95% reinforcing ratio and transversely reinforced with spiral W4.5 with 1.50 in pitch corresponding to 0.74% reinforcing ratio. CIP25 was longitudinally with ten US#6 (19M) ASTM A615 Grade 60 rebar (1.41% reinforcing ratio) and transversely reinforced with spiral W4.5 having minimum allowable reinforcing ratio of 0.50%, which

corresponds to 2.25 in pitch. Test results showed that the idealized plastic lateral load and average displacement ductility capacity were $V_p = 44.8$ kips (199.3 kN) and $\mu_{avg} = 7.75$ for CIP40, and $V_p = 60.6$ kips (269.6 kN) and $\mu_{avg} = 6.90$ for CIP25.

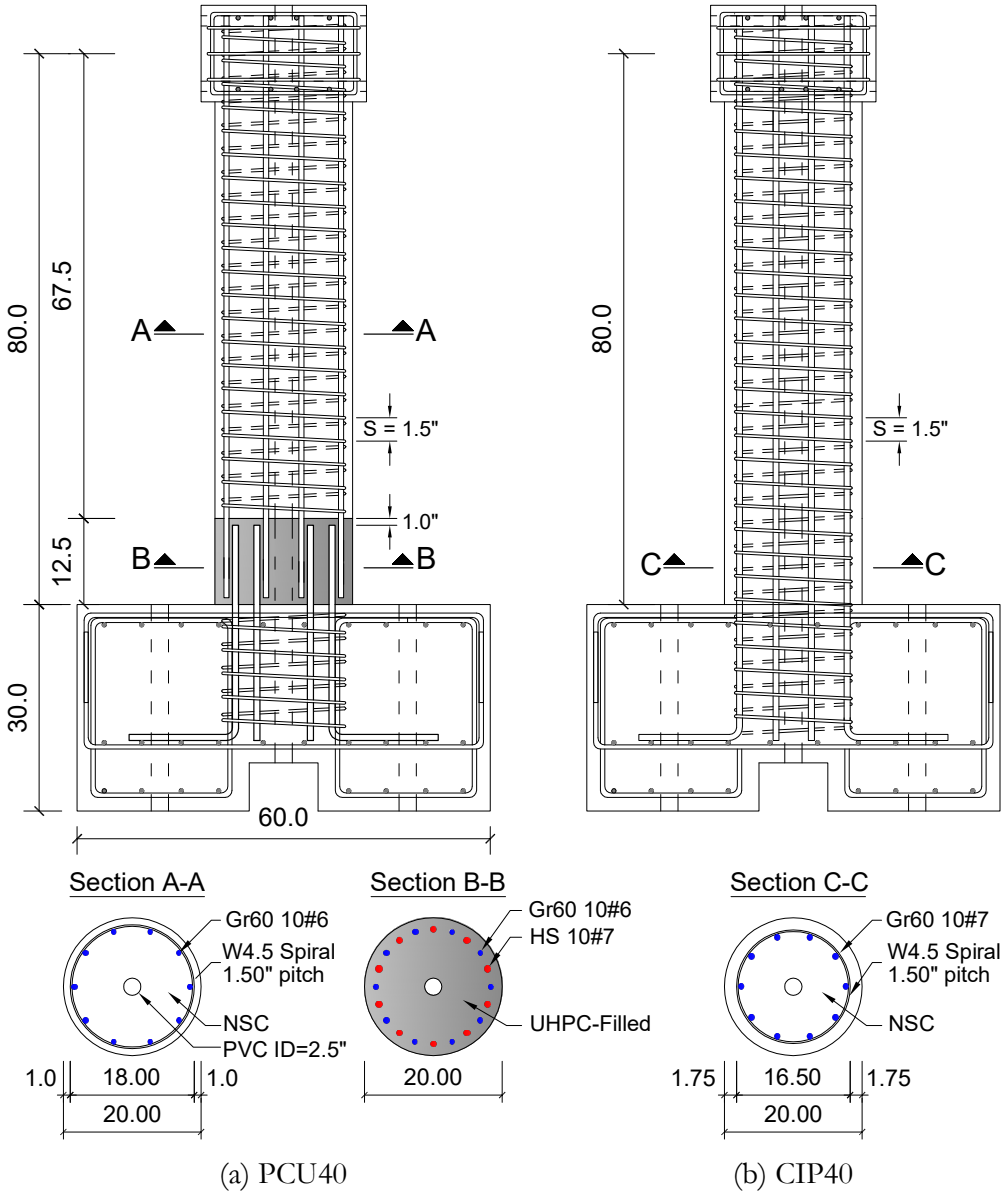

(a) PCU40 (b) CIP40

Figure 2.2: Schematic of AR = 4.0 columns

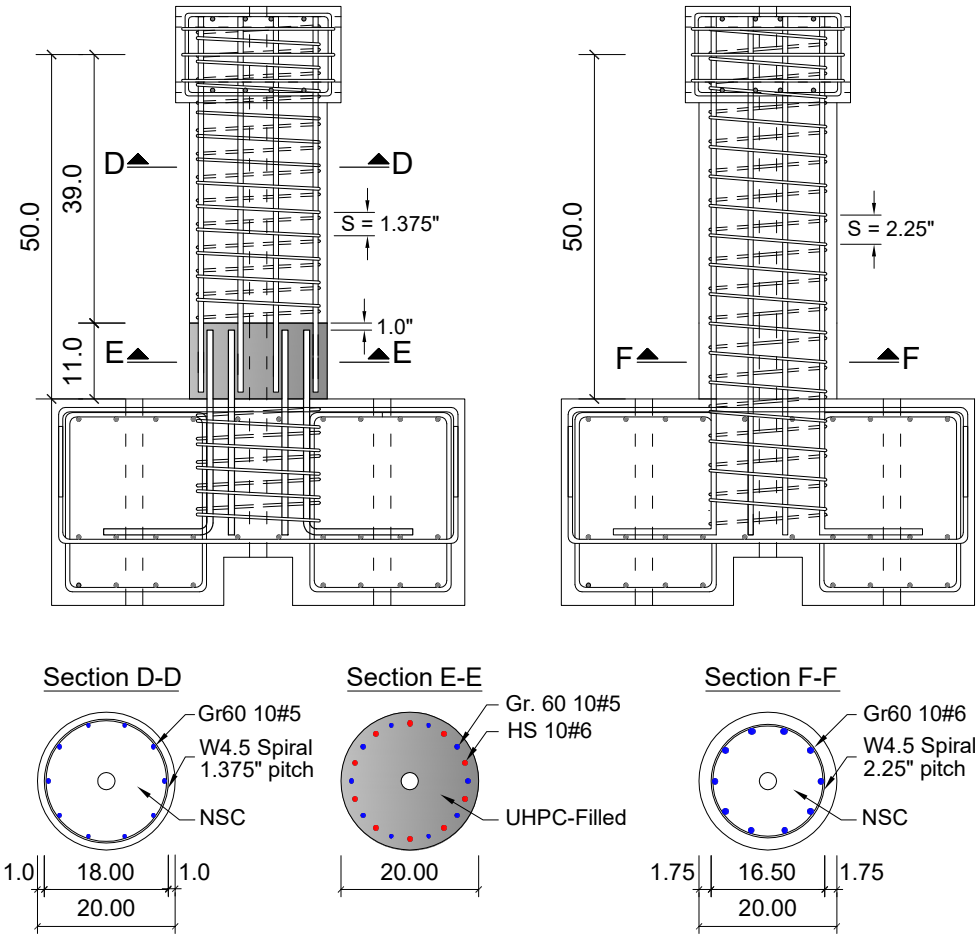

(c) PCU25 (d) CIP25

Figure 2.3: Schematic of AR = 2.5 columns

$$\Delta_u = \Delta_y + \Delta_p \tag{2.1}$$

$$\Delta_y = \frac{L^2}{3}\phi_y \tag{2.2}$$

$$\Delta_p = L_p\phi_p(L - \frac{L_p}{2}) \tag{2.3}$$

$$L_p = 0.08L + 0.15f_y d_b \geq 0.3f_y d_b \tag{2.4}$$

2.4.2 Precast Columns

Current Caltrans SDC prohibits splicing of main flexural reinforcement in the PH region. Consequently, the two precast columns PCU40 and PCU25 were designed to achieve the same target plastic lateral load capacity V_p as CIP40 and CIP25, respectively. Two assumptions were made in the design: (1) the footing and UHPC connection are rigid and (2) PH formation occurs above the connection region. This reduces distance between the applied load and critical section, which is herein referred to as column effective length (L') determined from the difference of L and the rigid connection height. A 1.0 in (25 mm) clear concrete cover was used for both precast columns to obtain proportional standard cover to full-scale bridge columns. Non-contact lap splices with rebar spacing of approximately $2.0d_b$ and $2.5d_b$ and spliced length l_s of $14d_b$ of column rebars (or $12d_b$ of footing dowels) were used based on the modified pullout test results conducted by Yuan and Graybeal [47] to allow yielding of NS bars and prevent early bond failure. A gap of 1.0 in (25 mm), 2 times the fiber length, between NS bars and footing surface and between HS bars and column shaft interface was chosen to prevent bar buckling. This resulted in the UHPC connection height and effective column length of 12.5 in (318 mm) and 67.5 in (1714 mm) for PCU40, and 11.0 in (280 mm) and 39.0 in (991 mm) for PCU25. Transverse reinforcement in the connection was eliminated due to the large shear resistance provided by the high compressive and tensile strength of UHPC.

The reduced column length decreased moment demand at the critical section. To achieve approximately the same plastic lateral load to CIP columns, reduction of longitudinal reinforcing ratios were required. Both precast columns were longitudinally reinforced with one smaller bar size than the CIP columns. Ten US#6 (19M) and ten US#5 (16M) ASTM A615 Grade 60 rebar were utilized as PCU40 and PCU25 longitudinal reinforcement, respectively. PCU40 was transversely reinforced with the same transverse steel ratio as

CIP40. A higher transverse steel ratio was used for PCU25 to prevent the large shear cracks in the PH region observed in CIP25.

Table 2.2: Concrete design material parameters

Column shaft/ connection	Unconfined concrete				Confied concrete		
	f'_c (ksi)	f'_{cu} (ksi)	ε_{co}	ε_{cu}	f'_{cc} (ksi)	ε_{cc}	ε_{cu}
PCU40	5	0	0.002	0.005	6.658	0.0053	0.0144
PCU25	5	0	0.002	0.005	6.788	0.0055	0.0151
Connection	20	0	0.003	0.006	-	-	-

Table 2.3: Reinforcing steel design material parameters

Rebar Types	Properties					
NS bars	f_y (ksi)	f_u (ksi)	E_s (ksi)	E_{sh} (ksi)	ε_{sh}	ε_{su}
	68	95	29000	1305	0.009	0.09
HS bars	f_y (ksi)	E_s (ksi)	b	$R0$	$CR1$	$CR2$
	165	29000	0.001	2	0.925	0.15
W4.5 spiral	f_{yh} (ksi)			ε_{su}		
	68			0.09		

Nonlinear moment-curvature ($M - \phi$) analysis using the Open System for Earthquake Engineering Simulation (OpenSees) was conducted to determine the idealized plastic moment (M_p) for both precast columns. Plastic lateral capacity V_p is the ratio of M_p and L'. The $M - \phi$ analysis used a zero-length element with fiber section. Uniaxial material "Concrete01" based on Kent-Scott-Park model [50] and "Concrete04" based on Mander model [51] were used to model the unconfined concrete cover and confined concrete core, respectively. Ultimate strain of the confined concrete was calculated based on Priestley and Park [52]. Longitudinal reinforcement was modeled with "ReinforcingSteel" using Chang and Mander model [53]. Values of the constitutive model parameters for reinforcing steel and concrete used in OpenSees are listed in Table 2.2 and 2.3, respectively. Fig. 2.4 shows the actual and elasto-plastic (EP) $M - \phi$ results for the precast columns. The EP curve is idealized from

the actual $M - \phi$ curve, calculated such that the areas under EP and actual curves after the onset of yielding are equivalent. The resulting plastic lateral load V_p were 47.5 kips (211 kN) for PCU40 and 66.2 kips (294 kN) for PCU25.

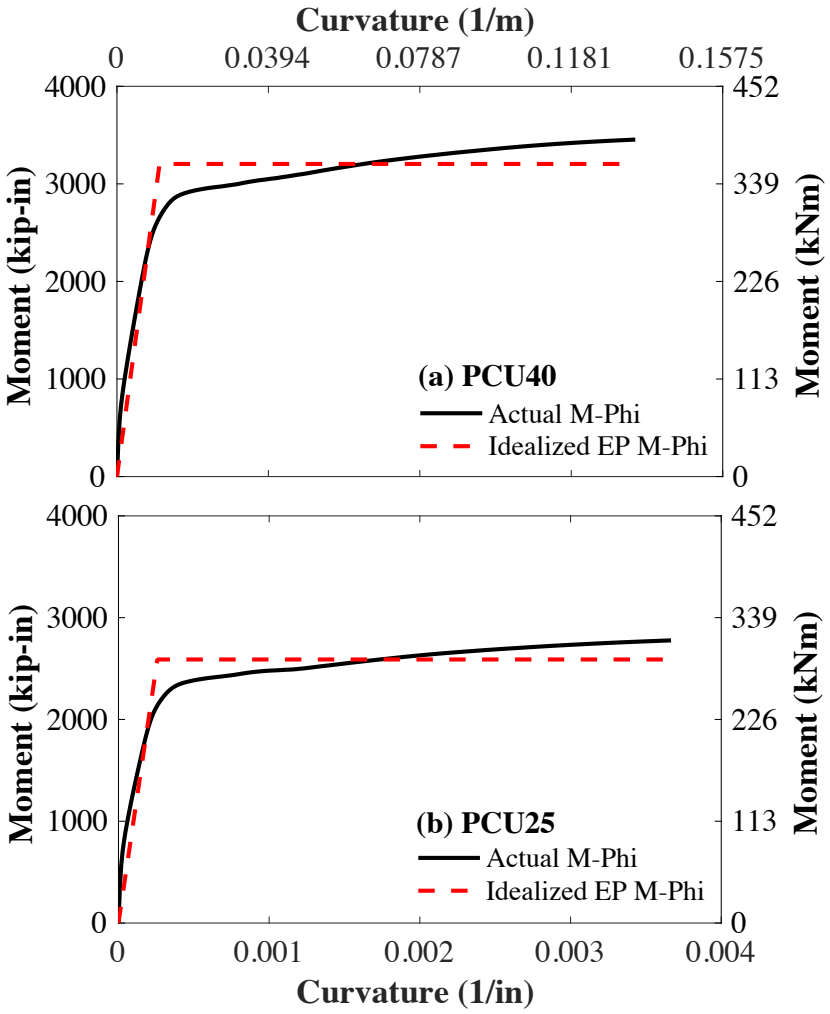

Figure 2.4: Moment-curvature response of precast columns

To realize the SPH design, the section of the column-footing interface was reinforced with HS footing dowels, which have the same longitudinal reinforcing ratio as CIP column reinforcement. A design check was conducted at this section using $M - \phi$ analysis to determine and verify that UHPC and HS bar maximum stresses (f'_{cmax} and f_{smax}) were lower than

UHPC ultimate strength and HS yield strength, respectively. Uniaxial materials Concrete01 and Steel02, the latter based on Giuffre-Menegotto-Pinto model, were used to model UHPC and HS bars, respectively. Fig. 2.5 shows the $M - \phi$ curves for the UHPC connection of both PCU40 and PCU25. The maximum stresses at the interface were $f'_{cmax} = 12.1$ ksi and $f_{smax} = 82.3$ ksi for PCU40, and $f'_{cmax} = 12.1$ ksi and $f_{smax} = 89.1$ ksi for PCU25. The results indicated that the UHPC connection exhibited linear elastic performance.

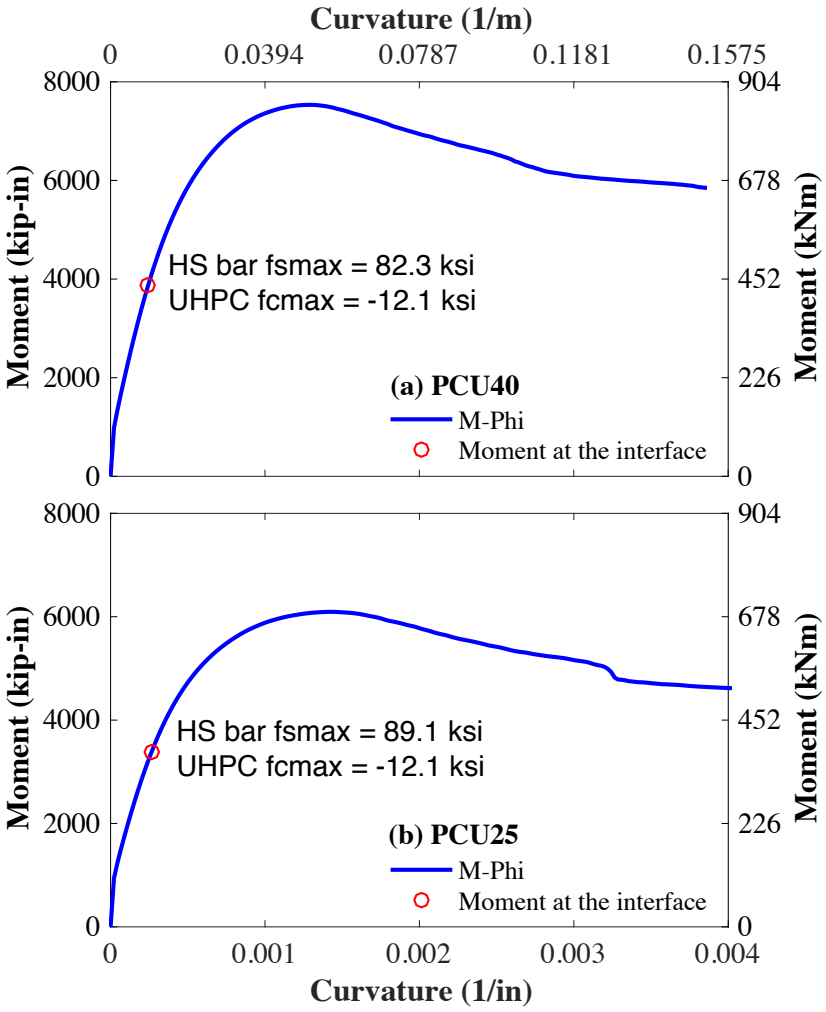

Figure 2.5: Moment-curvature response of UHPC connection

2.5 Construction Processes

The construction of the precast columns follows four-step processes. All the construction work was conducted at the University of Central Florida. First, the precast footings were constructed as shown in Fig. 2.6. The footings were 60 x 60 x 30 in (1524 x 1524 x 762 mm) in length, width and height respectively, and were reinforced with NS bars #5 (16M) at the bottom and top reinforcement mats. The footing incorporated a 7 x 11 in (178 x 280 mm) opening strip parallel to the loading direction, a 2.5 in (63.5 mm) hole at the center, and four 3.0 in (76 mm) holes at the edges to allow post-tensioning. HS dowels placed inside the footing were secured by steel spiral and a wooden template. The dowels protruded from the footing surface 11.5 in (292 mm) for PCU40 and 10.0 in (254 mm) for PUC25. After the reinforcing cage was arranged, concrete was cast and allowed to cure a minimum of 24 hours prior to formwork removal.

The precast column shaft was constructed in parallel having NS longitudinal bars protruding the same length as the corresponding footing dowels. A wooden template was used to ensure the protruding length and position of each deformed bar. The column shaft also incorporated a 2.5 in (63.5 mm) hole at the center for post-tensioning purpose. A 1.0 in (25 mm) ID PVC vent was installed at the column base to allow air pocket removal when pouring the connection. Fig. 2.7 shows the precast column reinforcement cage, formwork, PVC vent location, and loading head reinforcement detail.

Prior to connecting the column shaft to the footing, concrete surfaces of the two precast elements were ground to expose aggregate finish and pre-wetted to obtain a saturated surface dry (SSD) condition. A template was used to hold the heavy column weight, form bracing, and provide an inlet to cast the connection. An alternative construction method more suitable for on-site installation that uses a stay-in-place alignment steel or concrete pedestal and steel bracing is also suggested (Fig. 2.8).

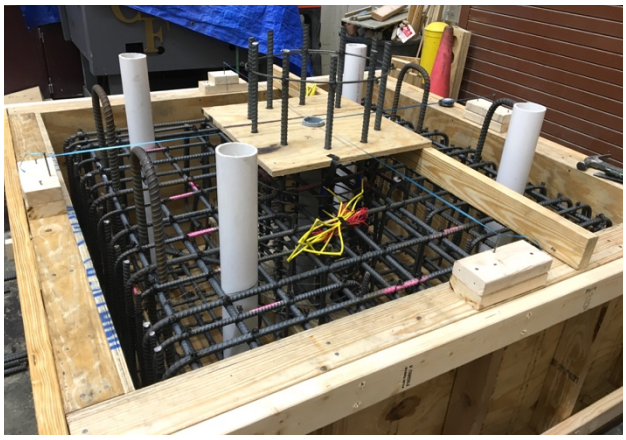

(a) Footing reinforcement

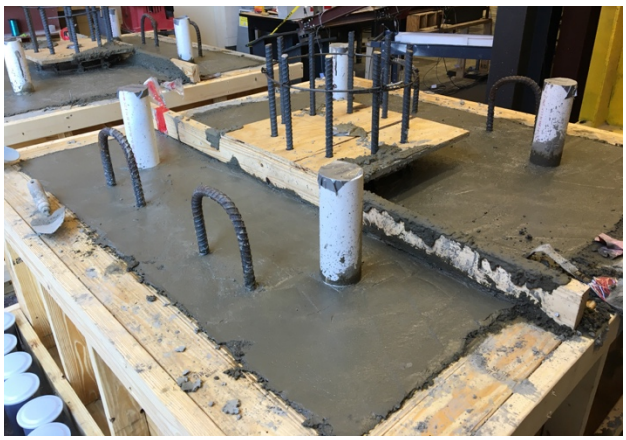

(b) Footing after concrete casting

(c) Completed footings

Figure 2.6: Footing construction

(a) Column reinforcement

(b) Column formwork

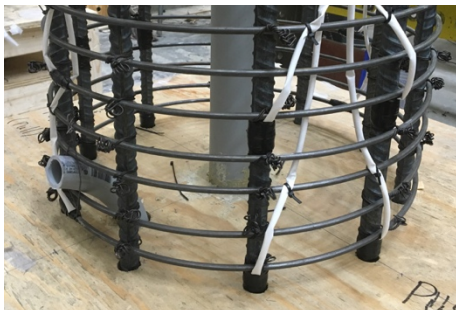

(c) PVC vent

(d) Loading head

Figure 2.7: Column shaft construction

(a) Column shaft with extended bars

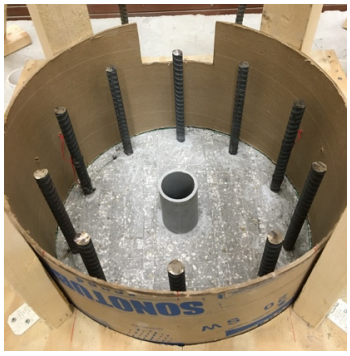

(b) Footing with aggregate expose

(c) Connection details

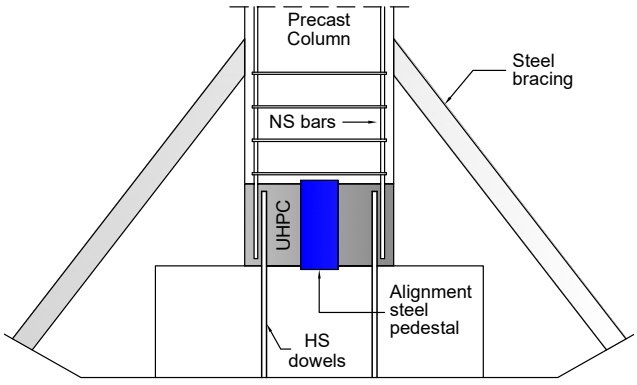

(d) Alternative method for on-site column installation

Figure 2.8: Preparation for connection casting

(a) UHPC mixing

(b) Modified flow table test

(c) Connection formwork

(d) Pouring of UHPC connection

Figure 2.9: UHPC connection casting

(a) PCU40

(b) PCU25

Figure 2.10: Completed precast columns

Finally, UHPC was mixed following the batching and mixing procedures as described in Chapter 1. Temperature and slump of each mixing batch were measured using a hand-held thermometer and a modified flow table test, respectively, to prevent overheating and ensure workability of UHPC. The average measured UHPC temperature and slump were 66 °F (19 °C) and 8.25 in (210 mm), respectively. UHPC was poured approximately 15 in (381 mm) above the bottom surface of the column shaft. This provided pressure head to force the

remaining air through the PVC vent until the UHPC itself flowed out of the vent (Fig. 2.9). Fig. 2.10 shows the completed precast columns PCU40 and PCU25 after formwork removal.

2.6 Material Properties

Five different materials were utilized to construct each precast column including (1) conventional concrete, (2) UHPC, (3) mild reinforcing steel (NS), (4) HS, and (5) plain steel wire. The precast columns require a large quantity of conventional concrete and UHPC, resulting in different casting batches. The following sections provide details on batching, mixing, and the mechanical properties of the materials used.

2.6.1 Conventional Concrete

The footings and column shafts were cast with two different batches of conventional concrete, but used the same mix with a maximum aggregate size of 0.375 in (9.5 mm) and a slump of 6 in (152 mm). The average 28-day and test-day compressive strength of the footings and column shafts were determined according to ASTM C39 [54]. Table 2.4 shows the measured properties of conventional concrete utilized for the precast columns and concrete properties of CIP columns reported by Al-Jelawy et al. [48].

2.6.2 UHPC

The UHPC utilized for the connections was a commercial product UP-F2 developed by King Packaged Materials Company [35] with the material constituents as listed in Table 1.1. PCU40 and PCU25 connections were cast with separate batches of UHPC. The average 28-day and test-day compressive strength (f'_c), elastic modulus, and flexural strength (f) of the UHPC were determined using ASTM C1856/C1856M [55] with the average of three specimens per batch. The results with first crack and ultimate tensile strength (f_t) are

listed in Table 2.4. The cylinder samples had nominal diameter of 3 in (76 mm) and nominal height of 6 in (152 mm). The top and bottom surfaces were saw cut and ground to ensure the perpendicularity to the axis prior testing. The cylinders were tested using universal testing machine (UTM) with a stress rate of 145 psi/s (1.0 MPa/s). Three linear variable differential transducers (LVDTs) attached to a pair of parallel rings mounted on the cylinder with the gauge length of 3 in (76 mm) were used to measure the average axial strain. Fig. 2.11 shows the UHPC cylinder specimens, failure mode, and typical compressive stress-strain responses. Consistent specimen-to-specimen stiffness, strength and strain at peak stress results were observed.

The prism samples for flexure test had nominal width and depth of 3 in (76 mm) and span of 9 in (229 mm). The prisms were subjected to four-point bending test with a displacement control rate of 0.02 in/min (0.5 mm/min) using UTM. The specimen was instrumented with an LVDT at mid-span, installed on an aluminum bar attached to the concrete beam at the support locations to determine pure beam deflection at mid-span and eliminate support settlement. Fig. 2.12 shows the flexure test setup, failure mode and load-displacement results. Flexural strength was calculated using modulus of rupture formula $f = PL/bd^2$, where P is the peak load, and b, d, and L are width, depth, and span of the prism, respectively.

UHPC tensile stress-strain relationship was determined using dog-bone specimens recommended by Zhou and Qiao [40]. The test specimens had a total length of 18 in (457 mm), a thickness of 2 in (51 mm), and a width of 3 in (76 mm) at the two ends and 2 in (51 mm) at middle portion with the gauge length of 6 in (152 mm). A single specimen per batch was tested using UTM under a displacement rate of 0.02 in/min (0.5 mm/min). Four LVDTs (one at each side) were used to measure the average axial strain and account for possible bending effects. Fig. 2.13a and 2.13b depict the UHPC direct tension test setup and failure mode, respectively. UHPC tensile stress-strain relationship up to the strain of 0.02 was

shown in Fig. 2.13c. It was observed that the UHPC used in this study initially exhibited linear elastic behavior followed by strain-hardening after the first cracking occurred. The strain-hardening produced multiple microcracks before a single localized crack was formed, resulting in a gradual strain-softening.

Table 2.4: Measured concrete material properties

Materials	Elements	Properties	Column models			
			PCU40	CIP40	PCU25	CIP25
Conventional concrete	Footing	28-day f'_c	6.04	4.98	6.04	4.98
		Test-day f'_c	7.58	9.49	7.68	9.43
	Column shaft	28-day f'_c	6.48	5.12	6.48	5.12
		Test-day f'_c	8.02	7.4	8.29	7.6
UHPC	Connection	28-day f'_c	20.31	-	19.9	-
		Test-day f'_c	20.63	-	21.25	-
		Elastic modulus	5840	-	5640	-
		Flexural strength f	4.09	-	3.61	-
		First crack f_t	1.12	-	1.10	-
		Ultimate f_t	1.43	-	1.39	-

f'_c is compressive strength; f is flexural strength; f_t is tensile strength
Notes: All units in ksi; 1 ksi = 6.9 MPa

2.6.3 Reinforcing Steel

The precast column shafts and CIP columns were reinforced longitudinally with ASTM A615 Grade 60 (Grade 420) [56] steel and transversely with ASTM A1064 [57] W4.5 (6 mm) plain wire spiral. Longitudinal steel reinforcement used for the footing dowels of precast columns was ASTM A1035 Grade 100 (Grade 690) [58]. Yield strength f_y, yield strain ε_y, ultimate strength f_u, and strain at peak stress ε_u of all reinforcement were determined using ASTM A370 [59]. The measured reinforcement properties are listed in Table 2.5.

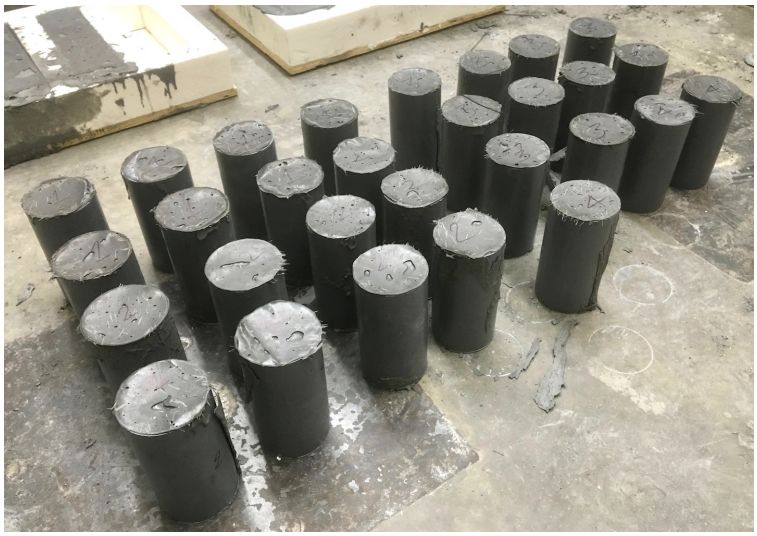

(a) UHPC cylinders

(b) Failure mode

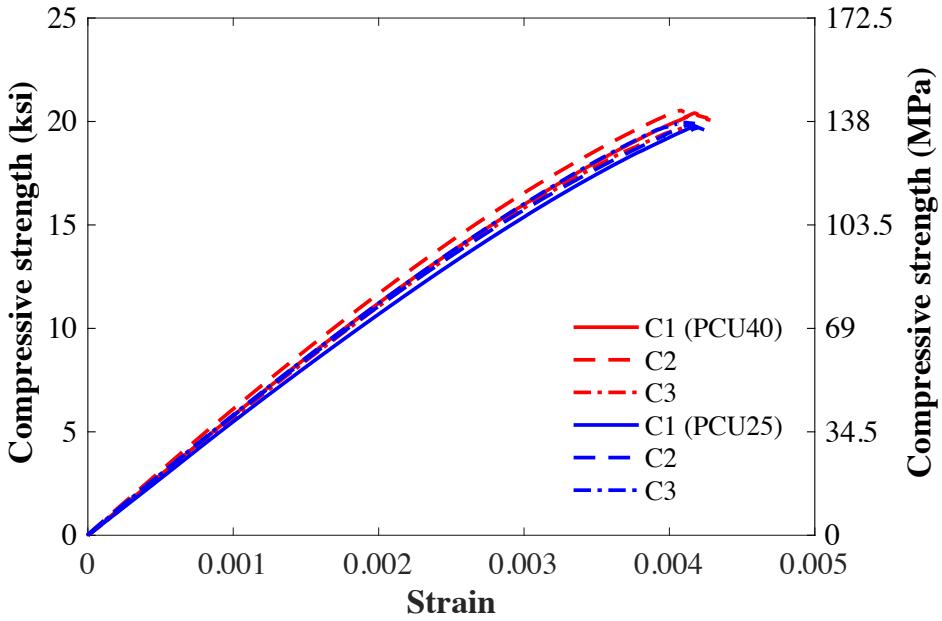

(c) Stress-strain relationship

Figure 2.11: UHPC compression test

(a) Test setup

(b) Failure mode

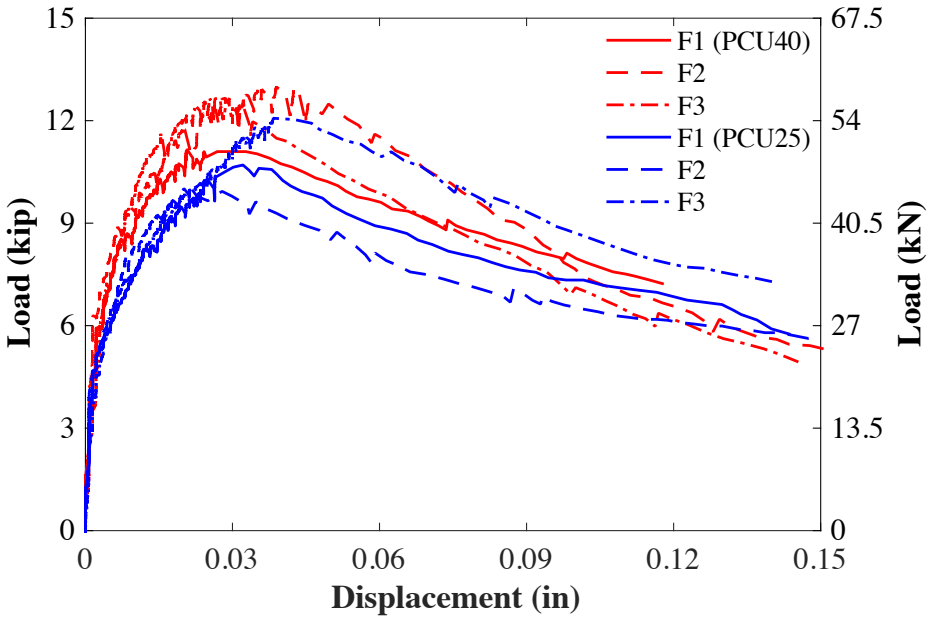

(c) Load-displacement relationship

Figure 2.12: UHPC flexure test

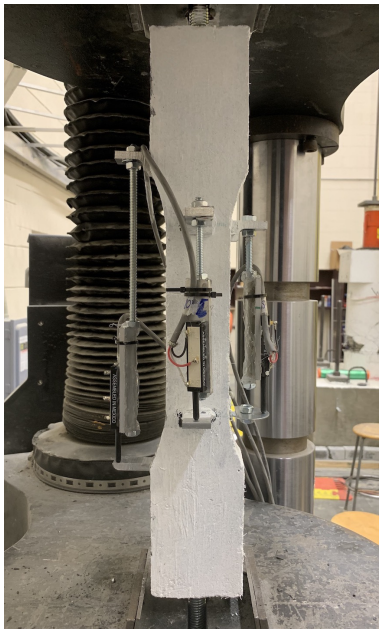

(a) Dog-bone specimen

(b) Failure mode

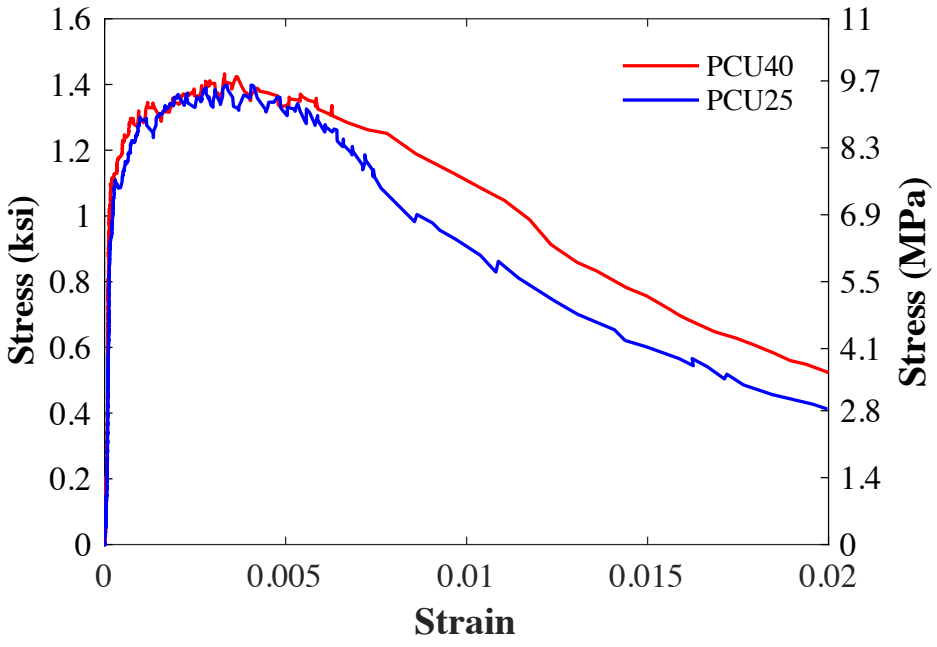

(c) Stress-strain relationship

Figure 2.13: UHPC Direct tension test using dog-bone specimens

Table 2.5: Measured reinforcing steel material properties

Bar Size	Grade (ksi)	f_y (ksi)	ε_y (in/in)	f_u (ksi)	ε_u (in/in)
#5 NS	60	62.9	0.00217	96.2	0.1368
#6 NS	60	65.2	0.00224	110.2	0.1233
#7 NS	60	68.6	0.00251	104	0.1170
#6 HS	100	122.1	0.0067	159.5	0.0646
#7 HS	100	118.1	0.0066	162.1	0.0407
W4.5	-	98.3	0.0045	105.7	0.0860

Notes: 1 ksi = 6.9 MPa; 1 in. = 25.4 mm
"NS" denotes normal-strength bar
"HS" denotes high-strength bar

2.7 Test Setup and Loading Protocol

Fig. 2.14 and 2.15 show the precast column test using a single curvature cantilever test setup. Footing fixity was secured with high-strength grout and four HS post-tensioning rods. Each column was subjected to a constant axial load of 126 kips (560 kN) utilizing a two-way acting hollow-core hydraulic jack and an HS post-tensioning rod passing through the center of the column. A pressure relief valve and an in-line pressure transducer were mounted to control and monitor fluctuation of the axial load. A maximum axial load undershoot and overshoot of -12% and 6%, respectively, were observed during the test when actuator traveled to the peak drift and returned to zero drift. Lateral load was applied using a 110 kip (490 kN) servo-hydraulic actuator connected to the column loading head and concrete reaction blocks. The column was subjected to a series of slow cyclic loading using a drift-based displacement-control loading protocol. Two full push and pull cycles were applied at the drift ratios of 0.25, 0.50, 0.75, 1, 2, 3, 4, 5, 6, and 8% until failure occurred. Drift ratio is the ratio of column lateral displacement to the total column height. Failure is identified by the drop of 20% of lateral load.

A total of 23 LVDTs were installed at the push (North) and pull (South) loading side, and at the East side of each column to capture the curvatures, bond-slip rotations, and shear deformations of the columns. Three string potentiometers were mounted on column loading head to measure the average tip displacement of each column. Strain gauges were instrumented at different heights starting from 4 in (102 mm) below footing surface to approximately mid-height of the column to measure strains of longitudinal and transverse reinforcement.

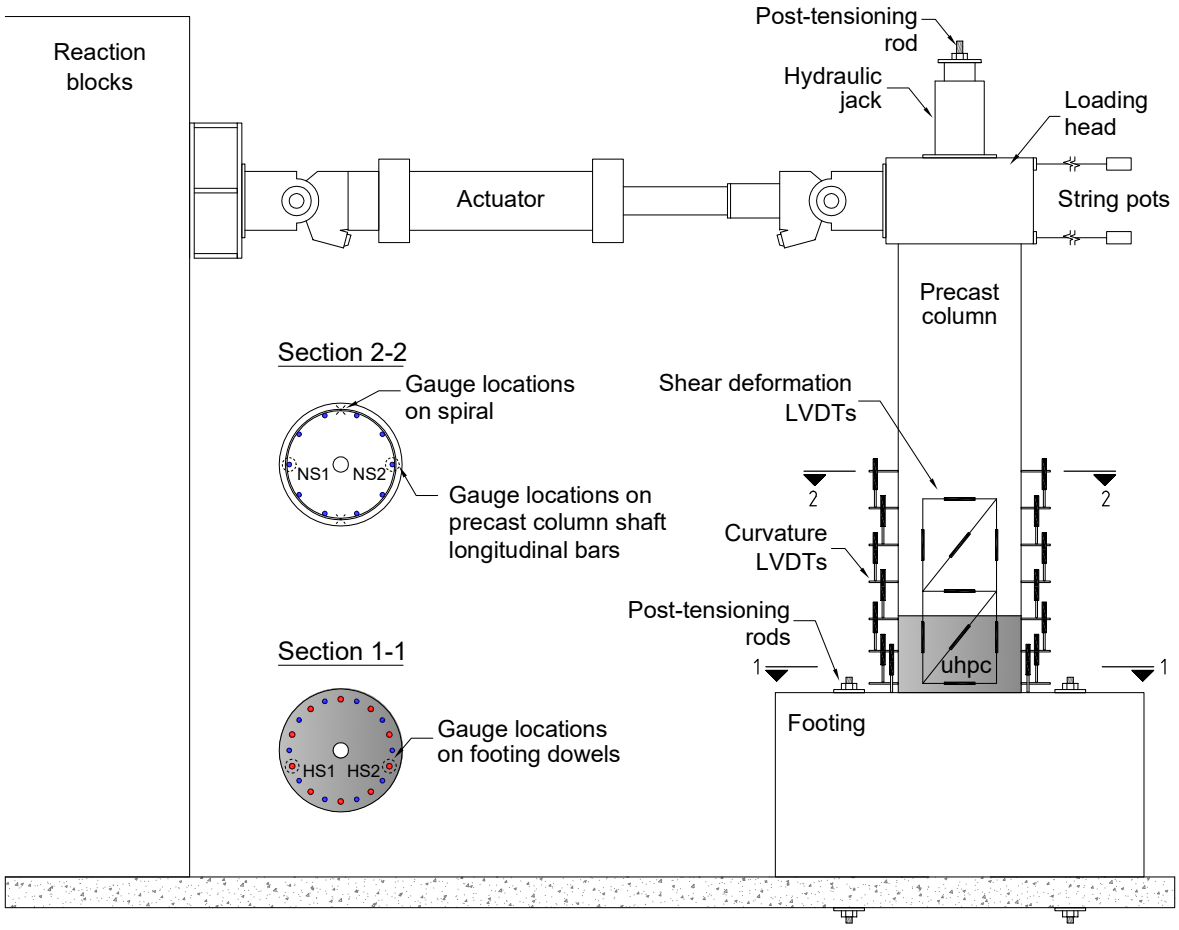

Figure 2.14: Schematic of column test setup and instrumentation

Figure 2.15: Column test setup photo

CHAPTER 3: COLUMN EXPERIMENTAL RESULTS

3.1 Introduction

This chapter presents the testing results of the two precast columns utilizing the proposed UHPC lap splice connection. The chapter presents additional details to the experimental results described by Chan et al. [45]. The results provide good insight of the experimental findings that include the damage progression at every drift ratio, force-displacement hysteresis responses, energy dissipation, curvature profiles and moment-rotations in the PH region, PH deformations and strain profiles, and stress transfer in the splice region. Columns PCU40 and PCU25 results are presented separately, but are also compared with the corresponding CIP columns tested by Al-Jelway et al. [48]. Several important column responses were used to identify achievement of the design objectives, which include (1) column strength and displacement ductility, (2) lap splice development and shear performance of the connection, (3) strain penetration into the footing and top of UHPC connection, and (4) PH formation location.

3.2 Precast Column PCU40

3.2.1 Damage Progression

Fig. 3.1 to 3.6 show the damage progression of column PCU40 at every drift level inspected after each half drift cycle. A continuous blue line was marked on the precast column to identify the UHPC connection region and the precast column shaft. Prior to 2% drift, the precast column shaft exhibited distributed hairline flexural cracks along two-thirds of the column shaft height (Fig. 3.1a to 3.1c). By the end of 2% drift, the hairline flexural cracks extended and fine inclined shear cracks initiated. No apparent cracks were seen on the UHPC connection of PCU40 (Fig. 3.2a). At 3% drift, additional flexural and shear cracks

occurred, while the existing flexural cracks began to localize on the column shaft. Apparent crack opening caused by the slip of NS bars were observed at the column-connection interface. A few short and fine flexural cracks were observed on the UHPC connection a few inches below the interface (Fig. 3.2b).

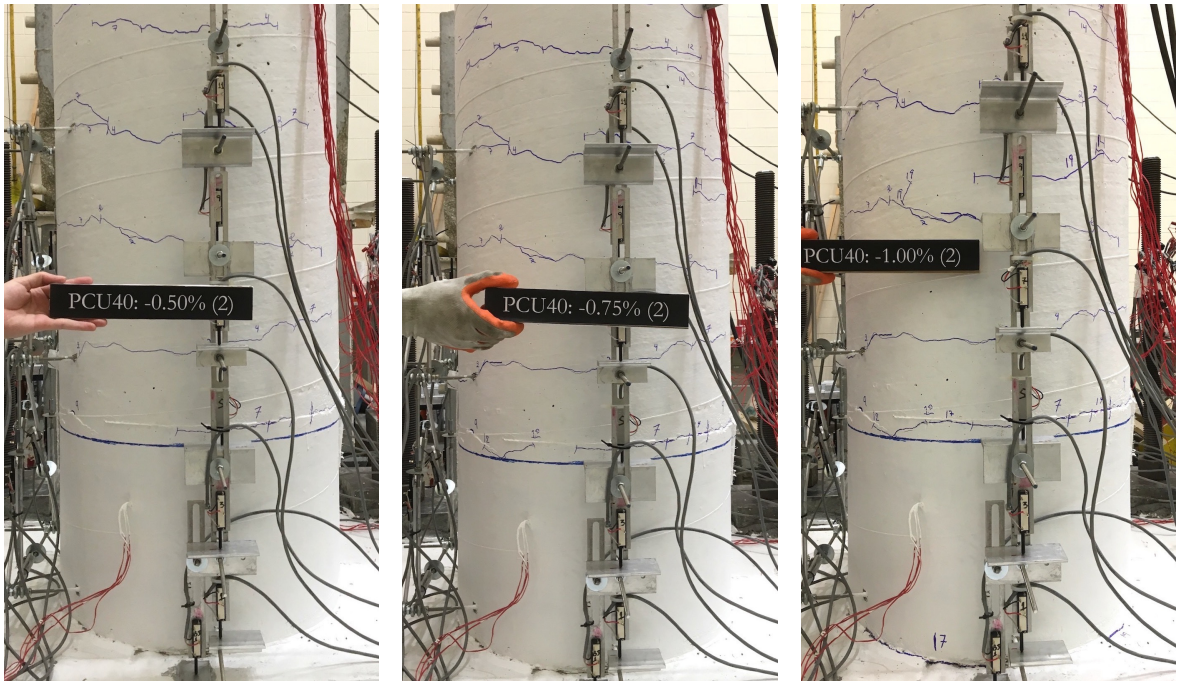

(a) 0.50% drift (b) 0.75% drift (c) 1% drift

Figure 3.1: Observed damage of PCU40 prior to 2% drift (North)

At 4% drift, PCU40 experienced initiation of cover spalling at the base of the column shaft on the north (N) and south (S) with additional fine inclined shear cracks on the west (W) and east (E) sides. The high tensile stress concentration of the extreme NS bars created additional short and fine flexural cracks on the top few inches of UHPC connection. Splitting cracks along the extreme NS and HS bars also initiated in the UHPC connection (S). The splitting cracks along HS bars were caused by the radial stresses generated from the

compressive strut between the NS bars in tension (Fig. 3.3). At 5% and 6% drifts (Fig. 3.4 and 3.5), concrete cover spalling extended and splitting cracks progressed towards the base of the connection. It can be observed that splitting cracks occurred predominately at the south side of the connection, while at north side few splitting cracks were seen. This can be attributed to different fiber orientation and distribution in the UHPC connection. At failure, PCU40 damage was limited to 12 in (305 mm) above UHPC connection where concrete core crushing initiated, followed by buckling of the main longitudinal bars, spiral fracture, and longitudinal bar fracture. Shear cracks were widened but limited to 0.1 in (2.5 mm) in width. Only minor splitting and flexural cracks were observed on the UHPC connection region, while the footing remained damage free (Fig. 3.6).

On the other hand, CIP40 exhibited very similar damage pattern and progression to PCU40 with the exception of the damage location and footing condition. Fig. 3.7 and 3.8 show the side by side comparison between the damage progression of the two columns at 4% and 8% drifts, respectively. At 4% drift, CIP40 also exhibited cover spalling yet at the column base directly above the footing surface. The footing surfaces exhibited radial cracks (Fig. 3.7b). At 8% drift, CIP40 failure started with core concrete crushing, followed by longitudinal bar buckling, and spiral fracture at the column base region (Fig. 3.8b). In addition, the footing concrete of CIP40 exhibited concrete delamination. The CIP column failure mode at the column base, with radial cracks and delamination of footing concrete, is typical of bridge columns due to high inelastic strain penetration from the longitudinal bars into the footing. Damage to precast column PCU40 above the UHPC connection and the undamaged footing showed that PH formation was successfully shifted. Longitudinal bar fracture and minor connection splitting cracks in PCU40 (N and S) indicated the efficient use of UHPC in developing short lap-spliced reinforcement and damage-tolerant seismic connection.

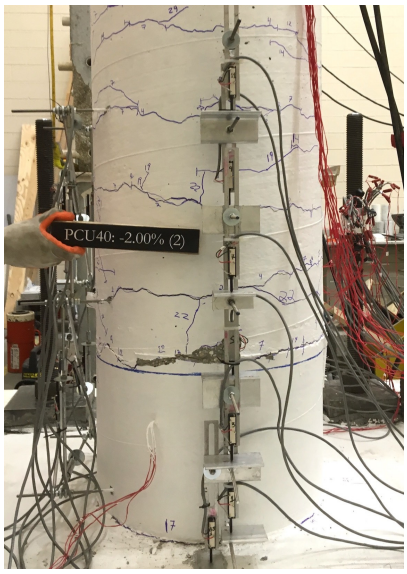

(a) 2% drift

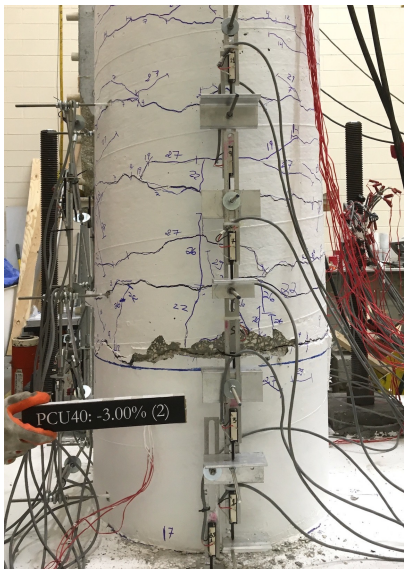

(b) 3% drift

Figure 3.2: Observed damage of PCU40 at 2% and 3% drifts (North)

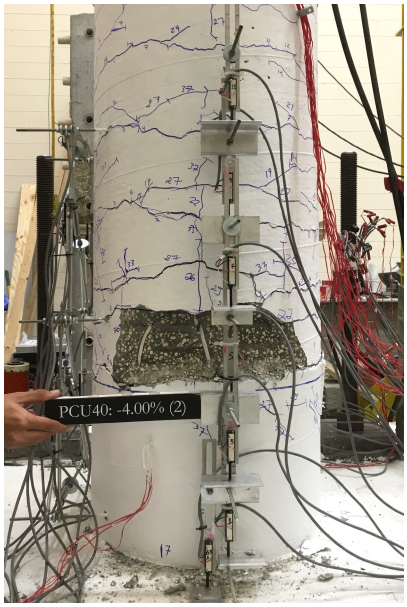

(a) North

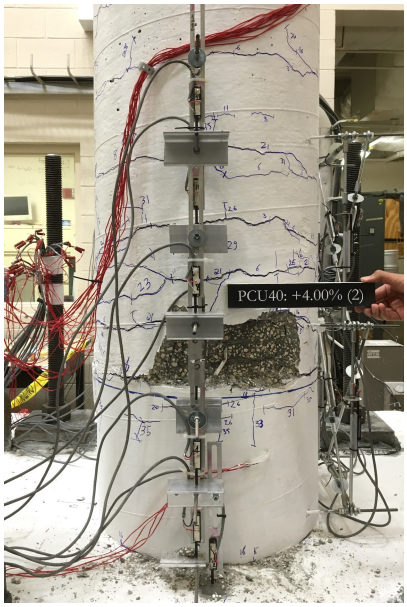

(b) South

Figure 3.3: Observed damage of PCU40 at 4% drifts (2nd cycle)

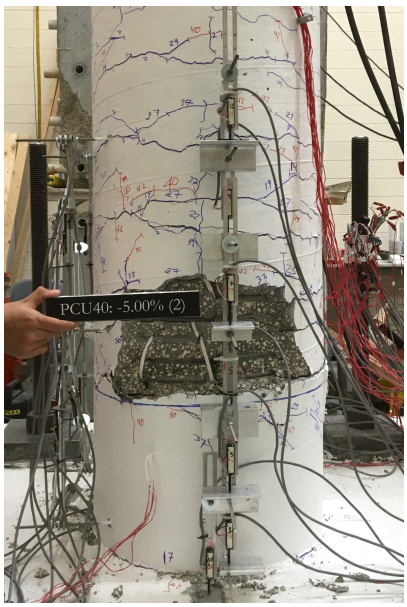

(a) North

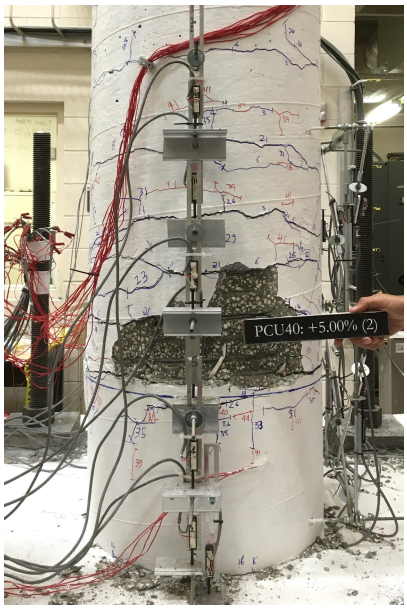

(b) South

Figure 3.4: Observed damage of PCU40 at 5% drifts (2nd cycle)

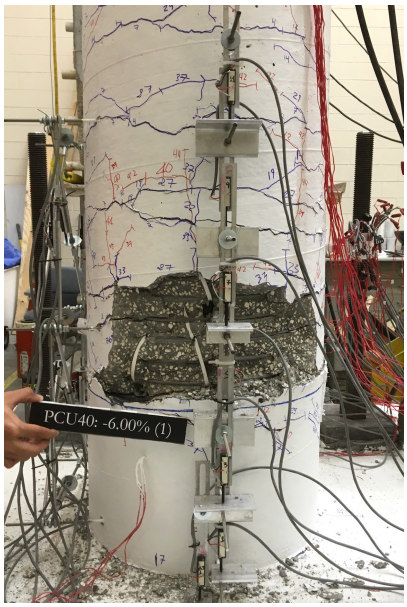

(a) North

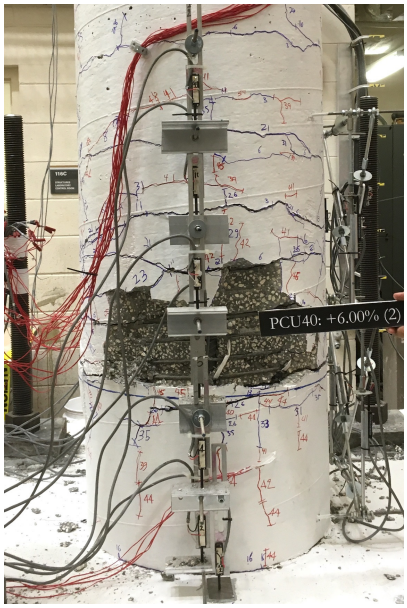

(b) South

Figure 3.5: Observed damage of PCU40 at 6% drifts (2nd cycle)

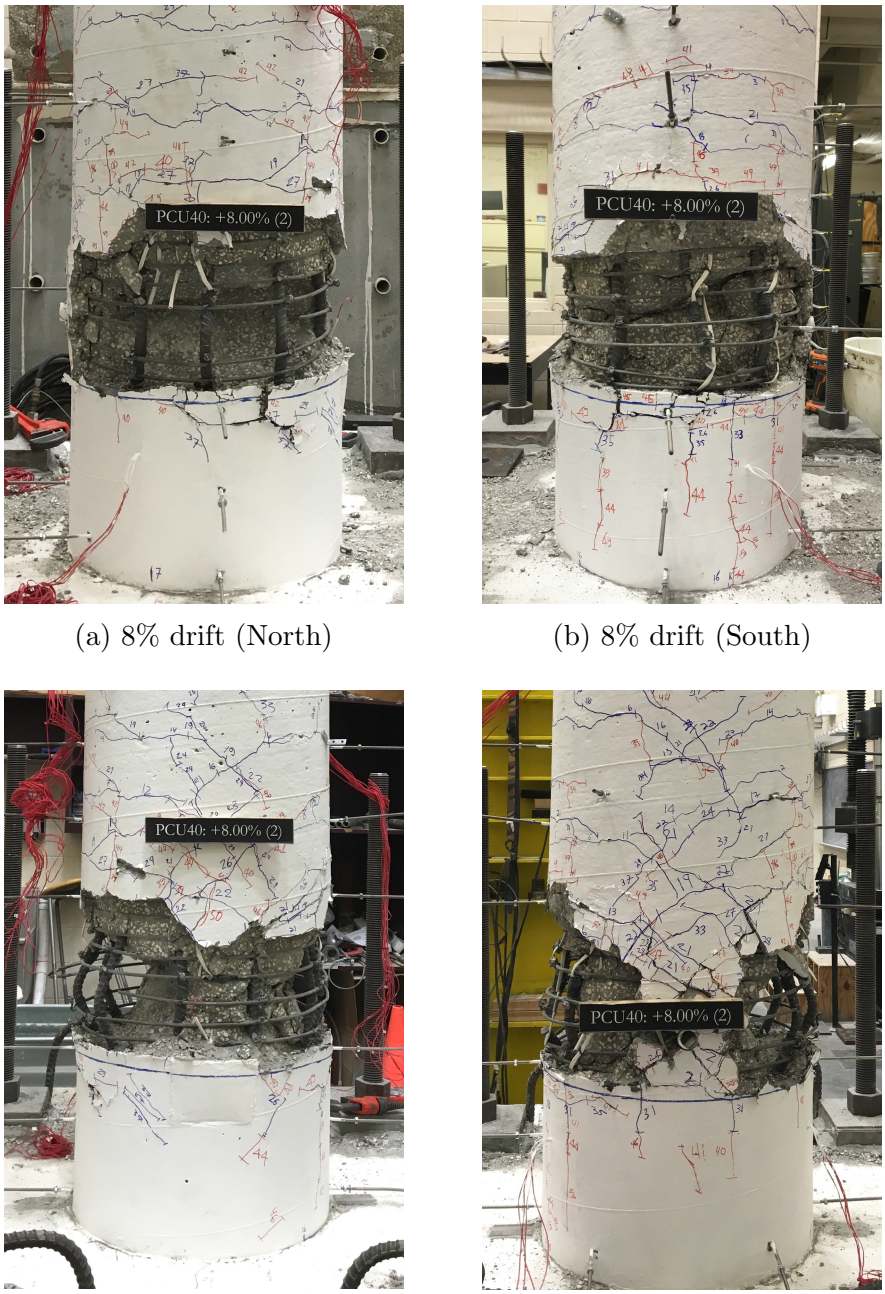

(a) 8% drift (North)

(b) 8% drift (South)

(c) 8% drift (West)

(d) 8% drift (East)

Figure 3.6: Observed damage of PCU40 at failure

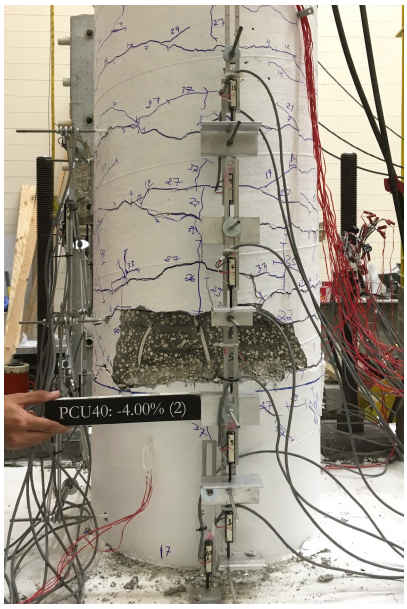

(a) PCU40 (North)

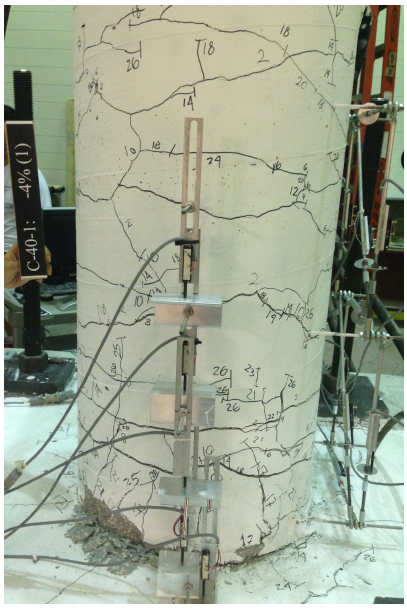

(b) CIP40 (North)

Figure 3.7: Comparison of damage pattern for AR = 4 columns at 4% drift

(a) PCU40 (East)

(b) CIP40 (East)

Figure 3.8: Comparison of damage pattern for AR = 4 columns at 8% drift (Failure)

3.2.2 Force-Displacement Relationship

The lateral force-drift hysteresis curves of PCU40 and CIP40 are shown in Fig. 3.9. The occurrences of important local responses in the two columns including the onset of rebar yield, onset of cover spalling, concrete cover loss, spiral fracture, NS bar rupture, and debonding of NS-UHPC are annotated. The plastic lateral load V_p and average displacement ductilities μ_{avg} shown in Fig. 3.10 were determined with Caltrans procedures [49] using the elasto-plastic (EP) curve. The EP curve is idealized from the average push/pull force-drift envelop prior to 20% drop of lateral load, calculated such that the areas under EP curve and the envelop after the first yield point (onset of yielding) are equivalent. The onset of longitudinal bar yielding was obtained from experimental strain data.

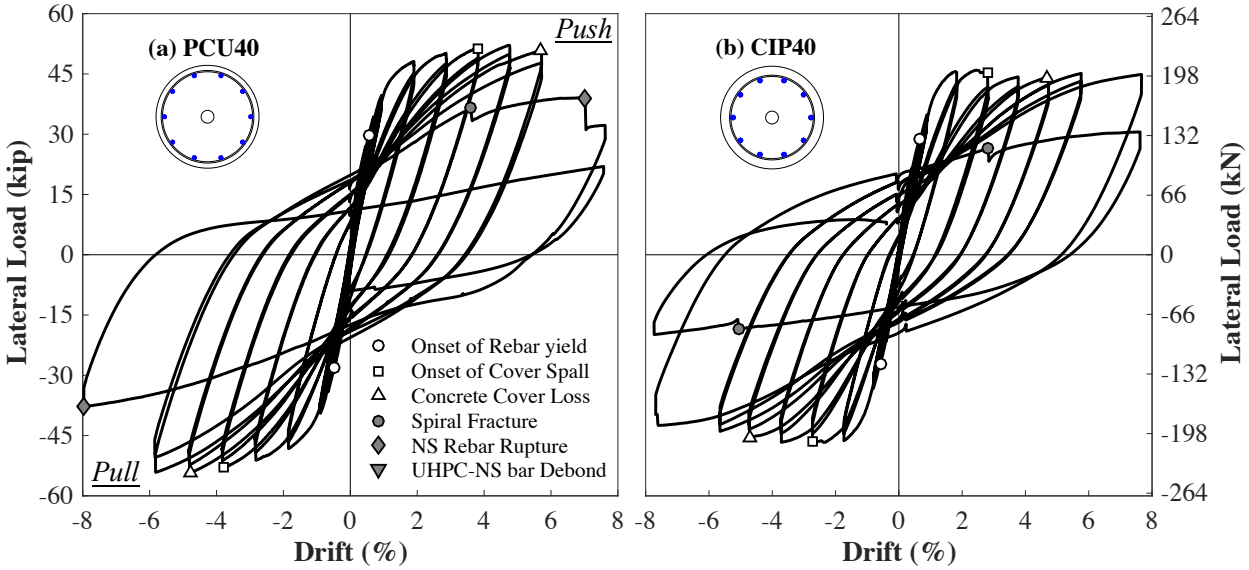

Figure 3.9: Force-drift relationships of AR = 4 columns

The hysteresis loops of both AR 4 columns prior to 8% drift were stable and wide. Both columns experienced strength degradation at failure (8% drift). PCU40 failed a cycle sooner than CIP40 resulting in the reduced ultimate displacement Δ_u, yet the precast column achieved both higher lateral load (V_p = 49.3 kips (219.3 kN)) and ductility (μ_{avg} = 7.90),

respectively compared with $V_p = 44.8$ kips (199.3 kN) and $\mu_{avg} = 7.75$ of CIP40. The larger lateral load and ductility of both precast columns compared with CIP columns were due to the increase of achieved concrete compressive strength (f'_c) compared with the assumed design f'_c, and the smaller yield displacements of the precast column, respectively.

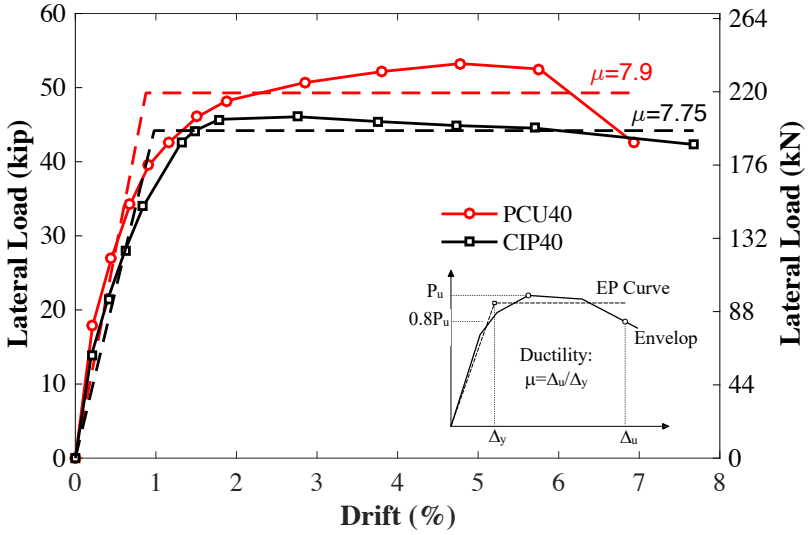

Figure 3.10: Average force-drift envelop of AR = 4 columns

3.2.3 Energy Dissipation

Energy dissipation E_D for a given cycle is the area under the single force-displacement hysteresis loop. E_D of the precast and CIP columns were compared using equivalent viscous damping ratio ξ_{eq}, calculated using eq. 3.1, where K_E is the effective stiffness determined from eq. 3.2, Δ_{max} and Δ_{min} are the maximum positive and negative displacements of the hysteresis loop, respectively, and P_{max} and P_{min} are the forces corresponding to the maximum positive and negative displacements, respectively. The damping ratio utilizes effective stiffness K_E to normalize E_D. This minimizes the effect of different lateral capacities and geometric configurations.

$$\xi_{eq} = \frac{E_D}{2\pi K_E \Delta_{max} \Delta_{min}} \tag{3.1}$$

$$K_E = \frac{P_{max} - P_{min}}{\Delta_{max} - \Delta_{min}} \tag{3.2}$$

Fig. 3.11 shows the ξ_{eq} of AR = 4 columns determined from the average between first and second loading cycles. The precast column PCU40 had good energy dissipation and comparable damping ratios to the reference CIP column at nearly every drift level. Prior to 1% drift, ξ_{eq} was low, but followed by increasing ξ_{eq} after initiation of yielding in the extreme longitudinal bars. On average after 1% drift, PCU40 had approximately 0.01 higher ξ_{eq} than CIP40. The larger ξ_{eq} of PCU40 can be attributed to the longitudinal bar slip that spread the bar yielding over a larger column height.

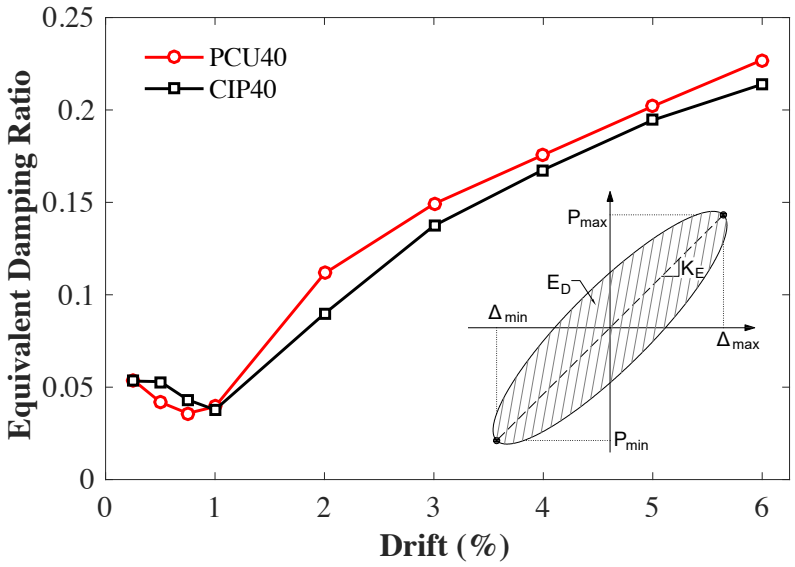

Figure 3.11: Equivalent damping ratios of AR = 4 columns

3.2.4 Plastic Hinge Curvatures and Rotations

Fig. 3.12 shows the curvature profiles of PCU40 and CIP40, which were measured using LVDTs installed on opposite faces of the columns at various heights. The schematic

of the instrumentation is shown in Fig. 3.14. A curvature (ϕ) at the center of a gauge length (h_{avg}) was calculated using eq. 3.3 and 3.4, where θ is the column rotation, ΔL_L and ΔL_R are the measured relative displacements at the left and right sides of the column under loading, respectively, D is the column diameter, d_L and d_R are the distances of the left and right LVDTs from the column faces, respectively. The curvatures were used to qualitatively quantify the PH distribution and stiffness of the UHPC connection.

$$\theta = \frac{\Delta L_L - \Delta L_R}{D + d_L + d_R} \tag{3.3}$$

$$\phi = \frac{\theta}{h_{avg}} \tag{3.4}$$

For column CIP40, the maximum curvatures at every drift level (from 2% to 6%) were observed at the column base where moment demand was high and major damage occurred. For PCU40, the largest curvatures were concentrated at the column-UHPC connection interface. Above the connection, plastic curvatures were continuously distributed which indicated a well-distributed PH of PCU40. On the other hand, UHPC connection displayed significantly smaller curvatures. This confirmed the stiffness of connection regions as assumed during design. The sharp increase of curvatures at the column base was attributed to rebar slip rather than the plastic curvatures.

The damage-tolerant behavior of UHPC connection of the precast column can be confirmed utilizing the hysteretic base moment-rotations at two critical sections: the column base (bond slip) and column-connection interface (section F2) as shown in Fig. 3.13. With increasing drift level, moment-rotation hysteresis loops of PCU40 grew wider at section F2 corresponding to the observed major damage above the connection. However, very thin hysteresis loops were observed at the base of the precast column, indicating that despite exhibiting splitting cracks, the UHPC connection was able to maintain strength and stiffness.

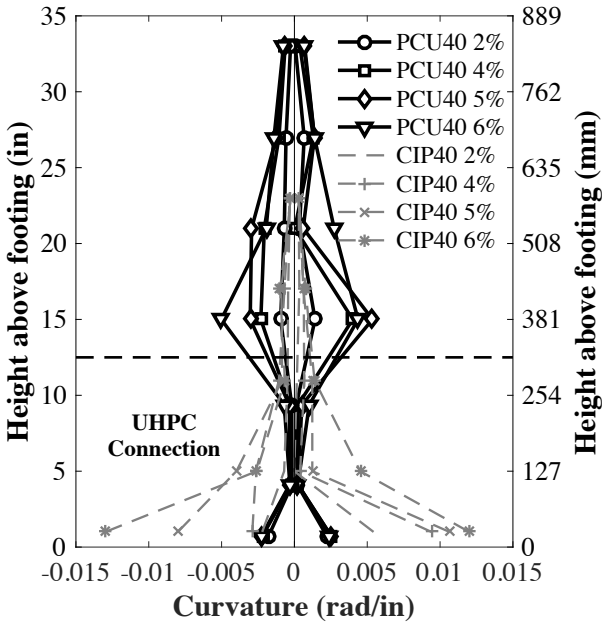

Figure 3.12: Plastic hinge curvature of AR = 4 columns

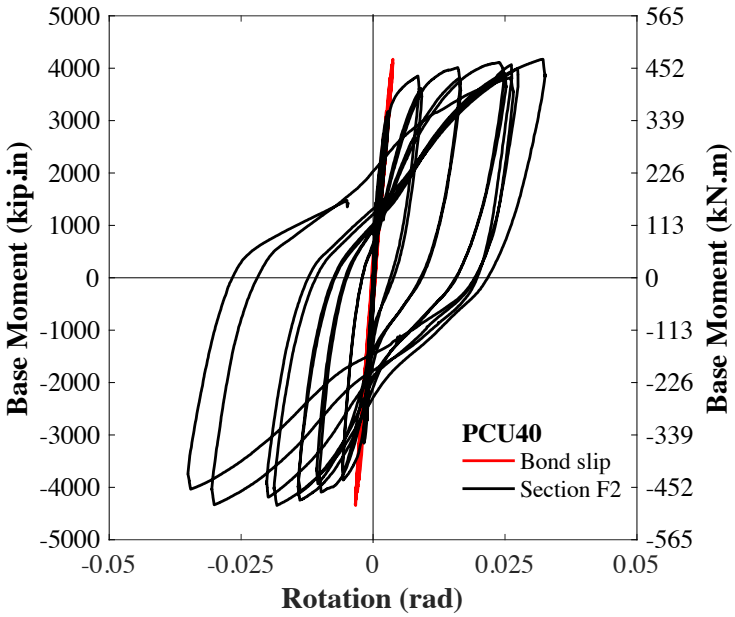

Figure 3.13: Base moment rotation of PCU40

3.2.5 Plastic Hinge Deformations

Fig. 3.14 shows the contributions to the tip displacement by the bond-slip due to strain penetration of well-anchored dowels, flexure, and shear deformations for PCU40 during the first cycle pushover load from 0.75% to 5% drifts. Bond-slip and flexure deformations (ΔF) were computed from the curvature LVDTs using eq. 3.5, where L is the column length, h_i is the distance from the footing surface to each segment rotation (θ_i). Shear deformations (ΔS) were computed from the shear LVDTs using eq. 3.6 and 3.7, where ΔD is the extension of diagonal LVDT, ΔD_{vh} is the combined extension due to vertical (Δ_v) and horizontal (Δ_h) extension, and b, h, and d are the horizonal, vertical, and diagonal gauge length of the shear LVDTs, respectively. To facilitate consistent physical interpretation between PCU40 and PCU25 responses in flexure, the flexural deformations were split into four regions: F1 (connection), F2+F3 (observed major damage), F4 and F5 (minor damage).

$$\Delta F = \theta_i(L - h_i) \tag{3.5}$$

$$\Delta S = \Delta D - \Delta D_{vh} \tag{3.6}$$

$$\Delta D_{vh} = \sqrt{(b + \Delta_h)^2 + (h + \Delta_v)^2} - d \tag{3.7}$$

Tip displacement of column PCU40 caused by bond-slip due to strain penetration of well-anchored dowels was only notable prior to 1% drift, and gradually decreased to less than 10% at larger drifts as a result of the elastic response of HS footing dowels shown in the subsequent section. The majority of tip displacement was caused by the flexural deformation in the major damage region (F2+F3). The F2+F3 deformation accounted for approximately 30% at the onset of NS bar yielding and increased to 60% at larger drifts due to the highly inelastic flexural responses. It can be noted that F2+F3 deformation includes both flexural deformation and bond-slip between UHPC and NS reinforcing bars. The contribution of

flexural deformations at the locations F1, F4, and F5 was small, representing less than 10% of column tip displacement. The shear deformation for PCU40 was insignificant throughout, contributing less than 4% to tip displacement at every drift. The PH deformation results showed that the proposed UHPC lap splice connection for PCU40 had low strain penetration from HS footing dowels. Relative slip between NS bars and UHPC played a key role in controlling the precast column deformations.

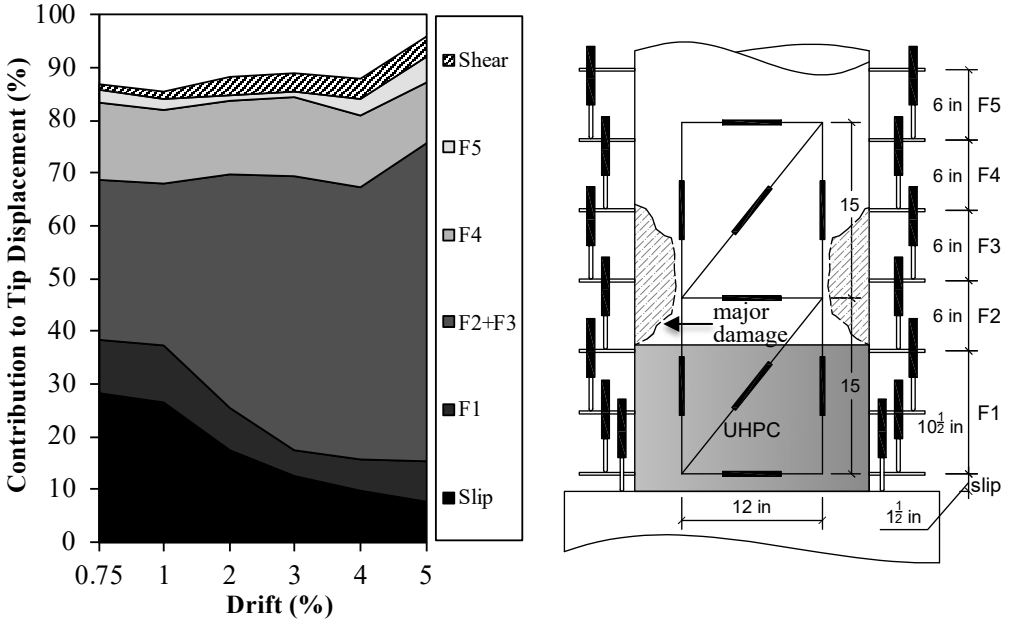

Figure 3.14: Plastic hinge deformation contributions of PCU40

3.2.6 Plastic Hinge Strain Profiles

Fig. 3.15 shows the plastic hinge strain profiles of the extreme NS and HS bars on the opposite sides of PCU40 from 0.25% to 5% drifts, when the strain gauges remained reliable. UHPC connection regions are marked with horizontal black dash lines, and yielding strains of both NS and HS bars are marked with vertical red dashed lines. It was observed that at every drift, strains of HS bars in the footing and UHPC connection region of PCU40 were

below yielding strains, indicating the linear elastic deformation as per the design objective. The peak strain of HS bars occurred at or slightly below the connection-footing interface.

The largest NS strains were located at the column-connection interface, where NS bars began yielding at 0.75% drift. At larger drifts, the inelastic responses of NS bars in the UHPC connection indicated strain penetration (slip) of NS bars into the UHPC connection. This resulted in minor splitting cracks of the connection observed during the test. The largest strain values between the column and connection interface of PCU40 were also consistent with the locations of rebar fracture, which were few inches above the interface. Well-distributed plastic reinforcing strains were evident above the UHPC connection. Bar yielding extended over 37% of the precast column shaft length (L'), showing a larger spread of PH length compared with the CIP column.

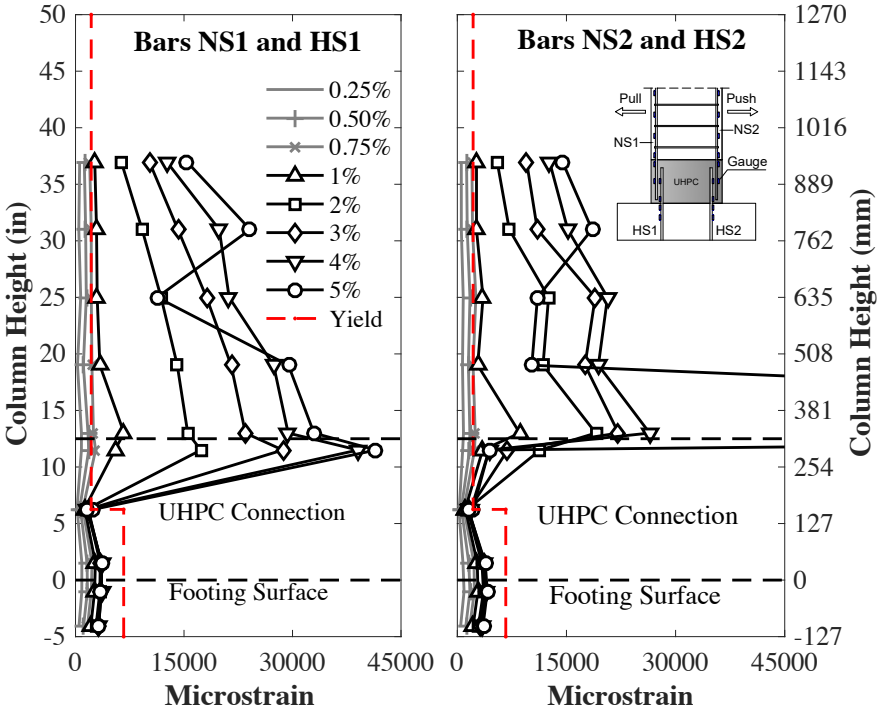

Figure 3.15: Strain profiles of longitudinal bars in the plastic hinge of PCU40

Fig. 3.16 depicts the force-strain hysteresis responses of the extreme NS bar at the

critical section and the extreme HS bar at the footing-connection interface up to 5% drift. The thin hysteresis loops of HS bar further confirmed the linear elastic response, low energy dissipation, and little strain penetration into the footing. On the other hand, the wide plastic force-strain hysteresis loops of NS bar indicated that the majority of strain penetration that ensured high energy dissipation and ductility of PCU40 occurred at the critical section into the UHPC connection.

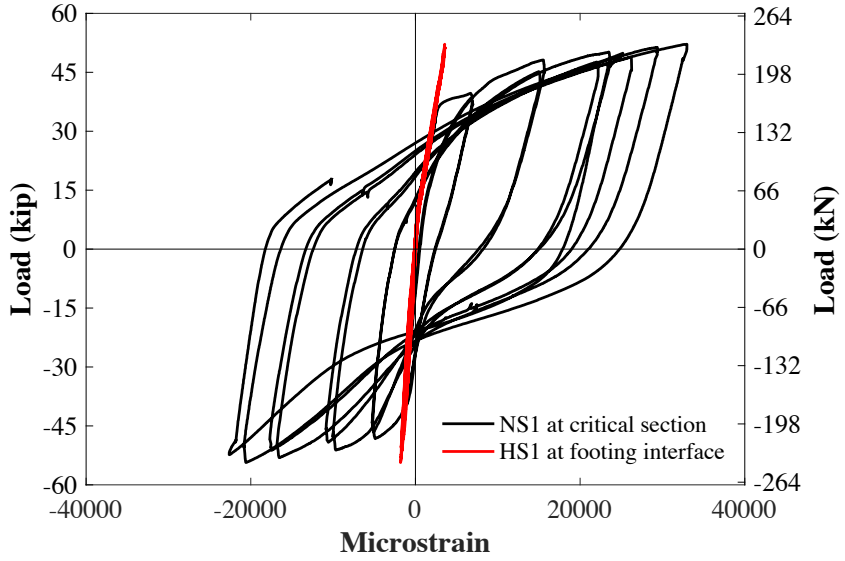

Figure 3.16: Force-strain at critical section of PCU40 (up to 5% drift)

3.2.7 Stress Transfer and Bond Strength in Spliced Region

Fig. 3.17 depicts the axial stresses within the extreme NS longitudinal column reinforcement and the HS footing bars at the south side and in the spliced region of PCU40. The bar stresses presented here were determined using stress-strain data captured from tension tests conducted on individual reinforcing bars. That is, bar stresses were determined by correlating strain data captured during column testing with the tension test data. The data presented in Fig. 3.17 corresponds to the measured strain data up to 6% drift, beyond which the strain measurements were not reliable. Δ_{fs} denotes the change in axial stresses:

between section A (critical section) and section B for NS bar, and between section C (footing interface) and section B for HS bar. Δ_{fs} provides additional information on the localized bond-slip effects.

The increasing bar axial stresses and the large magnitude of Δ_{fs} for NS bar up to 5% for PCU40 indicated good bond strength between UHPC and NS bar. At 6% drift, Δ_{fs} reduced significantly, indicating that localized microcracks and partial debonding may have occurred. Nevertheless, the NS bar maintained sufficient bond to enable bar fracture above the UHPC connection at 8% drift, as observed in the damage progression results. The large axial stresses and Δ_{fs} in HS bar at each drift ratio also showed the good bond strength between UHPC and HS bar. The gradual drop of HS bar axial stresses from 4% drift was due to the progressing UHPC splitting cracks along HS bars, which were caused by the radial stresses generated from the compressive strut between the NS bars in tension.

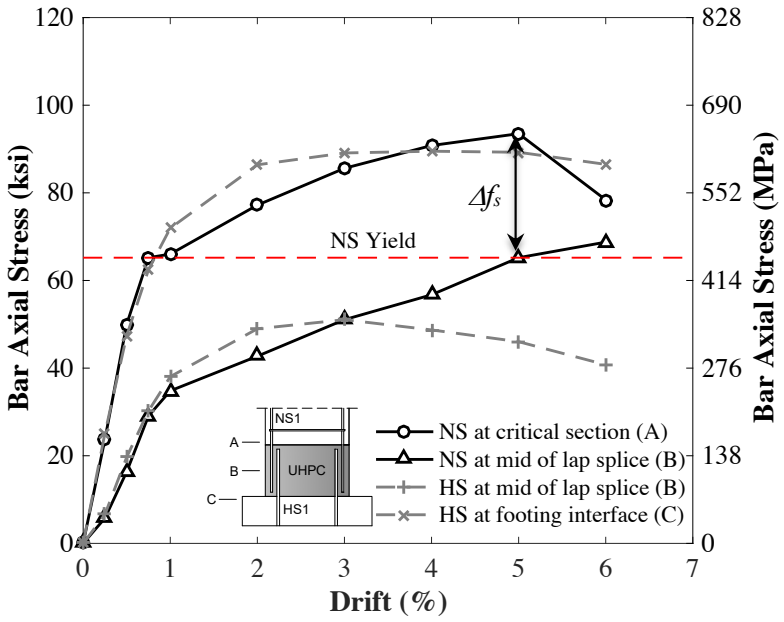

Figure 3.17: Extreme longitudinal bars axial stresses in the spliced regions of PCU40

3.3 Precast Column PCU25

3.3.1 Damage Progression

Fig. 3.18 to 3.23 show the damage progression of column PCU25 at every drift level inspected after each half drift cycle. Up to 1% drift (Fig. 3.18 and 3.19a), PCU25 experienced only hairline flexural cracks along the column shaft height. No crack was observed on the UHPC connection. At 2% drift, the column shaft developed fine inclined shear cracks with additional flexural cracks, while the existing flexural cracks started to localize. On the UHPC connection, several splitting cracks were observed along the spliced bars (Fig. 3.19b). At 3% drift, concrete cover began to spall on both sides of the precast column shaft (N and S). On the south side, PCU25 exhibited more significant damage patterns where the column shaft had more distributed flexural cracks, and splitting cracks on the connection had propagated to the connection base (Fig. 3.20). By the end of 4% drift, extensive cover spalling on both sides of PCU25 extended 5 in (127 mm) from the base of the column shaft, exposing the longitudinal and transverse reinforcement. Multiple closely spaced inclined shear cracks had formed on both sides (W and E) of UHPC connection. Yet, no cracking was observed on the footing of the precast column (Fig. 3.21).

At failure, the primary damage of PCU25 occurred above the UHPC connection region with no sign of footing damage, as expected. However, there were a few notable observations: (1) core crushing and cover spalling were less significant than PCU40, limited to 5 in (127 mm) above the UHPC region, (2) the increased shear intensity produced numerous but minor inclined shear cracks on UHPC connection and the precast column shaft, and (3) PCU25 failed at 5% drift due to extreme longitudinal bar pullout and critical UHPC splitting cracks at the south (S) side (Fig. 3.22) and at 6% drift due to extreme bar fracture at the north (N) side (Fig. 3.23).

Fig. 3.24 depicts the comparison between the damage progression of columns PCU25

and CIP25 at 6% drifts. CIP25 also experienced a typical bridge column failure mode due to inelastic strain penetration from the longitudinal bars into the footing. The failure initiated with core concrete crushing, followed by longitudinal bar buckling, and spiral fracture at the column base region. The footing concrete of CIP25 exhibited widened radial cracks at the footing surface. On the other hand, the significant damage above the UHPC connection and the undamaged footing of PCU25 indicated that PH formation was also successfully shifted. Longitudinal bar fracture and minor connection splitting cracks in the north side of PCU25 indicated the efficient use of UHPC in developing short lap-spliced reinforcement and damage-tolerant seismic connection. The bar pullout failure in the south side appeared to be due to the high shear demand of a typical short column combined with the large inelastic deformations.

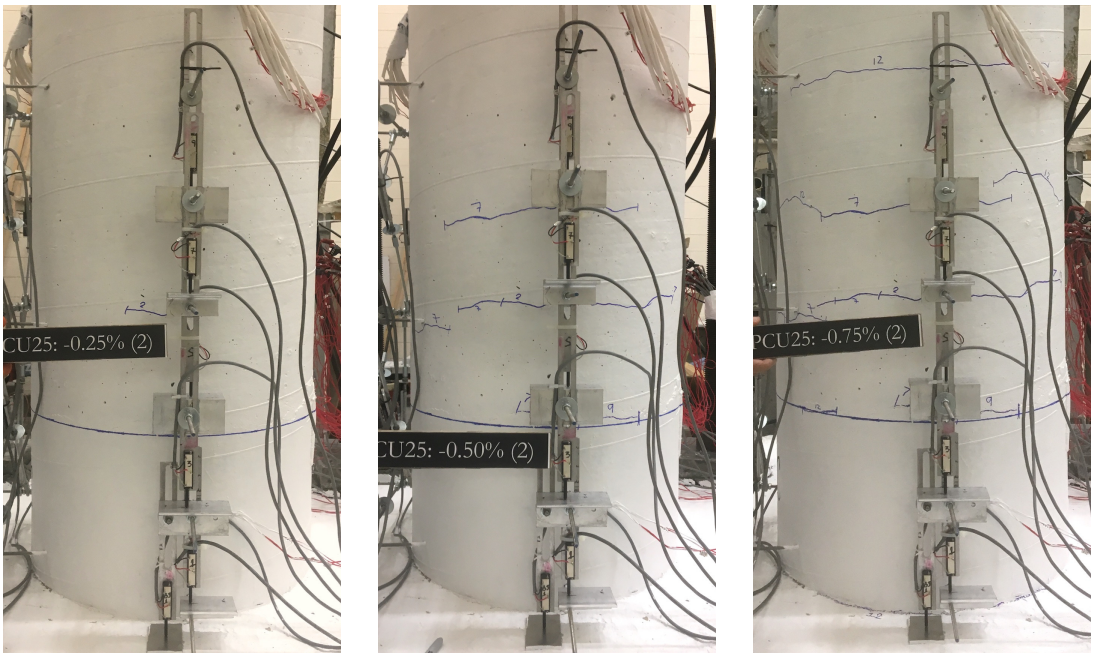

(a) 0.25% drift (North) (b) 0.50% drift (North) (c) 0.75% drift (North)

Figure 3.18: Observed damage of PCU25 prior to 1% drift (2nd cycle)

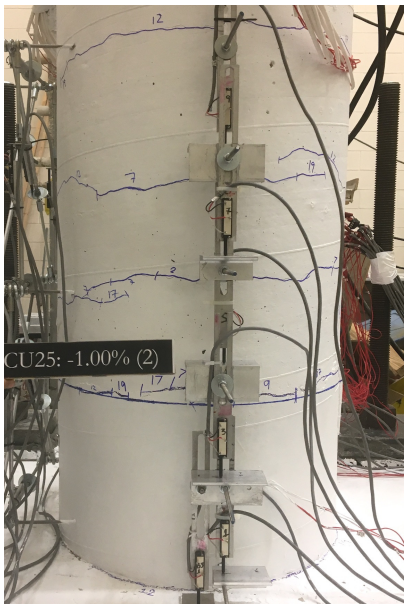

(a) 1% drift (North)

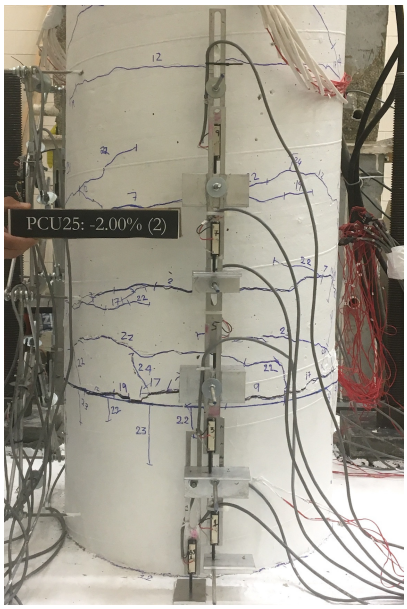

(b) 2% drift (North)

Figure 3.19: Observed damage of PCU25 of 1% and 2% drifts (2nd cycle)

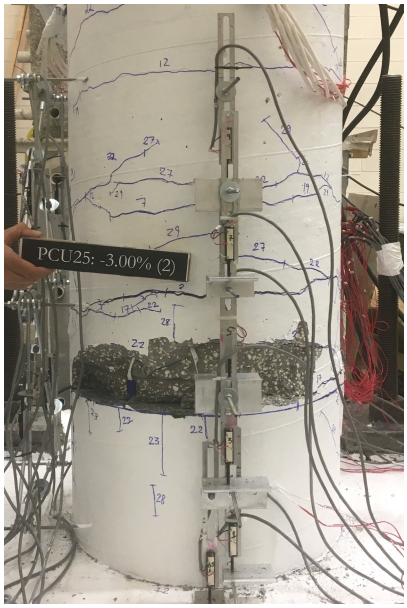

(a) North

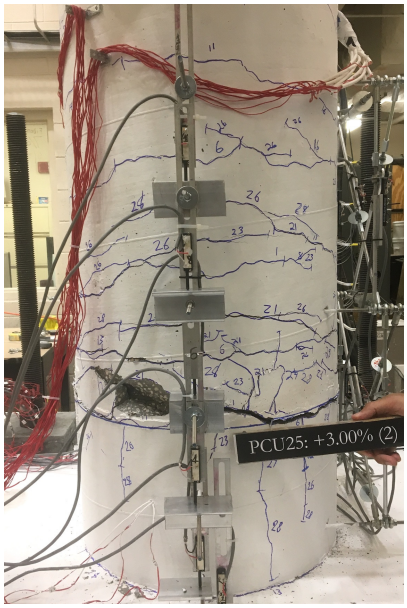

(b) South

Figure 3.20: Observed damage of PCU25 at 3% drift (2nd cycle)

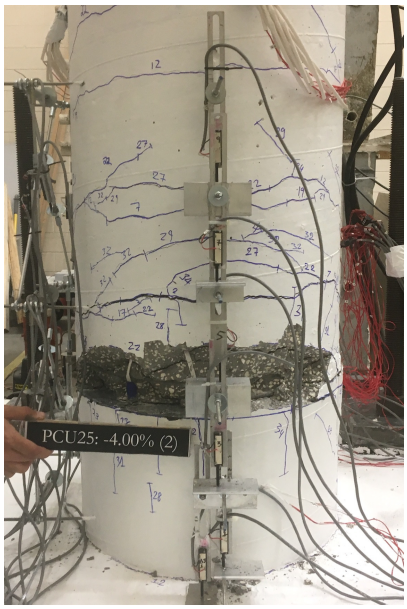

(a) North

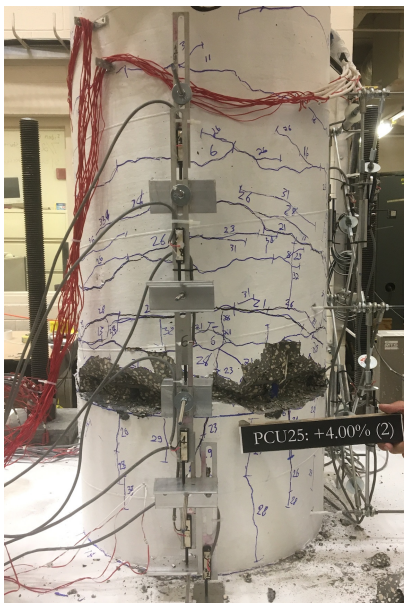

(b) South

Figure 3.21: Observed damage of PCU25 at 4% drift (2nd cycle)

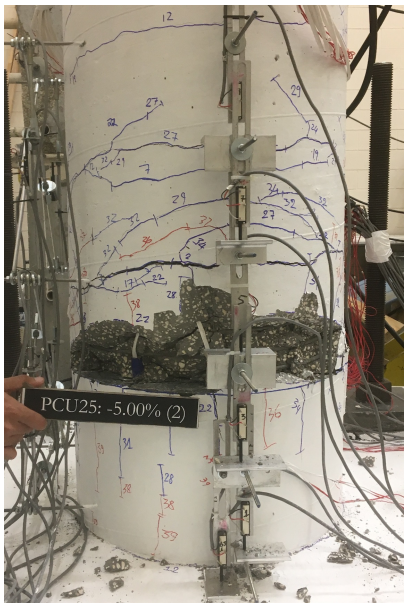

(a) North

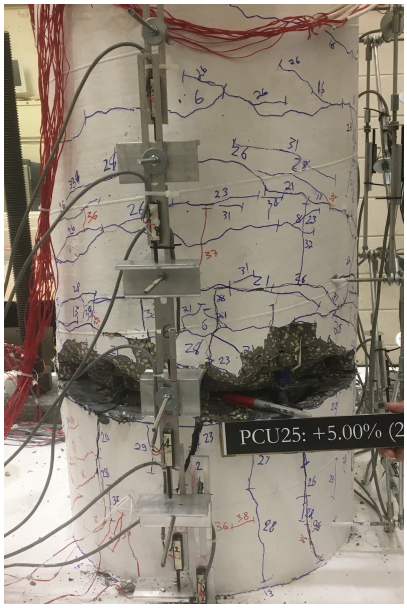

(b) South

Figure 3.22: Observed damage of PCU25 at 5% drift (2nd cycle)

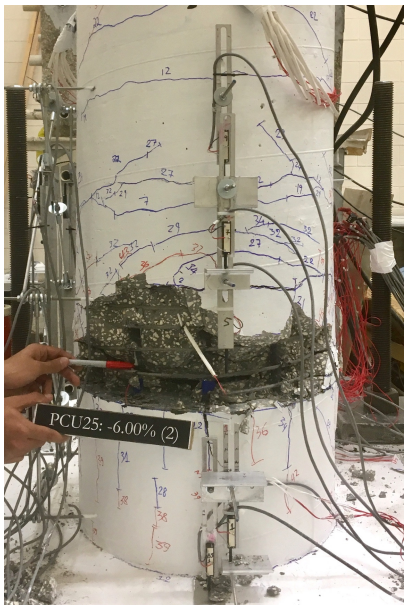

(a) North

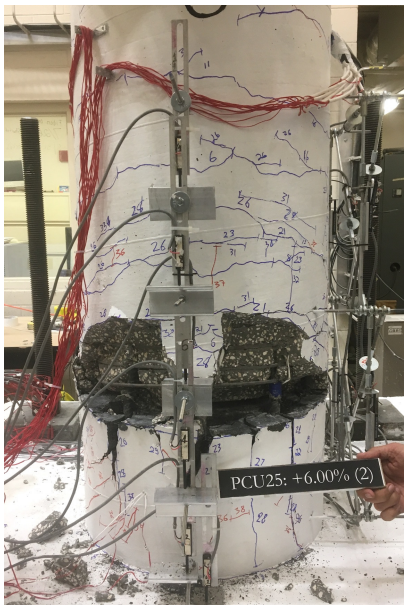

(b) South

(c) West

(d) East

Figure 3.23: Observed damage of PCU25 at 6% drift (2nd cycle)

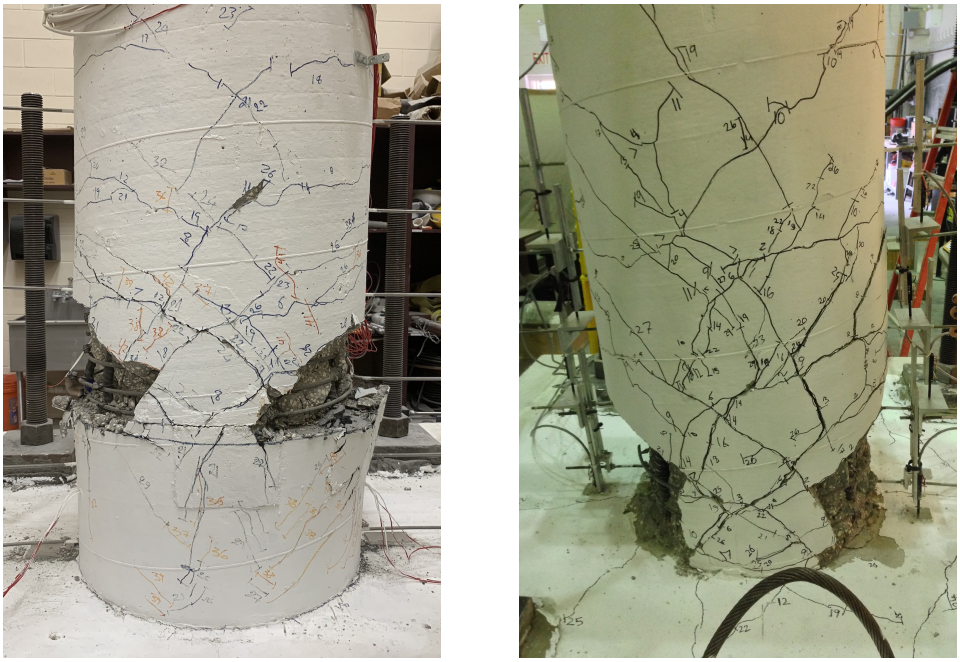

(a) PCU25 (West)

(b) CIP40 (West)

Figure 3.24: Comparison of damage pattern for AR = 2.5 columns at failure

3.3.2 Force-Displacement Relationship

The lateral force-drift hysteresis curves of PCU25 and CIP25 are shown in Fig. 3.25. The hysteresis curves were marked with important local events observed in the damage progression results that included onset of rebar yield, onset of cover spalling, concrete cover loss, spiral fracture, NS bar rupture, and debonding of NS-UHPC. Similar to AR = 4 columns, AR = 2.5 columns also exhibited stable hysteresis responses. CIP25 exhibited lateral load $V_p = 60.0$ kips (267 kN) and ductility $\mu_{avg} = 7.1$. On the other hand, PCU25 exhibited $V_p =$ 66.6 kips (296 kN) and $\mu_{avg} = 8.54$ (Fig. 3.26). The drop of lateral load was observed at 5% drift for PCU25 and 6% drift for CIP25. Despite the premature failure due to bar pullout at 5% drift at the south side, the average lateral load and ductility of PCU25 were approximately 11% and 20% higher than those of CIP25, respectively. The increase of achieved

concrete compressive strength (f'_c) compared with the assumed design f'_c, and the smaller yield displacements of PCU25 contributed to the larger lateral load and ductility of precast column, respectively, compared with CIP25.

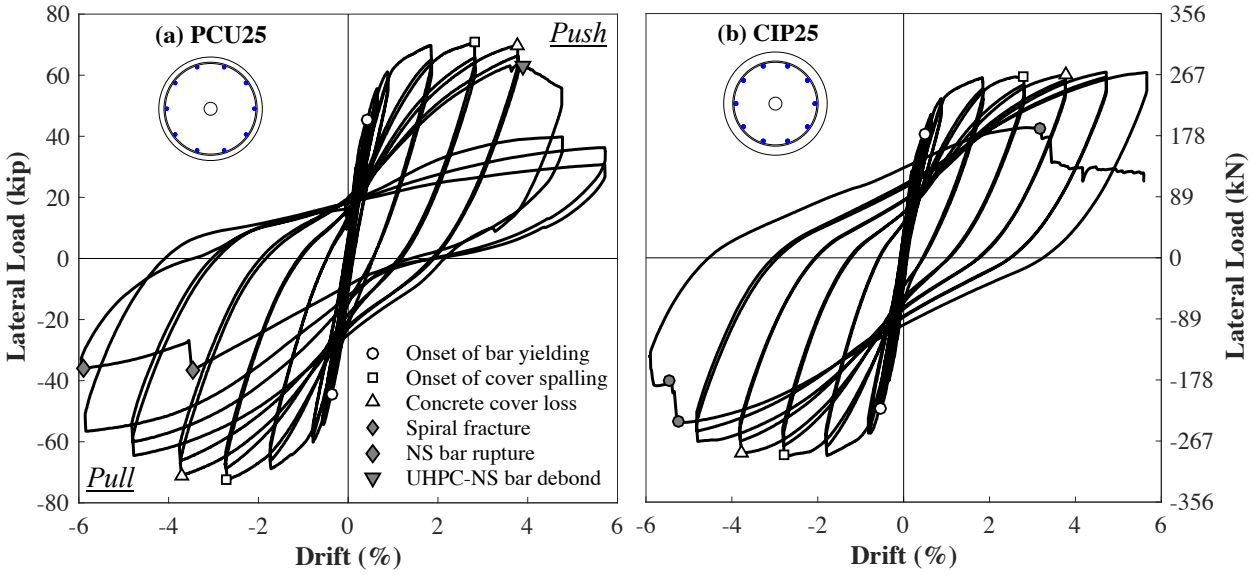

Figure 3.25: Force-drift relationships of AR = 2.5 columns

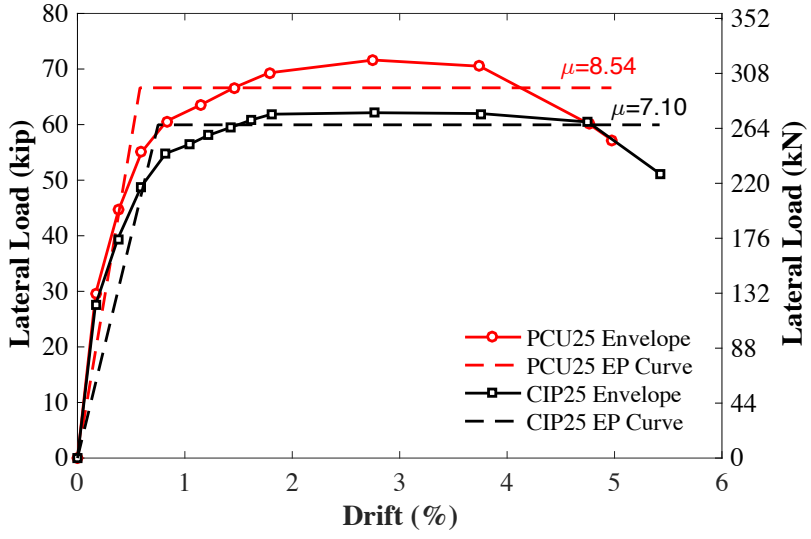

Figure 3.26: Average force-drift envelop of AR = 2.5 columns

3.3.3 Energy Dissipation

Fig. 3.27 depicts the average equivalent damping ratios (between the first and second loading cycles) of AR = 2.5 columns. Good energy dissipation and comparable damping ratios were also observed between the AR = 2.5 columns at nearly every drift level. Small ξ_{eq} were noted before 1% drift. After 1% drift when most extreme longitudinal bars yielded, the difference of ξ_{eq} between PCU25 and CIP25 on average was approximately 0.01. PCU25 had larger ξ_{eq} between 1% and 5% drifts that can be caused by the spread of bar yielding over a larger column height. Initiation of bar pullout on the south side of PCU25 at 5% drift did not reduce its energy dissipation, yet the complete bar pullout at 6% drift considerably reduced ξ_{eq} of the precast column to 0.023 lower than that of CIP25.

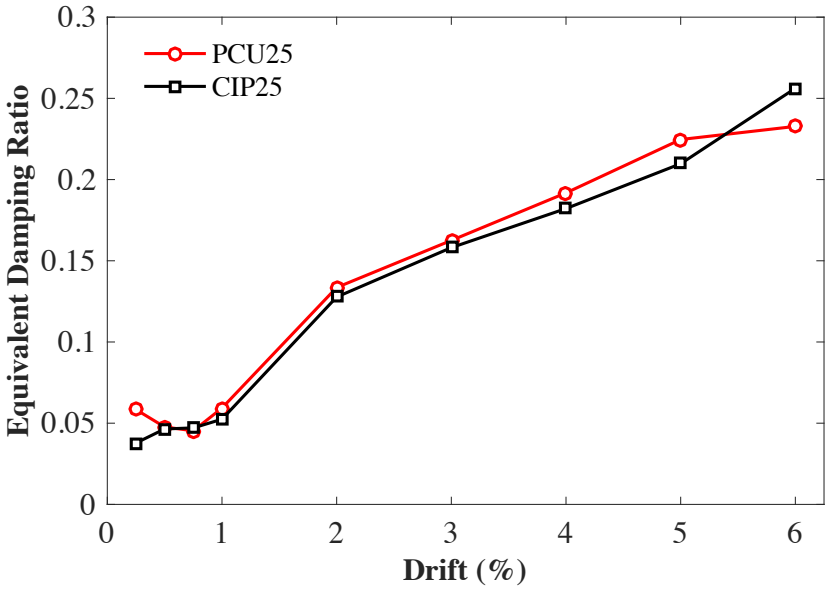

Figure 3.27: Equivalent damping ratios of AR = 2.5 columns

3.3.4 Plastic Hinge Curvatures and Base Moment Rotations

Curvature profiles of PCU25 and CIP25 from 2% to 5% drifts are illustrated in Fig. 3.28. The curvatures of AR = 2.5 columns showed the same patterns as AR = 4 columns, where the CIP column exhibited maximum curvatures at the column base corresponding to the major damage location, the precast column curvatures were largely concentrated at the column-UHPC connection interface, and the curvatures on UHPC connection were relatively small. The hysteretic base moment-rotations of PCU25 at the column base (bond slip) and at column-connection interface (section F2) are shown in Fig. 3.29. The thin hysteretic $M - \theta$ curve at the connection base proved the stiff response of UHPC connection despite the bar pullout failure. It can be noted that the moment-rotation hysteresis loops of PCU25 at section F2 were wider than those of PCU40 as bar pullout occurred.

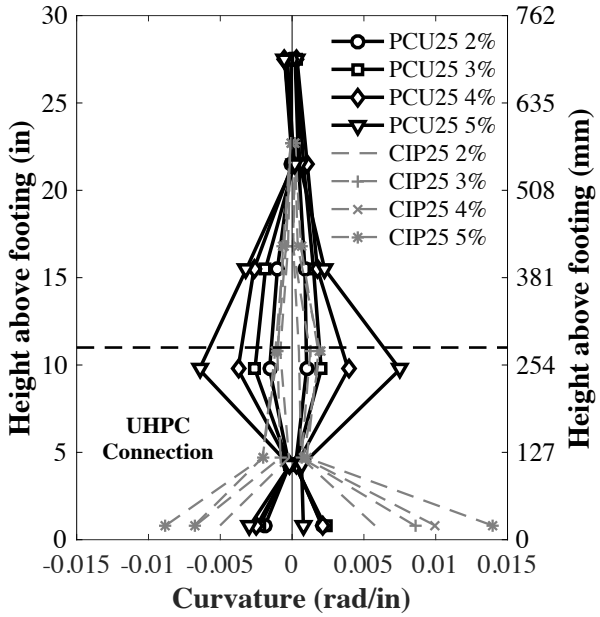

Figure 3.28: Plastic hinge curvature of AR = 2.5 columns

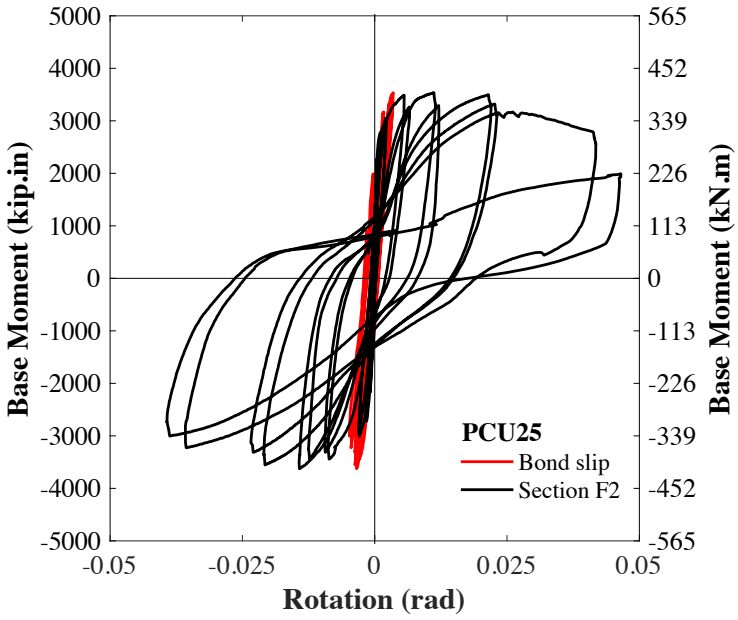

Figure 3.29: Base moment rotation of PCU25

3.3.5 Plastic Hinge Deformations

Fig. 3.30 shows the PH deformation contribution to the tip displacement of PCU25 during the first cycle pushover load from 0.75% to 5% drifts with schematic of the LVDT instrumentation used to capture the deformation responses. At early drift (prior to 1%), bond-slip due to strain penetration of well-anchored dowels generated approximately 30% of the total column tip displacement. Yet, the contribution continuously dropped to less than 3% by the end of 5% drift due to same linearly elastic response of HS footing dowels as observed in PCU40. Flexural deformations at locations F1, F4, and F5 contributed lower than 10% of the total tip displacement at any drift levels. The majority of tip displacement was caused by the flexural deformation in the major damage region (F2+F3) that includes both flexural deformation and bond-slip between UHPC and NS bars. The F2+F3 deformation contributed 30% at the onset of NS bar yielding and increased to approximately 80% at 5% drift, which was governed by bar pullout. The high shear intensity of PCU25 only increased

the shear deformation contribution to 8% (from 4% in PCU40) of the column tip displacement. The PH deformation results of PCU25 not only confirm the low strain penetration of HS footing dowels and the significant role of NS bar slip in the UHPC connection as observed in PCU40, but also indicate that shear deformation was not significant although transverse reinforcement was not used within the connection.

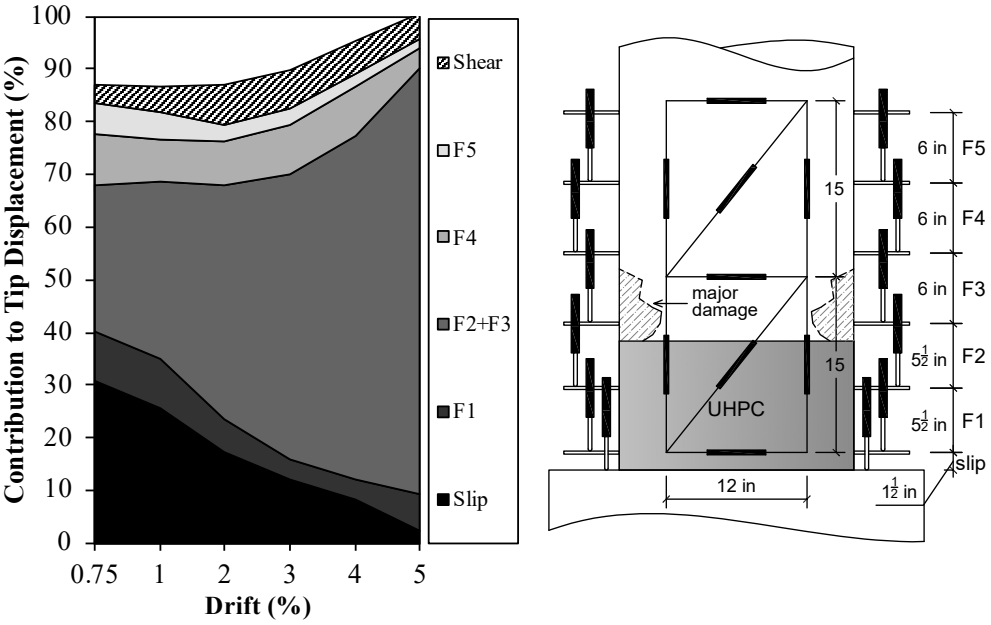

Figure 3.30: Plastic hinge deformation contributions of PCU25

3.3.6 Plastic Hinge Strain Profiles

Fig. 3.31 depicts the PH strain profiles of the extreme NS and HS bars of PCU25 from 0.25% to 4% drifts. The UHPC connection region is marked with horizontal black dash lines, and yielding strains of both NS and HS bars are marked with vertical red dashed lines. The strain results of PCU25 were consistent with the design objectives and with those of PCU40, where HS bar strains of PCU25 were lower than the yielding strain that confirmed the linear elastic behavior, and NS bars exhibited highly inelastic responses in the UHPC

connection indicating NS bar slip in the connection. At 0.50% drift, NS bars on both sides of PCU25 began yielding. With increasing drift levels, bar yielding extended over 53% of the precast column shaft length (L'), displaying well-distributed plastic reinforcing strains above the UHPC connection. This showed that PCU25 had a larger spread of PH length than the CIP column and PCU40. The early and high slippage of UHPC-NS bars may contribute to the larger PH length in PCU25.

Fig. 3.32 shows the force-strain hysteresis responses of the extreme NS bar at the critical section and the extreme HS bar at the footing-connection interface up to 4% drift. Similar to force-strain history in PCU40, thin hysteresis loops were observed in HS bar, while wide hysteresis loops were seen in NS bar. This indicated lower strain penetration into the footing than into the UHPC connection.

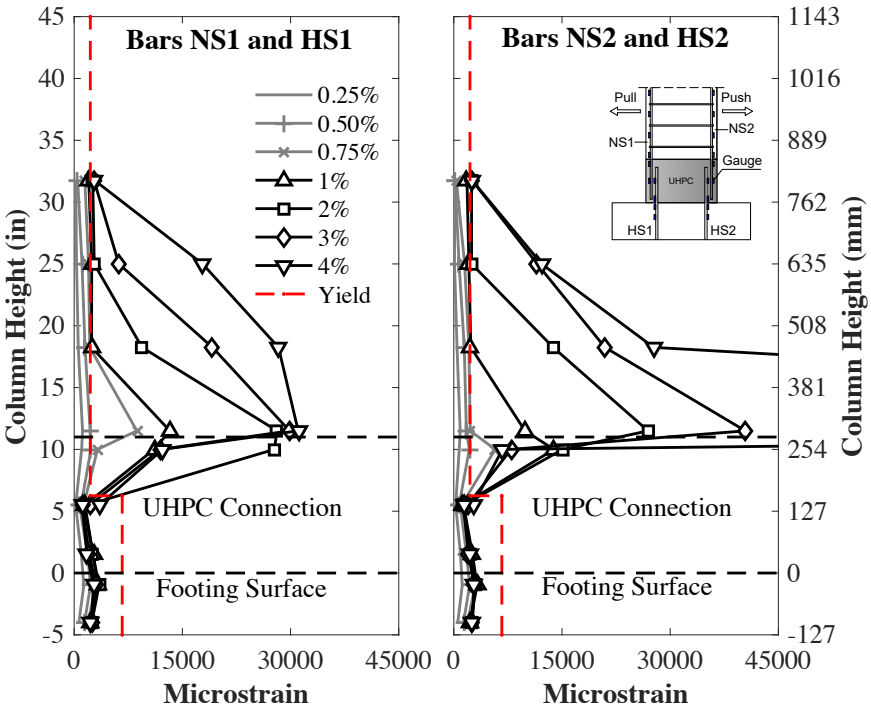

Figure 3.31: Strain profiles of longitudinal bars in the plastic hinge of PCU25

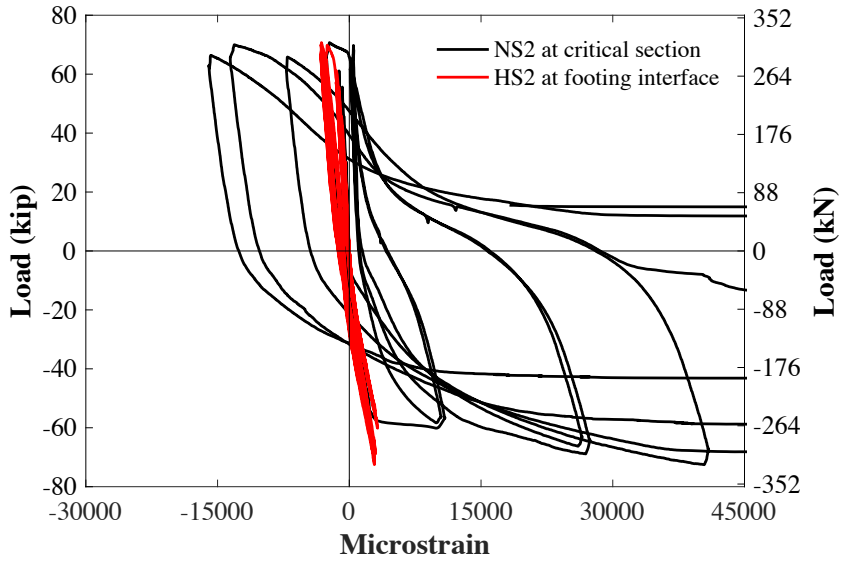

Figure 3.32: Force-strain at critical section of PCU25 (up to 4% drift)

3.3.7 Stress Transfer and Bond Strength in Spliced Region

Fig. 3.33 shows the axial stresses within the extreme NS longitudinal reinforcement and the HS footing bars in the spliced region at the south side of column PCU25 up to 4% drift when strain measurements remained reliable. Δ_{fs} represents the change in axial stresses: between section A (critical section) and section B for NS bar, and between section C (footing interface) and section B for HS bar. Similar axial stress responses in NS and HS bars to PCU40 were observed in PCU25. Good UHPC-NS bar bond strength up to 2% was evident as the NS bar stresses at sections A and B kept increasing and Δ_{fs} remained considerably large. However, the high shear intensity of the column caused early UHPC splitting cracks and partial debonding along NS bars and therefore a reduction of Δ_{fs} at 3% and 4% drifts. Splitting cracks along HS also occurred early at 3% drift. Bond strength between UHPC and rebar remained high at these drift levels, but a rapid drop of Δ_{fs} in NS and HS bars is expected when bar pullout occurred.

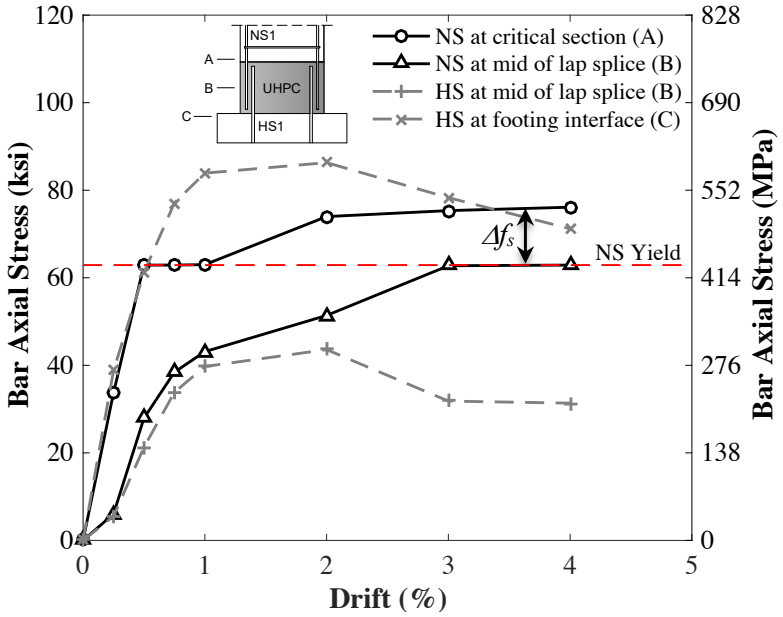

Figure 3.33: Extreme longitudinal bars axial stresses in the spliced regions of PCU25

3.4 Comparisons with Previous Column Models

This section compares the performance of PCU40 and PCU25 with previously investigated seismic columns utilizing UHPC, which include UHPC-filled duct [28] and UHPC hybrid systems [30]. Currently proposed UHPC connection is also compared with GS connection that used the same SPH concept studied by Al-Jelawy et al. [48]. Comparison is made in terms of lateral capacity, displacement ductility, failure modes, and construction feasibility. Performance comparison to UHPFRC jacket and other non-emulative systems using UHPC connection is not possible because the systems were designed with different performance objective. Table 3.1 summarizes the performance comparison.

3.4.1 Lateral Capacity and Displacement Ductility

Each column being compared was designed to have similar performance as a reference CIP column. Therefore, the lateral capacity and displacement ductility were compared

relative to the reference columns. The load and ductility ratios were respectively 1.10 and 1.02 for PCU40, and 1.11 and 1.20 for PCU25. The 10% improved lateral load was caused by the increase of f'_c from the expected design f'_c of 5 ksi, while the higher ductilities were attributed to the shift of PH formation and slip of NS bars in UHPC connection. Precast columns using GS connection that had the same reference CIP columns as PCU columns exhibited load and ductility ratios of 0.86 and 0.90 for AR = 4 column, and 1.02 and 0.81 for AR = 2.5 column. Al-Jelawy et al. [48] concluded the lower load of AR = 4 column and reduced ductility of AR = 2.5 column were caused by the reduced cover due to construction error, and the higher shear demand and deformation, respectively. Precast column using UHPC-filled duct connection is a half-scale column with AR of 4.5. The column had load and ductility ratios of 0.98 and 0.86 (μ_{avg} of 6.30 compared with 7.36 of CIP column), respectively. Tazarv and Saiidi [28] concluded the lower ductility of 14% was attributed to the lower f'_c of the concrete shell compared with that of reference CIP column, which reduced the column resistance against bar buckling. On the other hand, load and ductility ratios of the quarter-scale UHPC hybrid column were 1.01 and 0.88, respectively. The high compressive strength of UHPC may prevent the material from attaining the full dilation and crushing strain capacity, resulting in 12% reduction of ductility.

3.4.2 Failure Modes

Fig. 3.34 shows the comparison of failure modes between PCU40, GS AR = 4, and UHPC-filled duct columns having similar AR. PCU40 showed the shift of PH formation above the connection region and failed due rebar rupture. The UHPC connection exhibited several splitting but still maintained high stiffness (Fig. 3.34a). GS column experienced similar failure mode to PCU40 with the shift of PH formation and bar rupture above the connection. However, the GS connection underwent significant cover spalling (Fig. 3.34b). UHPC-filled duct was designed to emulative CIP column. The column PH occurred directly

above the footing surface. The column ultimately failed due to bar fracture above the footing-column interface. No bond failure of rebar embedded in UHPC was observed (Fig. 3.34c). Detailed failure patterns of UHPC hybrid system was not fully described. Only flexural cracks around the UHPC region were reported. In an earthquake event, failure with the shift of PH formation provides additional benefit by preventing damage to capacity protected members and rupture of longitudinal reinforcement at the footing-column interface. This lowers the repair and replacement time and cost.

(a) PCU40 (b) GS AR = 4 [48] (c) UHPC-fil. duct [15]

Figure 3.34: Failure mode comparison between different column models

3.4.3 Construction Feasibility

UHPC lap splice, GS, and UHPC-filled duct connections were proposed for ABC, in which precast column shaft and footing or bent-cap were constructed off-site and delivered for quick on-site installation. All the three systems provide similarly accelerated construction procedures, where minimal bracings are required to provide lateral stability and vertical alignment of the column shaft. For UHPC lap splice and GS connections, UHPC or grout

is filled after the precast column is braced, whereas UHPC-filled duct connection requires UHPC to be filled prior to column shaft installation and bracing.

Table 3.1: Comparisons with previous column models

Reference	Column ID	Scale[c]	AR	Description	Load (ksi)	Ductility	Ratio[b]	
							Load	Ductility
Current Study	CIP40[a]	0.42	4	PCU40 reference column	44.8	7.75	-	-
	PCU40	0.42	4	Precast AR = 4 using UHPC lap splice	49.3	7.90	1.10	1.02
	CIP25[a]	0.42	2.5	PCU25 reference column	60.0	7.10	-	-
	PCU25	0.42	2.5	Precast AR = 2.5 using UHPC lap splice	66.6	8.54	1.11	1.20
Al-Jelawy et al. [48]	CIP40[a]	0.42	4	G-40-1 reference column	44.8	7.75	-	-
	G-40-1	0.42	4	Precast AR = 4 using GS	37.0	7.00	0.83	0.90
	CIP25[a]	0.42	2.5	G-25-1 reference column	60.0	7.10	-	-
	G-25-1	0.42	2.5	Precast AR = 2.5 using GS	61.2	5.60	1.02	0.79
Tazarv & Saiidi[28]	CIP	0.5	4.5	PNC reference column	65.0	7.36	-	-
	PNC	0.5	4.5	Precast column using UHPC-filled duct	63.7	6.30	0.98	0.86
Zohrevand & Mirmiran [30]	RC	0.25	5	RUHPC reference column	17.6	5.40	-	-
	RUHPC	0.25	5	Hybrid UHPC column	17.7	4.80	1.01	0.89

[a] denotes CIP columns tested by Al-Jelawy et al. [48]
[b] denotes the ratio of precast column capacity relative to reference columns
[c] scale is relative to an assumed full-scale column with 48 in diameter
Notes: 1 ksi = 6.9 MPa; 1 in = 25.4 mm

CHAPTER 4: BOND INVESTIGATION OF REINFORCING STEEL EMBEDDED IN UHPC

4.1 Introduction

Results of the two 0.42-scale columns showed the successful use of UHPC connections having short lap splice length, practical concrete cover, and no shear reinforcement as damage-tolerant precast seismic bridge connections. The precast columns exhibited large lateral load capacity and higher displacement ductility than the reference CIP columns due to two main contributions: the shift of PH formation and the bond-slip of NS longitudinal bars into UHPC connection. The latter was the larger contributing factor to the tip displacement. It is important to note that the splice length selection of $12d_b$ (around $13d_b$ embedment length and cover ranging from 1.4 to $1.7d_b$) for the UHPC connection was approximated based on the design guidance and bond investigation under monotonic loading until failure by Graybeal [46] and Yuan and Graybeal [47]. Monotonic tension-tension bond pullout tests conducted by Yuan and Graybeal [47] found that NS and HS steel bars embedded $10d_b$ in UHPC (approximately 30% shorter than current study) with $2d_b$ of clear cover could sustain tensile stresses as high as 91.8 ksi (633 MPa) and 130 ksi (896 MPa), respectively prior to bond failure.

Column test results in the spliced region showed that the maximum stresses observed in the extreme NS and HS bars were 91.3 ksi (630 MPa) and 93.3 ksi (643 MPa), respectively for column PCU40, and 78.3 ksi (540 MPa) and 84.4 ksi (582 MPa), respectively for PCU25. The data is comparable to the monotonic pullout tests although the experimental parameters differ. PCU25 exhibited bond failure between the UHPC and steel reinforcement, which occurred at approximately 15% and 35% lower axial stress in the NS and HS bars. The observed lower axial stress in NS bar and reduced bond strength in PCU25 were caused by

the combined large inelastic deformations, cyclic loading, and high shear demands. For HS bar, the lower axial stress was caused by the radial stresses generated from the compressive strut between the NS bars in tension, rather than bond failure.

However, the larger side cover, higher bar strength, and higher confined pressure provided by the selected test setup may also contribute to the large bond strength and bar stresses in Yuan and Graybeal [47]. On the other hand, recent experimental investigations on bond strength of reinforcing steel embedded in UHPC ([65], [66], and [67]) indicated similar or lower axial bar stresses and bond strength than the column tests. This indicates that the existing UHPC bond strength test data in the literature has a large deviation, requiring further investigation.

The objective of this chapter is to investigate the local bond-slip behavior of reinforcing steel embedded in UHPC that has small side cover that corresponds to the column design parameters and where existing data is insufficient. Several other parameters were considered including splice length, bar size, and bar strength. Two types of experiments were used: (1) a simplified unconfined direct tension pullout test and (2) beam lap-splice test. The first experiment was utilized to simulate the UHPC column connection condition without confined transverse reinforcement, while beam test provided additional information on UHPC lap splice bond under bending stress. This chapter presents past research on bond of reinforcing steel embedded in UHPC, detailed experimental program, and experimental results with focus on the achieved maximum bar stress at failure, effects on bond strength under different parameters, and the observed failure modes.

4.2 Past Studies of UHPC-Rebar Bond Behavior

Although UHPC exhibits superior compressive and tensile strength comparing to conventional concrete, complementary reinforcing steel remains necessary to fully utilize

the high UHPC compressive strength, secure tensile ductility, and obtain reliable structural elements. The composite action of a typical RC element is ensured by bond performance between concrete and reinforcing steel, resulting from the combination of chemical adhesion, friction, and mechanical interlock. As load is transferred from the deformed bar along the ribs, compressive struts are formed and balanced by tensile rings of concrete. With ultra-fine granular materials and high strength microfibers, UHPC offers outstanding gripping effect and tensile strength that effectively resist the radial stress generated by the compressive struts; therefore, significantly enhances bond strength. Previous research has indicated that the bond strength of deformed bars embedded in UHPC was significantly higher than that of deformed bars embedded in conventional concrete, grout, and cementitious materials. The bond strength is affected by UHPC compressive strength, fiber content, side cover, embedment length, bar spacing, bar strength, and the confined pressure provided by different test setups. The existing literature of bond strength of deformed bars embedded in UHPC over the last decade is briefly described as below and summarized in Table 4.1.

4.2.1 Conventional and Modified Confined Pullout Tests

As part of an experimental program conducted to study the structural performance of field-cast UHPC connections for modular bridge deck, Graybeal [60] investigated the development length of mild reinforcing steel embedded inside UHPC. The test included three rebar sizes #4 (M13), #5 (M16), and #6 (M19), which were embedded 5.8, 6.3, and $6.5d_b$, respectively, into a 15.75 in diameter UHPC cylinder (cover ranging from 10 to $15d_b$) and were tested using conventional pullout test setup. Results showed that all specimens failed due to rebar rupture at the stresses between 100 and 108 ksi (692 and 743 MPa), indicating development length as low as 5.8 is sufficient to fully develop mild reinforcement.

Saleem et al. [61] studied the bond performance of HS steel Gr. 100 embedded in UHPC using two rebar sizes #3 (M10) and #7 (M22) and four embedment length 8, 10, 12,

and $18d_b$. A single side cover of 0.5 in (13 mm) was used to match the design parameter for light-weight UHPC-HSS bridge movable deck system investigated by Saleem et al. [44]. This resulted in the side cover of 0.6 and $1.3d_b$. The specimens were pulled against a fixed steel plate in which reinforcing bar was subjected to tension force while concrete was subjected to compression force. This traditional pullout test setup is known to enhance bond strength as concrete in compression reduces the significance of radial stresses formed by bar ribs in the concrete. Based on the pullout test results, Saleem et al. [61] concluded the development length for #3 (M10) embedded in UHPC is $12d_b$. On the other hand, bond of all #7 (M22) rebar with side cover of $0.6d_b$ was disturbed by stress concentration around the bearing area, leading to premature bond failure prior to the HS bar yielding strain.

Alkaysi and El-Tawil [62] performed pullout tests using four small steel plates to support the edge areas of UHPC cube, distancing the concrete around reinforcing steel from compressive struts. A total of 55 specimens were tested to study the effects of embedment length, bar coating and diameter, casting orientation, fiber content (1% and 2%), and curing age. Uncoated and epoxy coated #4 (M13) to #6 (M19) Gr. 60 bars with the embedment lengths from 2.6 to $8d_b$ were used. The results showed the increased embedment length adversely affected bond strength and bar stress. Bond strength was increased between 21% and 36% with the increased fiber content. Bond strength in UHPC was conservatively estimated to be $0.42\sqrt{f'_c}$ (ksi) or $1.1\sqrt{f'_c}$ (MPa).

Yuan and Graybeal [47] and Haber and Graybeal [63] used a modified pullout test to mimic the tension-tension lap splice configuration. The specimens were constructed by casting a precast NSC slab that had extending bars for anchoring UHPC strips atop. A series of test bars were positioned in the UHPC strips between the anchored bars. Yuan and Graybeal [47] tested over 200 specimens to study the effects of embedment length, side cover, bar spacing, concrete strength, bar size, bar type, and yielding strength on bond strength. Yuan and Graybeal [47] concluded that bond strength of deformed bar in UHPC increased

with the increase of embedment length, side cover, and the use of non-contact lap splice. The bond strength was decreased with larger bar diameter. The following embedment length and side cover were recommended to develop uncoated and epoxy-coated #4 to #8 bars having yield strength of 75 ksi (517 MPa) embedded in UHPC with a minimum strength of 13.5 ksi (93 MPa): a minimum embedment length of $8d_b$ and cover of $3d_b$ or embedment length of $10d_b$ and cover between 2 and $3d_b$. On the other hand, Haber et al. [63] investigated the effects of five different UHPC-class materials and fiber volume fraction (1%, 2% and 3%). The five UHPC-class materials showed consistent bond strength results with Yuan and Graybeal [47]. Additional findings indicated bond strength increased with the increase of fiber content and a minimum embedment length of $10d_b$, and cover between 1.56 and $3d_b$ was suggested to develop 75 ksi (517 MPa) yield strength deformed bars.

4.2.2 Unconfined Direct Tension Pullout Tests

Fehling et al. [64] performed a total of 20 direct tension pullout tests using #4 (M12) bars with side cover ranging from 1 to $2.5d_b$ and embedded between 2 to $12d_b$ in UHPC rectangular blocks. Confinement with transverse steel was provided on one side to induce failure on the other side. Test results showed that specimens with concrete cover of $1d_b$ and embedment length up to $12d_b$ was unable to develop Gr. 80 rebar. Specimens with concrete cover of 1.5, 2, and $2.5d_b$ required the embedment length of 8, 6, and $5d_b$, respectively to yield Gr. 80 rebars having yield strength of approximately 84 ksi (580 MPa). A few failure modes occurred in the tests in which cone failure was observed on specimens with large concrete covers and short embedment lengths, while mixed splitting crack failures were observed on specimens with small covers and large embedment lengths.

Lagier et al. [65] investigated the bond performance of NS reinforcing steel (yield strength of 66.7 ksi (460 MPa)) in UHPFRC subjected to unconfined direct tension pullout test. Two pairs of spliced deformed bars cast inside a UHPC block (without transverse

steel) were fixed by the top and bottom steel beams to ensure symmetric loading. Load was applied to the two top bars using displacement control. Three varying parameters were studied including bar size #8 (M25) and #11 (M35), fiber content (1%, 2%, and 4%), and embedment length (5, 8, 10, 12, and $18d_b$). The findings showed that the bar stress non-linearly increased with the increase of splice length. Higher fiber content not only increased bond strength but also delayed crack propagation. UHPFRC with 4% fiber content exhibited an average bond strength of 1.45 ksi (10 MPa) and required an an embedment length of $12d_b$ and a minimum cover of $1.2d_b$ to yield Gr. 60 reinforcing steel.

Zhou and Qiao [66] employed similar modified direct tension pullout test setup to that of Yuan and Graybeal [47]. However, the bottom bars were replaced with threaded rods and anchored against steel plate. This reduced the confinement provided by NSC precast slab as in previous test setup [47]. Consequently, the test is considered unconfined pullout test in this literature review. The test was utilized to study the effects of different UHPC mixture, embedment length (8 to $14d_b$) and side cover (1.6 and $3.2d_b$) of the bond behavior of epoxy rebar (#5 (M16)) embedded in UHPC. Results showed no significant effects between different UHPC mixtures. All specimens except those with side cover of $3.2d_b$ and embedment length of $14d_b$ were unable to reach bar yielding stress of 75 ksi (517 MPa). The suggested average bond strength and embedment length required to yield epoxy-coated Gr. 60 rebars were respectively 1.1 ksi (7.5 MPa) and 14 d_b with side cover of $1.6d_b$, and 1.4 ksi (9.7 MPa) and 10.8 d_b with side cover of $3.2d_b$.

Ronanki et al. [67] studied the effects of embedment length (6 to $10d_b$) and concrete cover (1.6 to $3.5d_b$) using a modified direct tension pullout test to eliminate the compressive stress observed in traditional pullout test setup. Each specimen incorporated two rectangular UHPC blocks having an extending test bar embedded. The two blocks were connected with two intermediate bars. The extending bars were subjected to tension forces. Consistent results with previous tests were observed where the increase of cover or embedment length

improved reinforcing steel bond performance in UHPC. It was concluded that bond strength varies between 1.4 and 2.4 ksi (9.7 and 16.6 MPa). To develop Gr. 60 rebar having yield stress of 60 ksi, Ronanki et al. [67] recommends the use of $10d_b$ embedment length with a minimum concrete cover of $2d_b$ or $8d_b$ embedment length with a minimum cover of 3.5.

4.2.3 Beam Lap Splice Tests

Bond conditions of flexural members are typically subjected to a combined axial, shear and bending stress states. The pullout test is the most commonly used bond test setup due to the ease of specimen design, instrumentation, and testing, but does not represent the actual stress states of flexural members. Previous studies showed that pullout test underestimated bond strength of tension reinforcing bars in concrete, while beam tests predicted the bond strength more accurately ([68] and [69]). Limited beam tests were performed to study bond behavior of reinforcing steel in UHPC. Saleem et al. [61] used T-section beams to determine embedment length required to develop #3 (M10) and #7 (M22) HS Gr. 60 bars having clear concrete cover of 0.5 in (13 mm). All specimens with embedment length smaller than $14d_b$ were unable to reach yielding strain as the results of premature failure. It was concluded with limited data points that embedment length of $18d_b$ was required to develop #7 (M22) HS Gr. 100 bar.

Ronanki et al. [67] performed a total of 12 beam tests with reinforcing steel spliced at beam mid-span region to investigate bond stress distribution and the effects of different covers (1.3 to $3d_b$) on bond performance of reinforcing steel in UHPC under bending stress. A constant splice length of $8d_b$ was utilized. The findings showed that all beams exhibited flexure and/or shear failures, resulting in a lower bound estimate of bond stresses for rebar in UHPC. Beams with concrete cover below $2d_b$ did not reach bar yield strain. Concrete cover between $2d_b$ and $3d_b$ is required to development Gr. 60 bar. It was also observed that the majority of force is transferred in the first $3d_b$ of embedment length.

Table 4.1: Past studies on bond of reinforcing steel embedded in UHPC

Test method	Past studies	Rebar (US)		Side Cover (d_b)	Embed-length (l_d)	UHPC fiber content	Test Results	
		Size	Grade (Yield)				Bar Stress (ksi)	Failure Mode
Confined Pullout Test	Graybeal [60]	#4 - #6	60	10 -15	5.8 - 6.2	2%	100 - 108	BF
	Saleem et al. [61]	#3, #7	100	0.6 - 1.3	8 - 18	2%	26 - 121	SF
	Alkaysi and El-Tawil [62]	#4 - #6	60 (60 - 73)	3.4 - 5.3	2.6 - 8	1% - 2%	27 - 88	SF, CF, & BF
	Yuan and Graybeal [47]	#5	120	2 - 3.5	3.75 - 10	2%	44 - 165	SF & CF
		#5	120	2	4 - 10	2%	43 - 144	SF & CF
		#5	60 (75)	2	4 - 10	2%	45 - 95	SF & CF
		#5	60 (75)*	2	4 - 10	2%	37 - 92	SF & CF
	Haber et al. [63]	#5	100	3	8, 10	1% - 3%	87 - 145	SF, CF, & BF
Unconfined Pullout Test	Fehling et al. [64]	#4	72.5 (84)	1 - 2.5	4 - 12	1.50%	41 - 98	SF & CF
	Lagier et al. [65]	#8, #11	60	0.9 - 1.2	5 - 18	1% - 4%	19 - 76	CF
	Zhou and Qiao [66]	#5	60 (75)	1.6; 3.2	6 - 14	2%	33 - 97	SF, CF, & BF
	Ronanki et al. [67]	#6, #7	60 (73), 80 (92)	1.6 - 3.5	6 - 10	2%	18 -97	SF & CF
Beam Lap Splice Test	Saleem et al [61]	#7	100	0.6	18	2%	17 - 158	SF
	Ronanki et al. [67]	#4 - #7	60 (73), 80 (92)	1.3 - 3	8	2%	n/a	FSS

Notes: All units in ksi; 1 ksi = 6.9 MPa; *Epoxy coated rebar
SF = Splittling failure; CF = Cone failure; BF = Bar fracture; FSS = Combined flexure, shear, and slip

4.3 Experimental Program

4.3.1 Direct Tension Pullout Test

An unconfined direct tension pullout test setup was utilized to evaluate bond performance of reinforcing steel embedded in UHPC. The test simulated similar low-confinement conditions of the column connection having small concrete cover and no transverse reinforcement. Simplified tension-tension lap splice pullout test setup was designed as shown in Fig. 4.1. Each specimen consists of two anchored bars and a test bar embedded inside a rectangular UHPC block having constant width of 10 in (254 mm). The two anchored bars were

evenly spaced and gripped using two rebar chucks. The test bar was spliced in the center of the anchored bars to ensure symmetric loading and fixed to the moving crosshead. The specimens were tested using the UTM under a constant displacement rate of 0.04 in/min (1 mm/min) until failure occurred. Three LVDTs, mounted on an aluminum ring that was fixed to the test bar 2 in (51 mm) from the UHPC block bottom surface, were used to determine rebar slip.

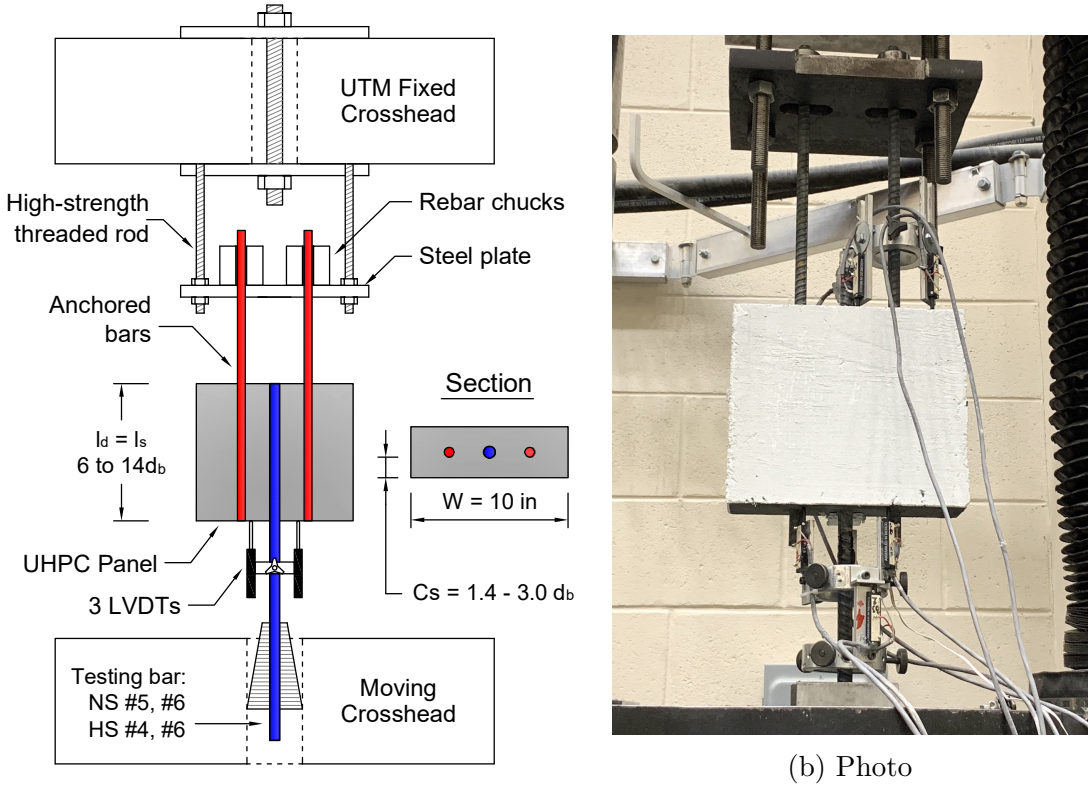

(a) Schematic

(b) Photo

Figure 4.1: Direct tension lap splice test setup

The effects of several parameters on bond strength of reinforcing bar in UHPC were investigated using a total of 21 specimens. Based on the results from column tests in Chapter 3, PCU40 with embedment length (hereinafter, denoted as l_d) of approximately $13d_b$ and

cover (hereinafter, denoted as C_s) of $1.4d_b$ was able to fracture NS #6 rebar. However, PCU25 with similar l_d and C_s of $1.7d_b$ could reach the maximum stress of 78.3 ksi (540 MPa) of NS #6 rebar. Therefore, embedment length of 6, 8, 10, 12, and $14d_b$ and cover ranging from 1.4 to $3d_b$ were studied. Three rebar sizes (#4 (M13), #5 (M16), and #6 (M19)) and two bar types (NS Gr. 60 and HS Gr. 100) were also examined to observe the effects of different bar size and strength. Other variables were held constant: bar spacing of $2.5d_b$, $l_d = l_s$ (where l_s is the splice length), and UHPC width of 10 in. Table 4.2 shows the test matrix of the direct tension pullout specimens.

Table 4.2: Direct tension pullout test matrix

ID	Test bar (US)	Bar Grade (US)	Cover, Cs (db)	Embedment length, ls (db)	Variables
P-d5NS-Cs1.4-ls6	NS #5	60	1.4	6	Splice length
P-d5NS-Cs1.4-ls8	NS #5	60	1.4	8	
P-d5NS-Cs1.4-ls10	NS #5	60	1.4	10	
P-d5NS-Cs1.4-ls12	NS #5	60	1.4	12	
P-d5NS-Cs1.4-ls14	NS #5	60	1.4	14	
P-d5NS-Cs2-ls6	NS #5	60	2	6	Side cover
P-d5NS-Cs2-ls8	NS #5	60	2	8	
P-d5NS-Cs2-ls10	NS #5	60	2	10	
P-d5NS-Cs2-ls12	NS #5	60	2	12	
P-d5NS-Cs3-ls6	NS #5	60	3	6	Side cover
P-d5NS-Cs3-ls8	NS #5	60	3	8	
P-d5NS-Cs3-ls10	NS #5	60	3	10	
P-d6NS-Cs1.6-ls6	NS #6	60	1.67	6	Bar size
P-d6NS-Cs1.6-ls8	NS #6	60	1.67	8	
P-d6NS-Cs1.6-ls10	NS #6	60	1.67	10	
P-d6HS-Cs1.6-ls10	HS #6	100	1.67	10	Bar strength
P-d6HS-Cs1.6-ls12	HS #6	100	1.67	12	
P-d6HS-Cs1.6-ls14	HS #6	100	1.67	14	
P-d4HS-Cs2.5-ls8	HS #4	100	2.5	8	Side cover
P-d4HS-Cs2.5-ls10	HS #4	100	2.5	10	
P-d4HS-Cs2.5-ls12	HS #4	100	2.5	12	

4.3.2 Beam Lap Splice Test

To study bond responses of reinforcing steel in UHPC when subjecting to bending stress, six precast beams using UHPC lap splice connection were tested. Although the design parameters differ, the specimens can be considered as scaled-down versions of the prefabricated deck panels investigated by Graybeal [46] and Haber et al. [63]. The specimen geometry was chosen because (1) lower quantity of UHPC was required, (2) the specimen could simulate both the precast columns using the proposed seismic UHPC connection (despite no shear demand and cyclic loading) and the field cast UHPC connection for prefabricated decks, and (3) localized individual reinforcing bar response can be evaluated.

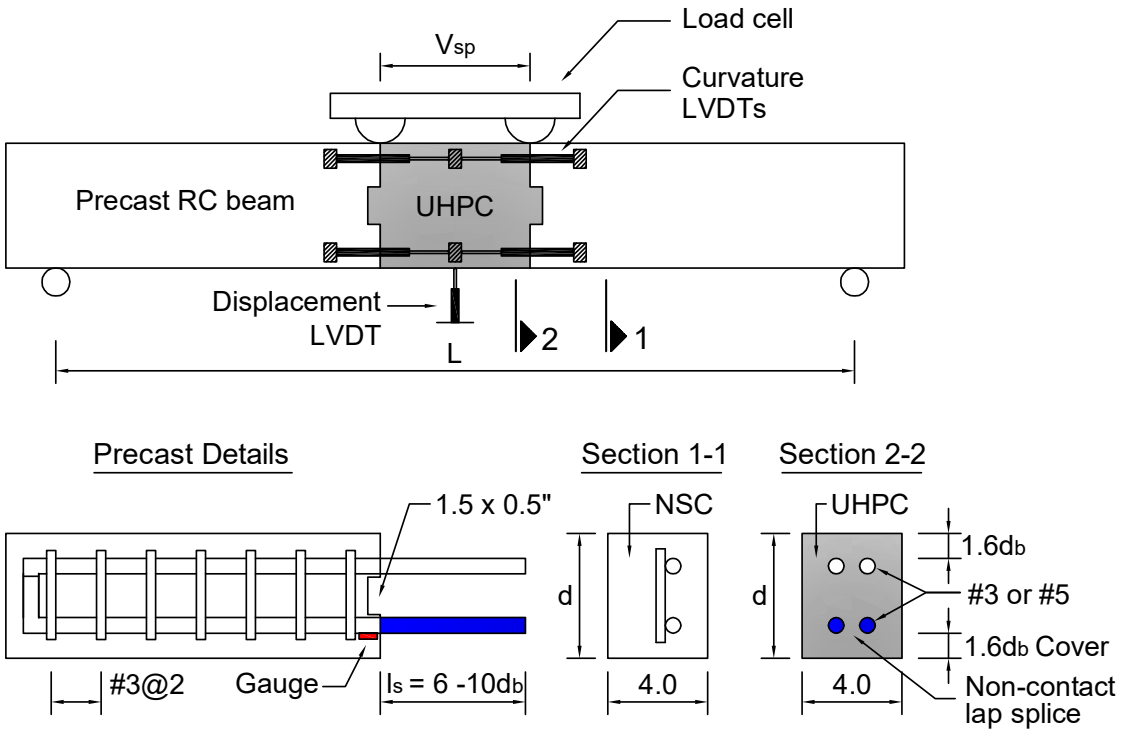

Figure 4.2: Lap splice beam detail and test setup

Fig. 4.2 shows the specimen details, instrumentation, and test setup. Each specimen consisted of two precast RC beams with longitudinal bars protruding l_d long from the left and

right beam surfaces. The protruding bars were spliced l_s long using non-contact lap splice. The specimens were designed using nonlinear moment-curvature ($M - \phi$) analysis. The design assumed failure occurred in the precast RC beams due to yielding of the longitudinal reinforcement. Two different bar sizes and strength (NS #5 (M16) and HS #3 (M10)) and three splice length l_s of 6, 8, and $10d_b$ with constant concrete cover of C_s of $1.66d_b$ were used to investigate the bond performance. The resulting longitudinal reinforcing ratios were 1.55% and 0.69% for specimens reinforced with HS #3 (M10) and NS #5 (M16), respectively. All the precast RC beams were transversely reinforced with one-leg NS #3 (M10) stirrups with the spacing of 2 in (51 mm). The lap splice beams were tested under four-point loading using a UTM at a displacement rate of 0.1 in/min (2.5 mm/min) until failure occurred. One LVDT was used to measure midspan deflection and four LVDTs were installed across the connection interfaces for curvature measurements. In addition, two strain gauges were installed inside the precast elements at the interface to measure strain of the longitudinal reinforcement. Table 4.3 shows the test matrix of the lap splice beam specimens.

Table 4.3: Beam lap splice test matrix

ID	Bar Type/ Size	Longitudinal steel ratio	l_s/l_d (d_b)	Connection length (in)	Vspan (in)	b x d x L (in)
B-d5NS-ls6	NS #5	1.55%	6/7.8	6	6	4 x 5 x 32
B-d5NS-ls8	NS #5	1.55%	8/8.8	6	6	4 x 5 x 32
B-d5NS-ls10	NS #5	1.55%	8.8/9.2	6	6	4 x 5 x 32
B-d3HS-ls6	HS #3	0.69%	6/8	3.75	4	4 x 4 x 26
B-d3HS-ls8	HS #3	0.69%	8/9	3.75	4	4 x 4 x 26
B-d3HS-ls10	HS #3	0.69%	10/10	3.75	4	4 x 4 x 26

Notes: 1 in = 25.4 mm

4.3.3 Casting and Material Properties

Fig. 4.3 shows the casting procedures for direct tension pullout specimens. Lapped reinforcement was arranged using wooden formwork. UHPC was then cast and allowed to cure for 48 hours prior to demolding. Fig. 4.4 shows the construction process of lap splice beam specimens. Initially, NSC was poured over the reinforcement and allowed to cure for 24 hours before demolding. The precast beam surface at the interface was ground to expose aggregate finish. After that the beams with protruding bars were spliced, pre-wetted to obtain a saturated surface dry (SSD) condition and UHPC was poured.

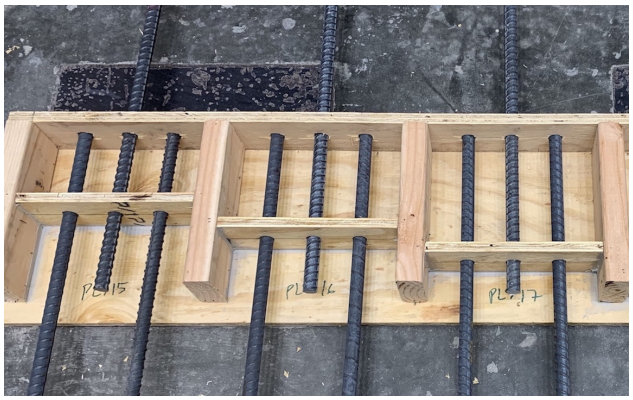

(a) Formwork

(b) Casting UHPC

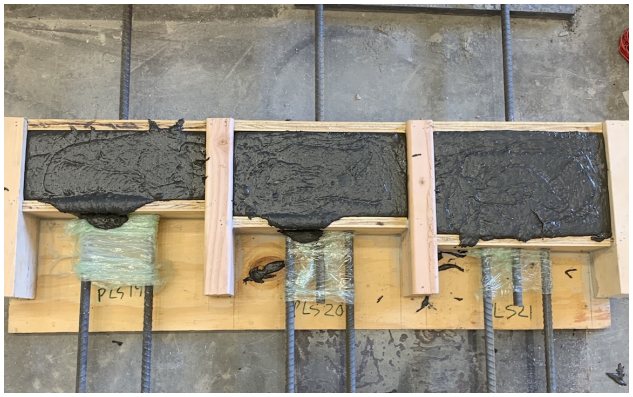

(c) After casting

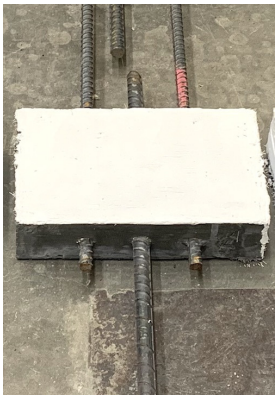

(d) Typical specimen

Figure 4.3: Direct tension lap splice specimen construction

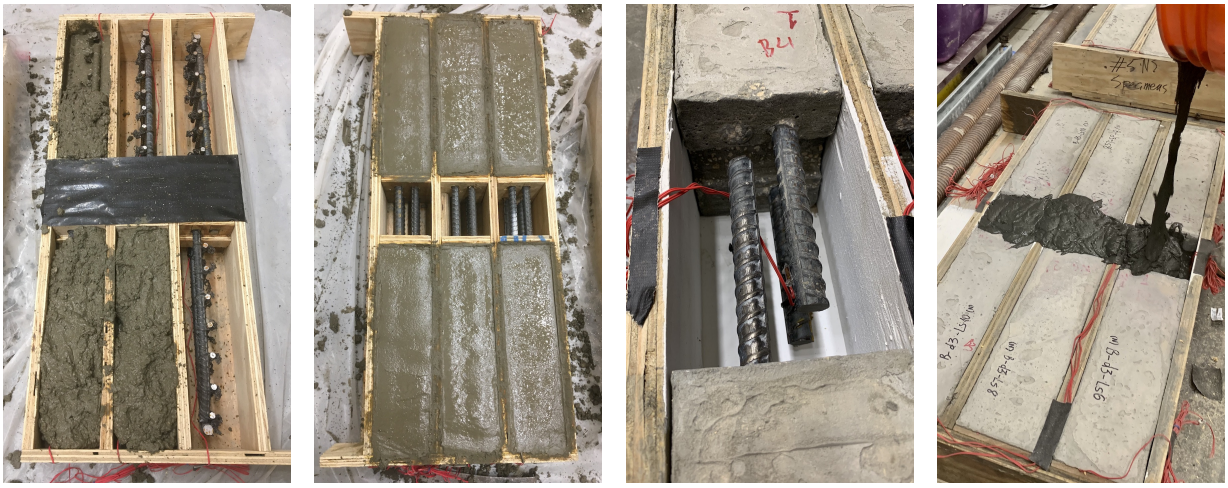

(a) NSC casting (b) After NSC casting (c) Connection detail (d) UHPC casting

Figure 4.4: Lap splice beam casting

Four different materials were utilized to construct both pullout and beam specimens including NSC, UHPC, NS reinforcing steel, and HS reinforcing steel. The precast beams were cast with two different batches of ready-mix conventional concrete having an expected compressive strength of 5 ksi (34.5 MPa). The average test-day f'_c of NSC was determined according to ASTM C39 [54]. UHPC utilized for both types of specimens had the same mix design to the precast column connection (Table 1.1). The average test-day f'_c and elastic modulus of UHPC were determined ASTM C1856/C1856M [55]. Two dog-bone specimens with the dimensions suggested by Zhou and Qiao [40] were used to determine the UHPC tension response. Fig. 4.5 depicts the UHPC tension stress-strain behavior. In tension, UHPC initially exhibited linear elastic response, followed by strain-hardening after the first cracking occurred and a gradual strain-softening after a localized crack was formed. The measured concrete properties are shown in Table 4.4. Both specimen types were reinforced with ASTM A615 Gr. 60 (Grade 420) and ASTM A1035 Gr. 100 (Grade 690) steel. The measured reinforcement properties that include yield strength (f_y), yield strain (ε_y), and

ultimate strength (f_u) are listed in Table 2.5.

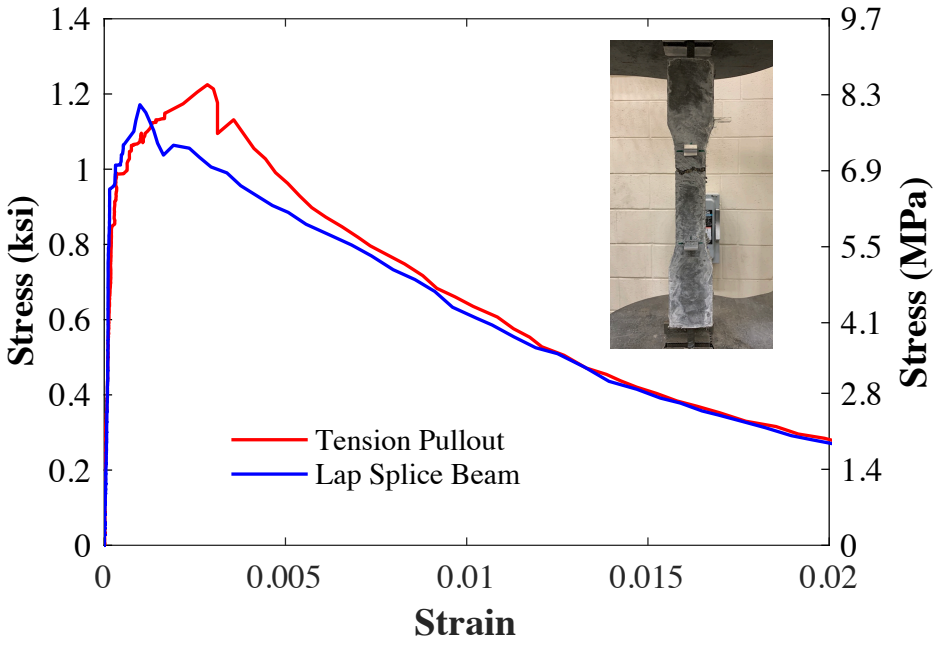

Figure 4.5: UHPC tension stress-strain relationship

Table 4.4: Measured concrete properties for component-level specimens

ID	NSC	UHPC			
	f'_c Test day	f'_c Test day	Young's modulus	f_t First crack	f_t Ultimate
Pullout	-	19.86	5930	0.98	1.24
B-d5NS	6.25	19.77	5738	1.04	1.18
B-d3HS	3.4	19.77	5738	1.04	1.18

f'_c is compressive strength; f_t is tensile strength
Notes: All units in ksi; 1 ksi = 6.9 MPa

4.4 Direct Tension Lap Splice Test Results

4.4.1 Failure Modes

Fig. 4.6 shows the failure modes observed in the pullout tests. The majority of the specimens exhibited splitting cracks at failure under four typical different forms of crack propagation. In general, fine cracks initiated at the bottom of the UHPC block and propagated toward the top surface. Large splitting cracks concentrated along the length of the test bar were observed at failure (Fig. 4.6a) for specimens with short splice length (6 and/or $8d_b$) when the maximum load was reached prior to rebar yielding.

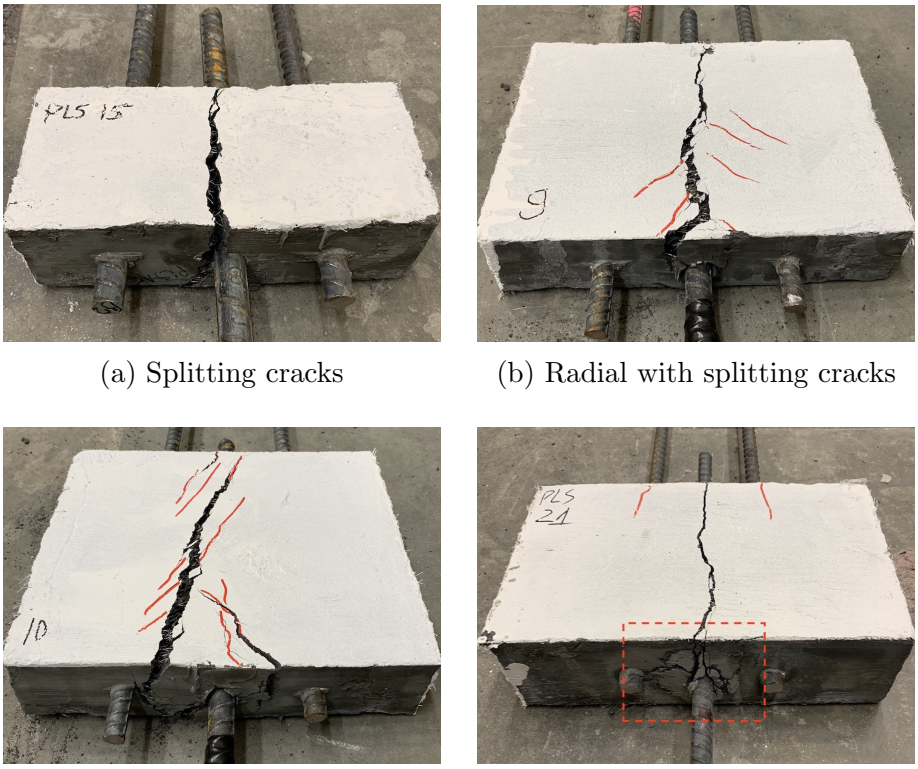

(a) Splitting cracks (b) Radial with splitting cracks

(c) Diagonal with splitting cracks (d) Cone with fine splitting cracks

Figure 4.6: Different failure modes of direct tension lap splice specimens

As the splice length was increased (10 and $12d_b$), UHPC bond strength was able to

develop the reinforcement. The high radial stress generated by the compressive struts from the ribs of the deformed bar created multiple radial cracks on UHPC block as shown in Fig. 4.6b (commonly occurred on specimens with small side covers). The filure mode with combined diagonal and splitting cracks (Fig. 4.6c) occurred on specimens with splice length of $14d_b$ and side covers smaller than $2d_b$. This indicates that the higher tensile stresses that formed the radial cracks exceeded the tensile strength of UHPC, creating localized tensile cracks. For specimens with large side covers (equal and larger than $2.5d_b$) and large embedment length (10 or $12d_b$), the failure mode was shifted to cone-like failure at bottom of UHPC block with fine splitting cracks along the test bar (Fig. 4.6d). This shows that the increase of side cover can reduce splitting crack width and allow the majority of bond stress to develop over a short bond length close to the loaded end of the test bar.

4.4.2 Force-Bar Slip Relationship

The pullout force-bar slip relationships of all specimens are depicted in Fig. 4.7. Specimens having the same bar size, bar type, and side cover, yet different embedment length are presented in the same plot. The left and right vertical axis indicate load and bar stress for each bar group, respectively. It is important to note that the bar slip measurement includes both slip and elongation of the test bar. It can be observed that the initial linear force-slip stiffness prior to bar yielding were similar for all specimens regardless of varying parameters. The increase of embedment length shows consistent increase of bar force, stress, and slip. Large side cover was able to achieve higher bar slip at peak stress and more gradual load drop, resulting in higher energy dissipation (i.e., specimens P-d5NS-Cs3-ls10 and P-d5NS-Cs1.4-ls14 achieved similar bar stresses, but the former exhibited higher slip at peak stress). Energy dissipation refers to the area under the stress/load-slip curve.

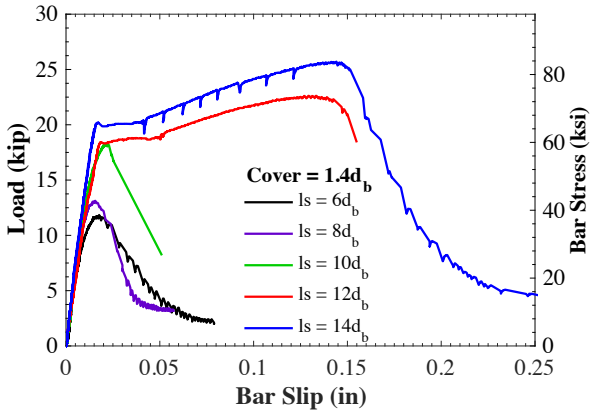

(a) NS #5 - Side cover = $1.4d_b$

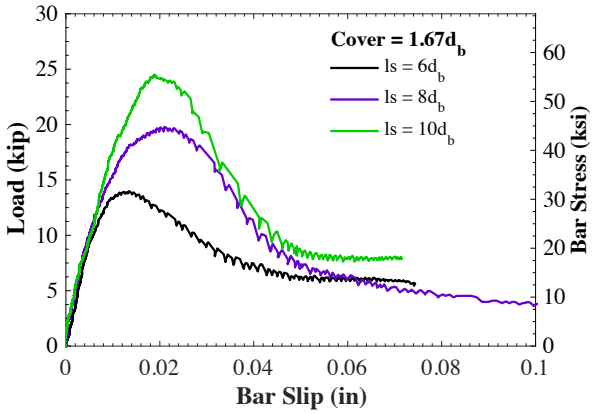

(b) NS #6 - Side cover =$1.66d_b$

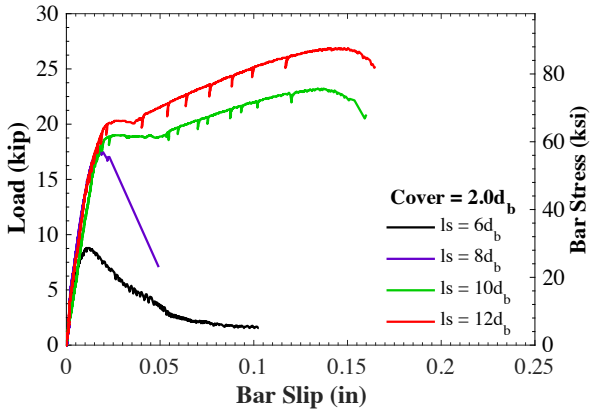

(c) NS #5 - Side cover =$2d_b$

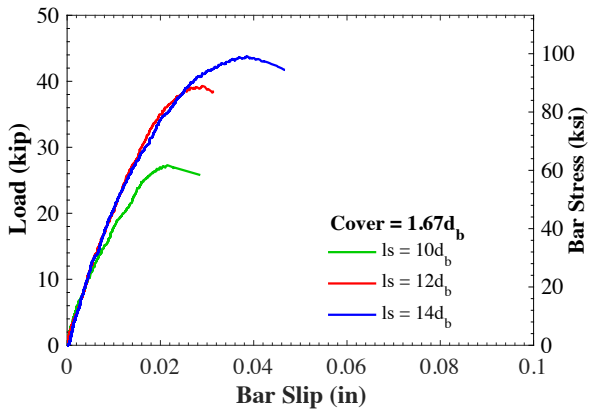

(d) HS #6 - Side cover =$1.66d_b$

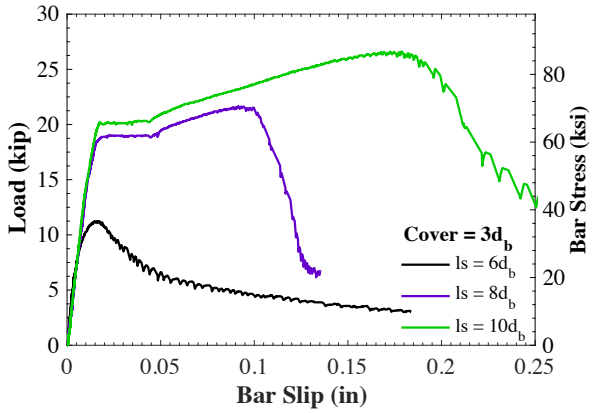

(e) NS #5 - Side cover =$3d_b$

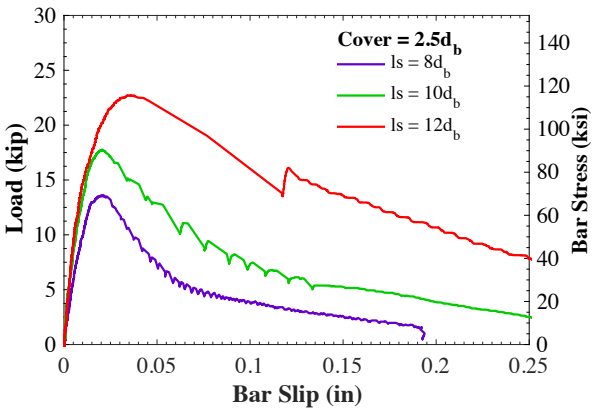

(f) HS #4 - Side cover =$2.5d_b$

Figure 4.7: Force-bar displacement relationship

4.4.3 Rebar Stress under Different Embedment Length

Fig. 4.8 shows the bar stress at failure versus varying embedment length normalized with rebar diameter. The bar stresses were calculated by dividing the peak load with reinforcing steel cross-sectional area. The specimens were divided into five groups that had different side covers, regardless of different bar size and strength. The data trends indicated closely linear relationship between bar stress and embedment length as observed in conventional concrete. Bar stress at bond failure increased with the increase of embedment length and side cover. A red dashed line was plotted to indicate NS bar yield strength in order to identify the embedment length required to develop a Gr. 60 reinforcing steel based on different size covers.

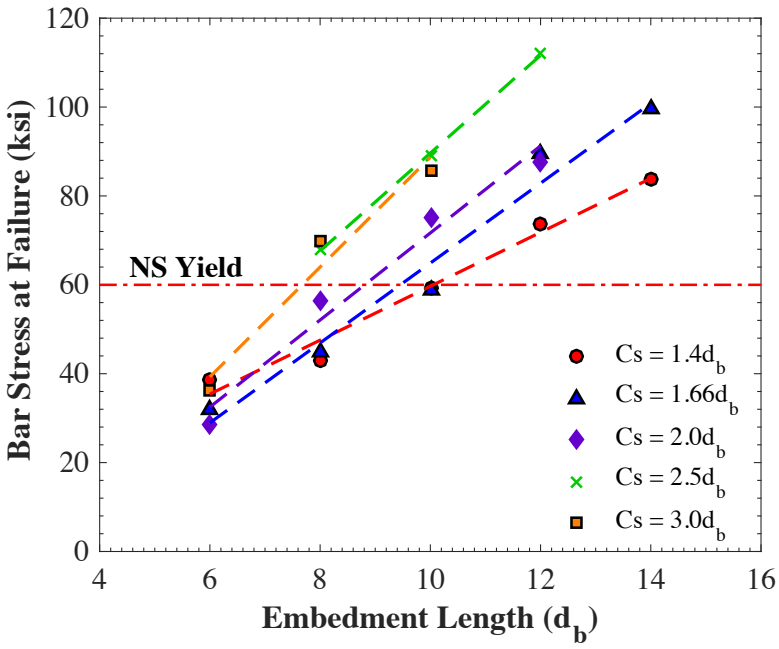

Figure 4.8: Rebar stress at failure with varying side cover

Results indicated that under unconfined conditions, specimens with embedment length of $6d_b$ could reach a maximum bar stress of approximately 40 ksi (276 MPa), which is well

below NS bar yield strength. For embedment length of $8d_b$, a minimum side cover of $2.5d_b$ is required to exceed NS bar yield stress. As the embedment length is increased to $10d_b$, specimens with concrete cover as small as $1.4d_b$ could develop Gr. 60 reinforcing steel. Furthermore, it was observed that bar stresses ranged between 74 ksi (510 MPa) and 101 ksi (696 MPa) at the embedment length of between $12d_b$ and $14d_b$ for side cover between $1.4d_b$ and $1.66d_b$ (corresponds to the precast column design parameters). This stress range was consistent with the maximum stress of 91.3 ksi (630 MPa) and 93.3 ksi (643 MPa) for NS and HS bars respectively observed in column PCU40, and 78.3 ksi (540 MPa) and 84.4 ksi (582 MPa) for NS and HS bars respectively observed in column PCU25.

4.4.4 Bond Strength with Varying Parameters

Fig. 4.9 depicts the effects of side cover, embedment length, bar size, and bar strength on the average bond strength of reinforcing steel embedded in UHPC. The bond strength presented herein is assumed to be uniformly distributed along the embedment length; therefore, can be calculated by dividing the maximum force with the overall contact area between rebar and UHPC: $\mu_{avg} = f_{s,max}d_b/4l_d$. The calculated average bond strength shows consistent results for the majority of data points except specimens with $l_s = 6d_b$, where bond strength fluctuated throughout. Therefore, the effects on rebar-UHPC bond strength exclude $l_s = 6d_b$. It is obvious that bond strength increased with the increase of side cover (Fig. 4.9a). From the total of 21 pullout specimens investigated in this study, average bond strength values range between 1.4 and 2.3 ksi (9.7 and 15.9 MPa) for side cover of 1.4 to $3d_b$. On the other hand, the average bond strength was less sensitive to embedment length having the average of only 7% improvement as l_s was increased from 8 to $14d_b$.

The effect of bar strength was evaluated using specimens having the same side cover of $1.66d_b$. Due to limited test data, a slightly different side cover ($1.4d_b$ vs $1.66d_b$) was used to observe the effect of bar size. The average, minimum, and maximum values of bond

strength presented in Fig. 4.9b were taken from specimens with l_s ranging from 8 to $14d_b$. It was observed that HS Gr. 100 and #5 rebar exhibited approximately 26% and 9% higher average bond strength than NS Gr. 60 and #6 rebar, respectively.

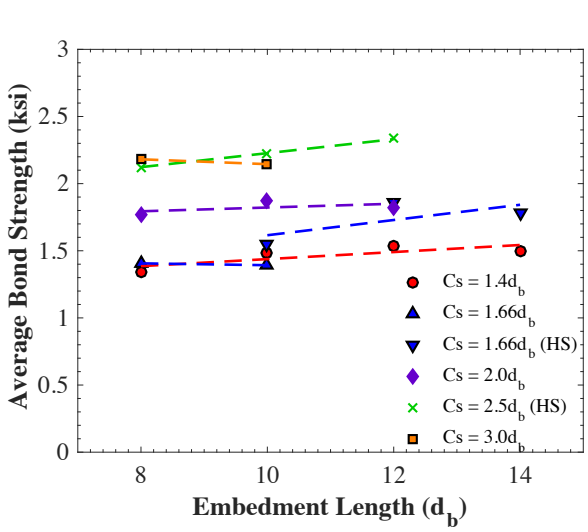

(a) Effect of cover and embedment length

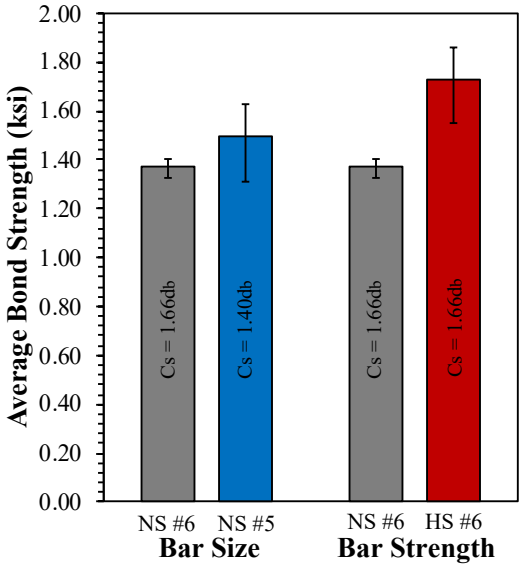

(b) Effect of bar size and strength

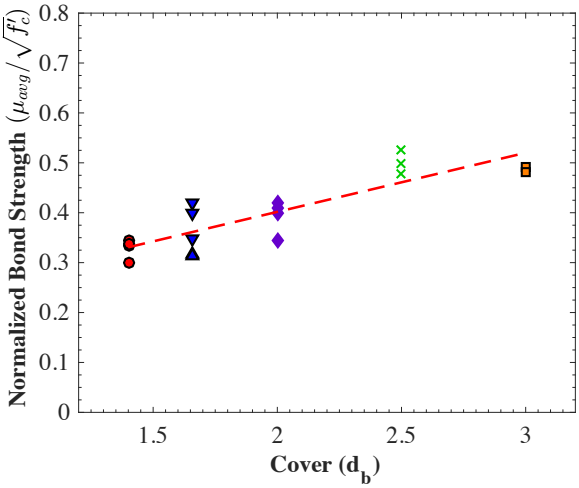

(c) Normalized bond strength

Figure 4.9: Effects of varying parameters on bond strength and normalized bond strength

Previous studies on bond strength of reinforcing steel in conventional concrete showed

bond strength was proportional to the square root of compressive strength. The proportionality was also observed for reinforcing steel embedded in UHPC (Alkaysi and El-Tawil [62], Haber and Graybeal [63], and Ronanki et al. [67]). Fig. 4.9c shows the relationship between average bond strength normalized with square root of UHPC compressive strength and side cover. A clear trend where normalized average bond strength increased with increasing cover was observed. Average bond strength in this study ranges between $0.32\sqrt{f'_c}$ and $0.52\sqrt{f'_c}$, where f'_c is in ksi.

4.5 Lap Splice Beam Test Results

4.5.1 Failure modes

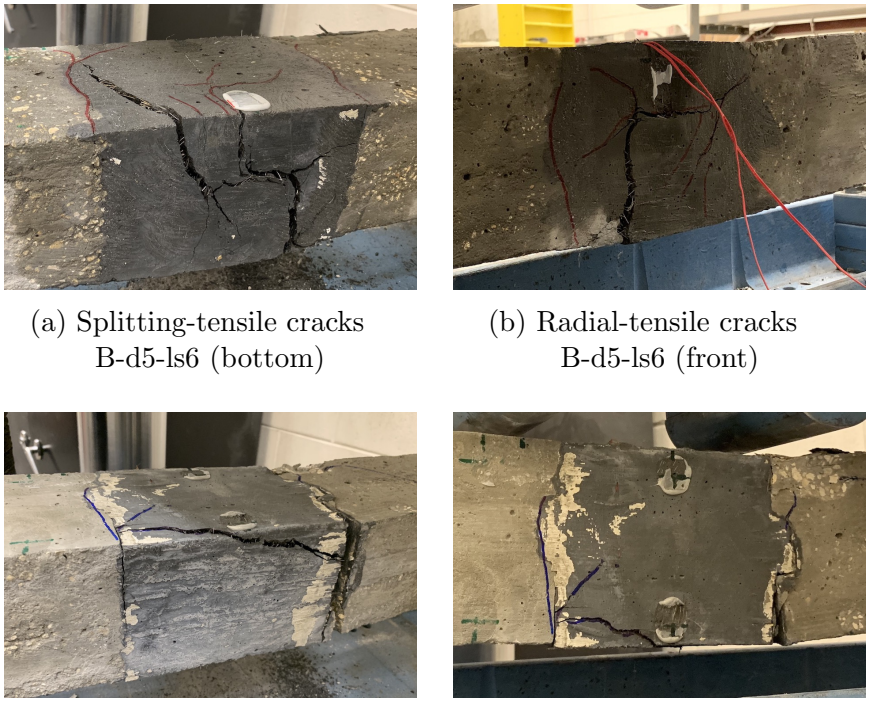

(a) Splitting-tensile cracks B-d5-ls6 (bottom)

(b) Radial-tensile cracks B-d5-ls6 (front)

(c) Interfacial cracks B-d5-ls10 (bottom)

(d) Splitting cracks B-d5-ls10 (front)

Figure 4.10: Typical failure modes of lap splice beams

Fig. 4.10 shows the crack patterns of tested lap splice beams. The crack patterns indicate how stresses were transferred in the lap splice connection under bending stress state. It can be observed that specimens with short spliced length exhibited splitting failure at the bottom surface (Fig. 4.10a). Concurrently, as large tensile stress exceeded UHPC tensile strength, flexural cracks occurred at the bottom surface in the regions without longitudinal reinforcement and propagated upward. Several radial cracks created by compressive struts also presented at approximately mid-height of specimen (Fig. 4.10b). For specimens with splice length of $10d_b$ in which spliced bars were terminated at the connection interfaces (Fig. 4.10c and 4.10d), the flexural cracks were avoided. The increasing bond length could also reduce the radial cracks. A single splitting was seen on the bottom surface of the connection. The slip due to splitting crack caused large crack openings at the connection interfaces.

4.5.2 Force-Displacement and Force-Strain Relationships

Fig. 4.11a and 4.11b depict the force-displacement relationships under increasing splice length of specimens reinforced with NS #5 and HS #3 bars, respectively. The specimens exhibited similar stiffness before slippage occurred. The increase of splice length from 6 to $10d_b$ shows the increase of loading capacity between 23% and 31%. However, load gradually dropped after maximum capacity was reached, suggesting that lap spliced beams with l_s of $10d_b$ and concrete cover of $1.66d_b$ may not be sufficient in providing high displacement ductility. It should be noted that past studies on using UHPC connection with l_d = 9.2 - $11.8d_b$ and $C_s = 1.6d_b$ (Hwang and Park [70]; Haber et al. [63]) for precast decks reported higher displacement ductility. Large connection strips typically exhibit higher confined pressure that increases UHPC bond strength and in turn displacement ductility, but were unable to capture the localized maximum bar stress when a single reinforcing bar was used as in current study.

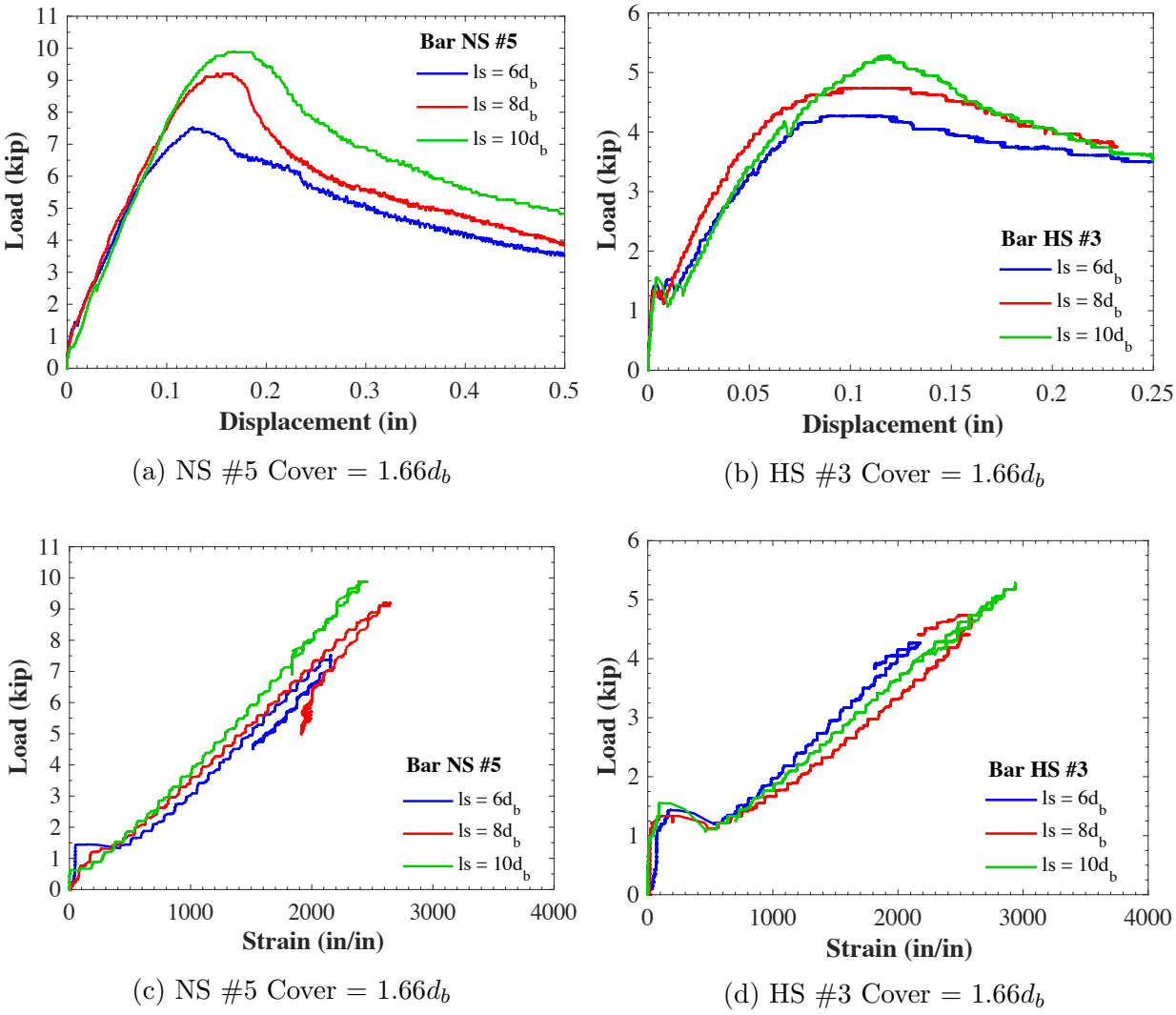

(a) NS #5 Cover = $1.66d_b$

(b) HS #3 Cover = $1.66d_b$

(c) NS #5 Cover = $1.66d_b$

(d) HS #3 Cover = $1.66d_b$

Figure 4.11: Force-displacement and force-strain relationships

Force-strain relationship and strain at peak load for the 6 lap-spliced beams were illustrated in Fig. 4.11c to 4.11d and listed in Table 4.5, respectively. The beam reinforced with NS #5 and l_s of $6d_b$ was unable to develop the reinforcing steel. Beams with NS #5 and l_s of $8d_b$ to $10d_b$ both experienced steel yielding. Bar stresses of the three specimens determined by correlating strain data captured during beam testing with the tension test data range between 62.5 to 62.9 ksi (431 to 434 MPa). For specimens reinforced with HS #3

bars, bar stresses between 63.2 and 85.2 ksi (436 and 587 MPa) were observed. The results indicated the stress level for specimens under bending stress was higher than specimens with the same cover and spliced length under direct tension pullout test. This clearly identifies the effects of different lap spliced specimens under different test setup and stress states.

Table 4.5: Beam lap splice test results

ID	Bar Type/ Size	l_s/l_d (d_b)	Strain at peak stress (in/in)	Peak stress (ksi)
B-d5-ls6	NS #5	6/7.8	0.00215	62.5
B-d5-ls8	NS #5	8/8.8	0.00262	62.9
B-d5-ls10	NS #5	8.8/9.2	0.00243	62.9
B-d3HS-ls6	HS #3	6/8	0.00218	63.2
B-d3HS-ls8	HS #3	8/9	0.00256	74.1
B-d3HS-ls10	HS #3	10/10	0.00294	85.2

Notes: 1 ksi = 6.9 MPa

4.5.3 Moment-Curvature at the Connection Interface

Moment-curvature ($M - \phi$) for each specimen was measured using curvature LVDTs installed across the connection interfaces. The interface location was expected to have the largest curvature, and was demonstrated in the failure mode results. $M - \phi$ experimental results were compared with a reference analytical moment-curvature calculated using non-linear $M - \phi$ analysis at the section over the interface to determine if the lap splice beams were able achieve the maximum moment capacity. The largest experimental curvature of the two interfaces for each specimen was used for comparison as shown in Fig. 4.12. The results showed the specimen reinforced with NS #5 and l_s of $10d_b$ was able to reach the maximum moment capacity despite splitting failure. Yet, the specimen reinforced with HS #3 and

l_s of $10d_b$ exhibited a reduced moment capacity of approximately 21% compared with the calculated bending moment, despite exhibiting higher bar stresses. The results suggest that a splice length of $10d_b$ is sufficient in developing NS Gr. 60 rebar embedded in UHPC with concrete clear cover as low as $1.66d_b$ subjected to bending stress state, but larger embedment length is necessary to obtain higher displacement ductility.

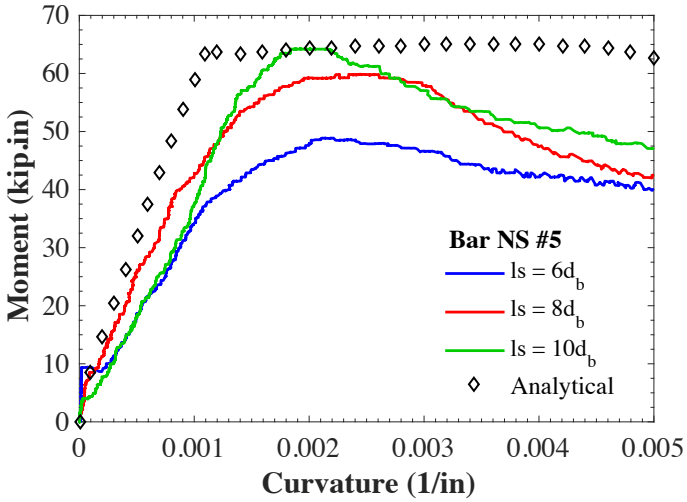

(a) NS #5 Cover = $1.66d_b$

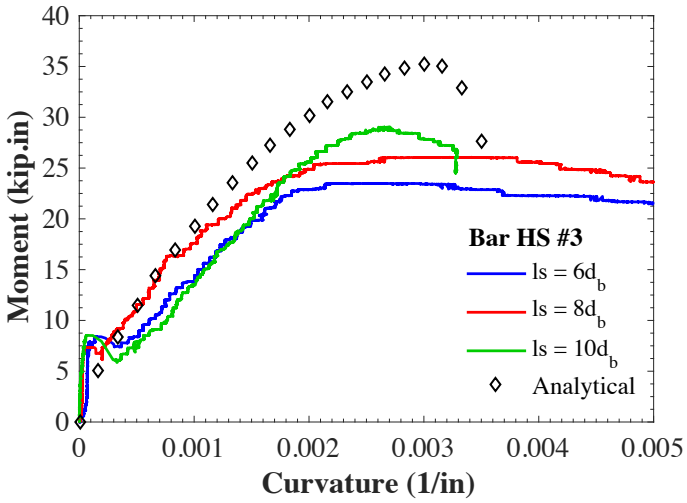

(b) HS #3 Cover = $1.66d_b$

Figure 4.12: Moment-curvature at the connection interface

CHAPTER 5: ANALYTICAL MODELING

5.1 Introduction

This chapter presents the analytical modeling of the tested specimens using two finite element modeling (FEM) programs: the Open System for Earthquake Engineering Simulation (OpenSees) framework and VecTor2 which are both capable of performing nonlinear structural analysis. Direct tension pullout specimens were modeled in OpenSees and calibrated with the experimental force-slip data to determine bond-slip models of NS and HS reinforcing steel embedded in UHPC. Precast and CIP columns were modeled using two methods: OpenSees one-dimensional (1D) fiber section elements and VecTor2 two-dimensional (2D) reinforced continuum plane stress elements. Detailed material constitutive models, element types, and bond-slip modeling are described in the subsequent sections. Results between the two column modeling methods, presented in terms of force-drift hysteresis loops, failure modes, and cumulative energy dissipation, are compared with the experimental results.

5.2 Pullout Modeling

5.2.1 Modeling Method

The pullout specimens were simulated using nonlinear 1D analysis in OpenSees. Each experimental specimen consisted of one test bar and two anchored bars embedded in a UHPC rectangular block. Test results showed dominant splitting failure mode. Minimal slippage was observed in the anchored bars. Therefore, the modeling was simplified to a single test bar modeling which incorporated two different segments: (1) the embedded end and (2) the 2 in free end where LVDTs were mounted to measure bar displacement/slip, as illustrated in Fig. 5.1.

Fifty "Truss" elements were used to model the embedded reinforcing bar and capture stress distribution along bonded length. Only one element was used for the 2 in segment at the free end. Bond-slip springs were utilized to represent bond between reinforcing bar and UHPC. The springs were modeled with "ZeroLength" elements connected between pinned supports and truss nodes. "ReinforcingSteel" and "Steel02" were used to model the materials of NS and HS reinforcing bars, respectively. Values of the different parameters were adopted from the tension bar test based on different rebar size and strength.

The "Hysteretic" material was used to model bond-slip behavior in the spring elements. The material was defined by three positive and three negative force-slip backbone points as depicted in Fig. 5.2. Parameters that control the pinching, damage, and unloading stiffness effects were neglected and set to zero. More material and element details are described in subsequent sections.

Each pullout model was subjected to a monotonically increasing displacement of 0.0005 in (0.013 mm) at the free end bar tip until failure. Initial assumed values of bond stress-slip backbone points were input to begin the analysis. Analytical force-slip results were recorded and compared with the experimental force-slip data. Parameter values of the bond stress-slip models were determined through an iterative optimization procedure using nonlinear least squares. The residual of the analytical and experimental force-slip data sets were minimized in addition to constraint equations that force the two slip parameters to remain in the same order (i.e., δ_2 greater than δ_1) and are both greater than zero. The constraints were enforced by penalty factors. All pullout specimens with embedment length from $8d_b$ to $14d_b$ were simulated ($l_d = 6d_b$ specimens were not analyzed due to the fluctuated test responses).

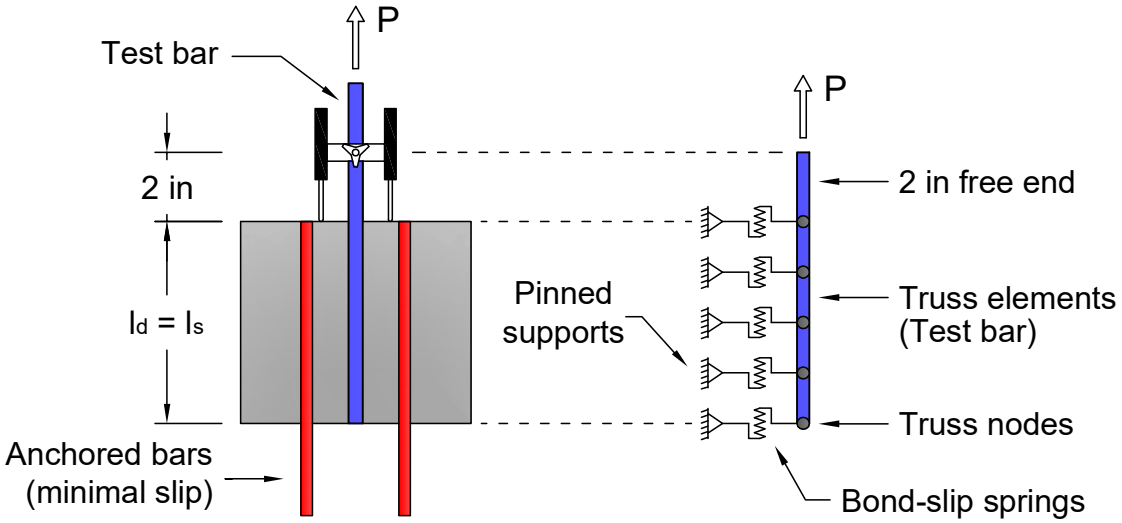

Figure 5.1: Pullout specimen modeling

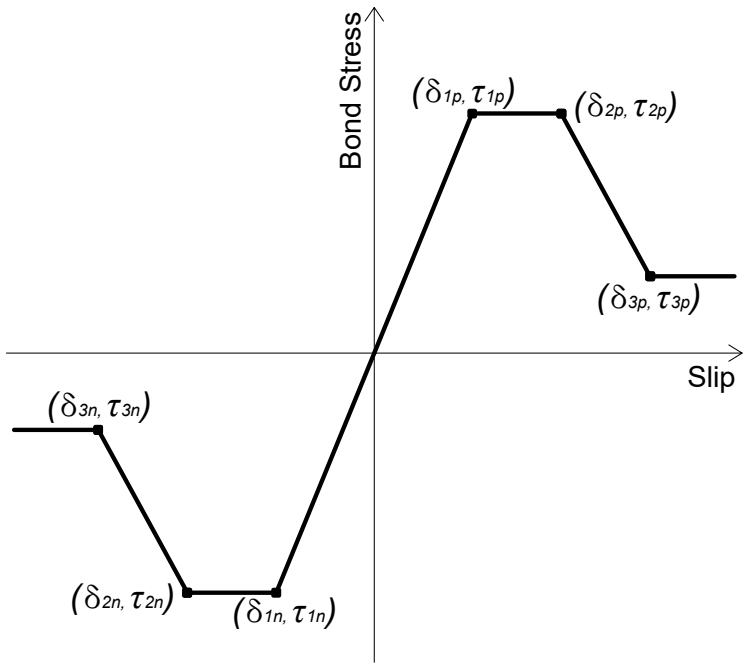

Figure 5.2: Bond-slip model for pullout using hysteretic material

5.2.2 Modeling Results

Figs. 5.3 and 5.4 show the predicted and measured force-bar slip relationships for all direct tension pullout specimens. The modeling method and least-square optimization were able to reproduce the pre-peak and post-peak force-bar slip curves and bar stress levels accurately. The resulting calibrated bond-slip parameters are listed in Table 5.1. It can be observed that the values of peak bond stress $\tau_1 = \tau_2$, residual bond stress τ_3, and the corresponding slips at peak stresses δ_1 and δ_2 were similar in each group of concrete cover. A notable difference was the slip at the onset of residual stress (δ_3) where considerably larger values were seen when reinforcement yielded.

The bond-slip model was taken from the average of specimens with different embedment length but the same concrete cover. The average bond stress-slip models with varying covers are depicted in Fig. 5.5. It can be observed the predicted peak bond stresses increased with increasing concrete covers (with the exception of $1.6d_b$ cover where only few specimens were averaged). The predicted peak bond stresses were between 1.34 and 2.2 ksi (9.2 and 15.2 MPa), and the residual bond stresses after bond failure accounted between 22% and 34% of the peak stress. Consistent increment of bond stress-slip parameters was observed as the cover increased. Consequently, the models were normalized with square root of compressive strength multiplied by cover to bar diameter ratio ($\sqrt{f'_c C_s/d_b}$) where f'_c is in ksi. Fig. 5.6 depicts the proposed unconfined bond stress-slip models for NS and HS reinforcing steel embedded in UHPC.

For NS bar, the peak and residual bond stresses were $\tau_1 = \tau_2 = 0.29\sqrt{f'_c C_s/d_b}$ and $\tau_3 = 0.3\tau_1$, respectively. The slips $\delta_1 = 0.004$ in (0.1 mm), $\delta_2 = 0.024$ in (0.6 mm), and $\delta_3 = 0.087$ in (2.2 mm) were the corresponding slips to the bond stresses. Similar bond-slip parameters were noted in HS bar compared with NS bar. The values of HS bar bond stress parameters were $\tau_1 = \tau_2 = 0.32\sqrt{f'_c C_s/d_b}$, and $\tau_3 = 0.3\tau_1$. The bar slip parameter values were $\delta_1 = 0.04$

in (0.1 mm), $\delta_2 = 0.014$ in (0.35 mm), and $\delta_3 = 0.1$ in (2.5 mm). The proposed models were compared with the unconfined model for NS bar in conventional concrete by Eligehausen et al. [71], assuming the conventional concrete had the same compressive strength value as UHPC. The initial ascending branch and peak bond stress were approximately the same to the proposed models. However, the Eligehausen model exhibited considerably larger δ_2 and δ_3 that can be attributed to traditional test setup where the concrete block was in compression causing significantly improved fracture energy.

Table 5.1: Pullout bond-slip modeling results

ID	$\tau_1 = \tau_2$ (ksi)	τ_3 (ksi)	δ_1 (in)	δ_2 (in)	δ_3 (in)
P-d5NS-Cs1.4-ls8	1.28	0.35	0.0032	0.0124	0.0365
P-d5NS-Cs1.4-ls10	1.5	-	0.005	0.012	0.03
P-d5NS-Cs1.4-ls12	1.52	-	0.0063	0.0533	0.126
P-d5NS-Cs1.4-ls14	1.52	0.315	0.0019	0.0208	0.1
Average	**1.46**	**0.33**	**0.0041**	**0.0246**	**0.0731**
P-d5NS-Cs2-ls8	1.78	-	0.003	0.009	0.05
P-d5NS-Cs2-ls10	1.9	-	0.008	0.04	0.11
P-d5NS-Cs2-ls12	1.85	-	0.007	0.02	0.11
Average	**1.84**	**-**	**0.006**	**0.023**	**0.090**
P-d5NS-Cs3-ls8	2.2	0.69	0.0048	0.0317	0.0671
P-d5NS-Cs3-ls10	2.18	0.81	0.0038	0.0295	0.149
Average	**2.19**	**0.75**	**0.0043**	**0.0306**	**0.108**
P-d6NS-Cs1.6-ls8	1.34	0.35	0.0037	0.0171	0.052
P-d6NS-Cs1.6-ls10	1.33	0.46	0.0028	0.0127	0.0437
P-d6HS-Cs1.6-ls10	1.55	-	0.006	-	-
P-d6HS-Cs1.6-ls12	1.85	-	0.005	0.012	0.08
P-d6HS-Cs1.6-ls14	1.8	-	0.005	0.02	0.09
Average	**1.57**	**0.47**	**0.0045**	**0.0154**	**0.0664**
P-d4HS-Cs2.5-ls8	2.04	0.56	0.0031	0.0125	0.0734
P-d4HS-Cs2.5-ls10	2.2	0.693	0.0007	0.0062	0.1033
P-d4HS-Cs2.5-ls12	2.34	0.72	0.0024	0.0137	0.2125
Average	**2.19**	**0.66**	**0.002**	**0.011**	**0.130**

Notes: τ_1 and τ_2 are peak bond stresses, τ_3 is residual bond stress
δ_1, δ_2, and δ_3 are the corresponding slips.

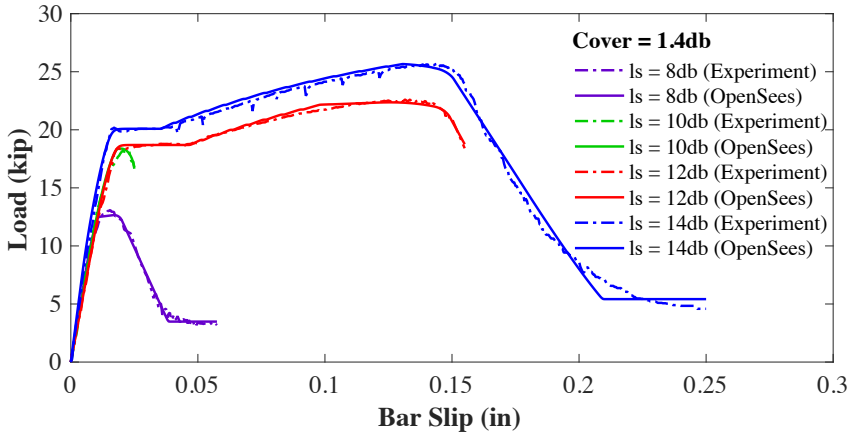

(a) NS #5, Cover = $1.4d_b$

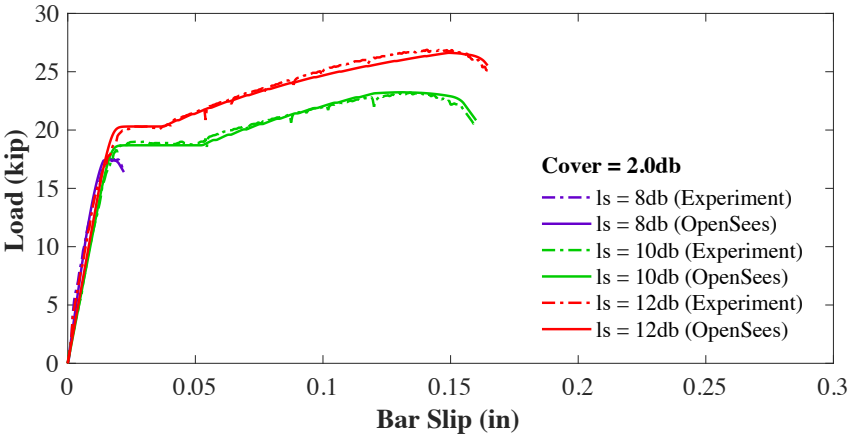

(b) NS #5, Cover = $2d_b$

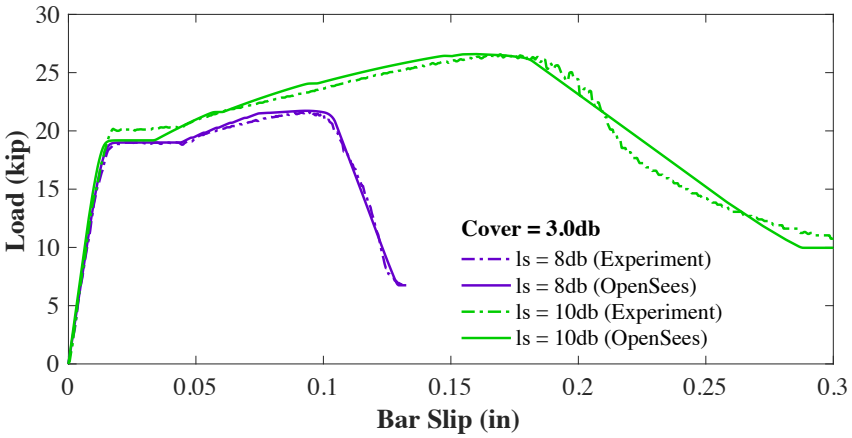

(c) NS #5, Cover = $3d_b$

Figure 5.3: Predicted and measured force-bar slip for covers of 1.4, 2, and $3d_b$

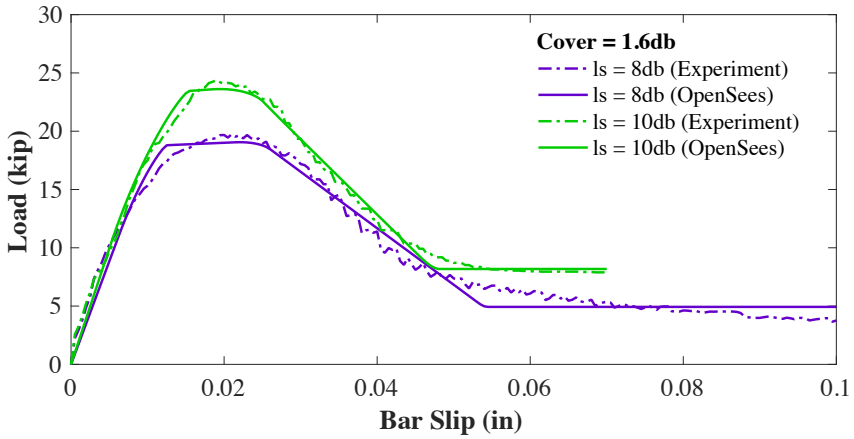

(a) NS #6, Cover = $1.6d_b$

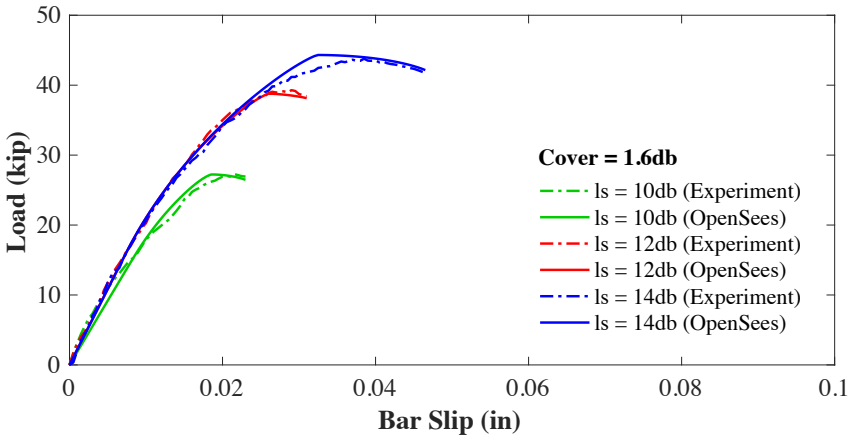

(b) HS #6, Cover = $1.6d_b$

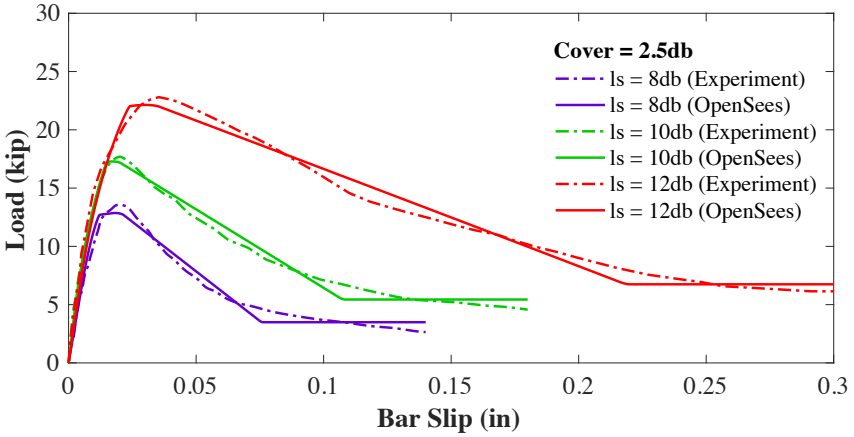

(c) HS #4, Cover = $2.5d_b$

Figure 5.4: Predicted and measured force-bar slip for covers of 1.6 and $2.5d_b$

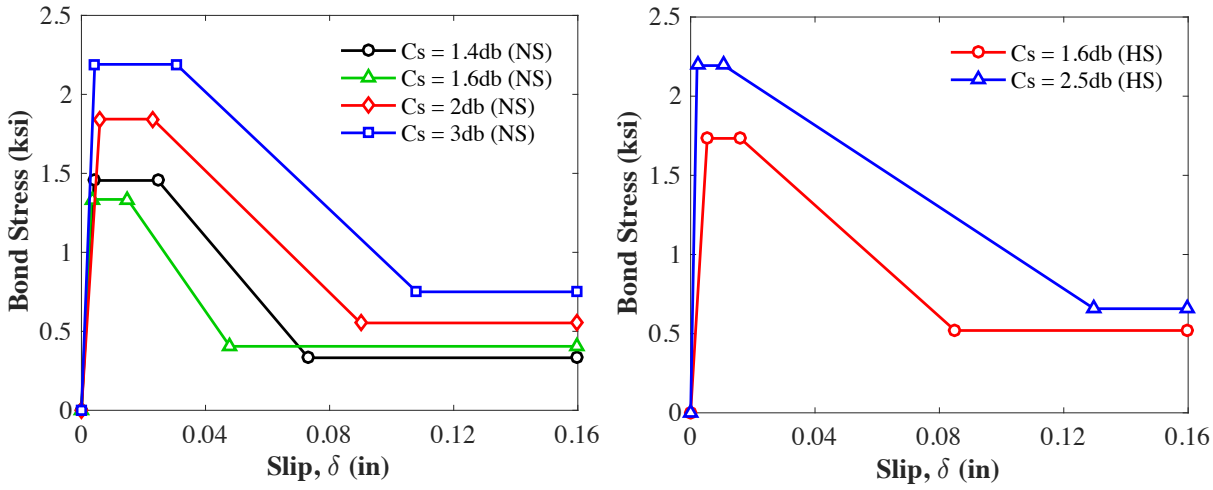

(a) NS bars

(b) HS bars

Figure 5.5: Average bond stress-slip for NS and HS bars with varying covers

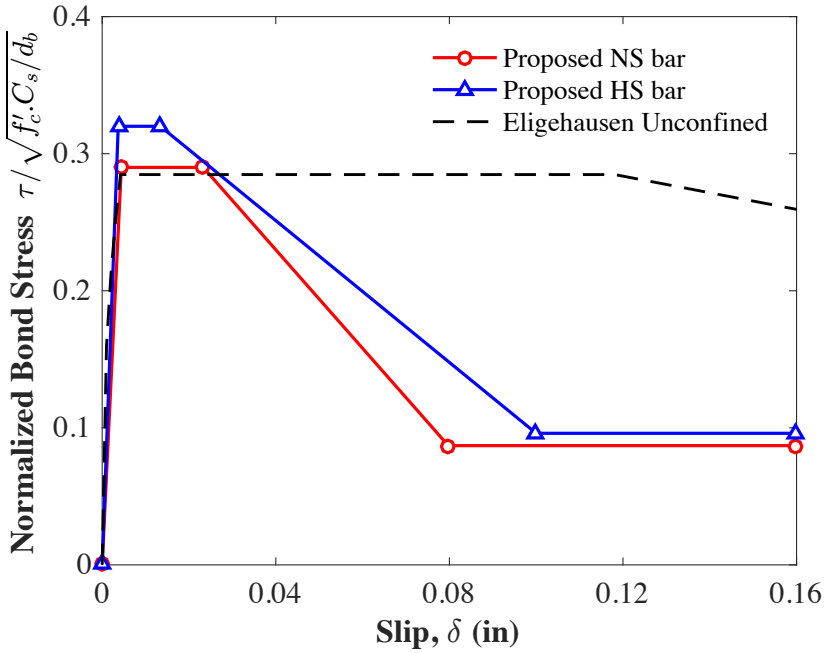

Figure 5.6: Proposed unconfined bond-slip models of reinforcing steel in UHPC

5.3 One-Dimensional (1D) Modeling for Columns

5.3.1 General Concepts

The columns were modeled using one-dimensional beam-column elements with two nodes and fiber sections at the discrete integration points along the length. The model was two-dimensional with 3 degrees of freedom per node. Due to the Euler-Bernoulli assumptions of the flexural elements, slip of reinforcement and in the lapped connection were considered at discrete location using springs.

5.3.2 Materials

5.3.2.1 Concrete

Two types of concrete were used to define concrete materials used for cast-in-place and precast columns. Unconfined concrete was used to represent concrete cover of the column shaft and UHPC connection, in which there is no presence of transverse reinforcement. The concrete cover was measured from the far face of the spiral to the concrete outer surface. Unconfined concrete was modeled using "Concrete01" material in OpenSees. The material is formed by a uniaxial Kent-Scott-Park concrete material [50] with degraded linear unloading/reloading stiffness based on the work of Karsan and Jirsa [72] and with no tensile strength. The constitutive model of "Concrete01" is illustrated in Fig. 5.7 and defined by four input parameters: the peak compressive stress f'_c, strain at peak stress ε_{c0}, concrete crushing stress f'_{cu}, and strain at failure ε_{cu}.

For concrete cover, f'_c was determined from the average test-day NSC compressive strength. The values of $\varepsilon_{c0} = 2f'_c/E_c$ and $\varepsilon_{cu} = 2\varepsilon_{c0} + 0.002$ were determined consistently with the Kent-Scott-Park model, where $E_c = 57000\sqrt{f'_c}$ (f'_c is in ksi). The crushing stress $f'_{cu} = 0$ was used to indicate the completely reduced compressive strength when cover has

spalled off. For UHPC connection, f'_c was determined from the average test-day UHPC compressive strength, ε_{c0} was taken equal to 0.004. UHPC Crushing stress f'_{cu} was set to zero at ε_{cu} of 0.008. The high tensile strength of UHPC was also modeled with "Concrete01" with the input parameters f_t and $\varepsilon_t = f_t/E_c$ taken from the UHPC dog-bone test, while f_{tu} is conservatively set to 0 at $\varepsilon_{tu} = 0.02$. The compression and tension materials were combined using the "Parallel" material in OpenSees.

Confined concrete was used to represent concrete core confined by transverse reinforcement. Confined concrete was also modeled using "Concrete01". However, the four input parameters of the constitutive model were determined using Mander's model [51] for confined concrete. The model uses the material properties at peak stress of unconfined concrete (f'_c and ε_{c0}), section geometry, and material properties, spacing, and geometry of the transverse steel to determine the confined constitutive responses (f'_{cc}, ε_{cc}, f'_{cu}, and ε_{cu}). The calculation of confined concrete parameters was based directly on Mander's equations [51]. Concrete tensile response was also included in this model using "Concrete01" with the input parameters as follows: $f_t = 7.5\sqrt{f'_{cc}}$, $\varepsilon_t = f_t/E_c$, $f_{tu} = 0$, and $\varepsilon_{tu} = 10\varepsilon_t$. The tensile response of NSC was added to obtain accurate initial stiffness prior to concrete cracking occurred.

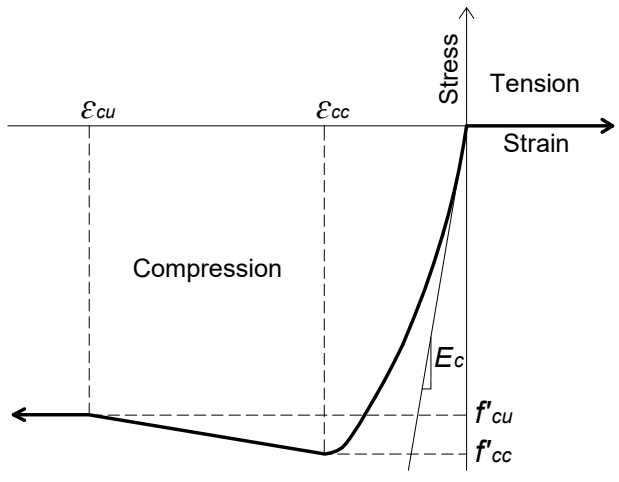

Figure 5.7: Concrete01 material constitutive model

5.3.2.2 Reinforcing Steel

NS longitudinal reinforcement of the column shaft and HS footing dowel were both modeled using the "Steel02" material in OpenSees. The material backbone follows uniaxial Giuffre-Menegotto-Pinto steel material with isotropic strain hardening [73] as depicted in Fig. 5.8. The material requires six input parameters (F_y, E_s, b, $R0$, $CR1$, and $CR2$). Parameters that define the isotropic hardening were neglected.

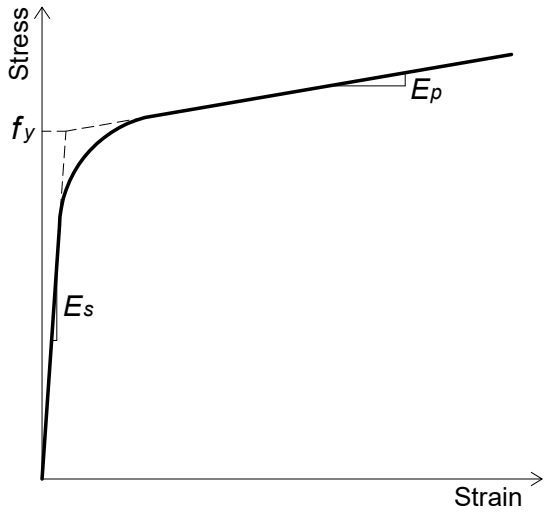

Figure 5.8: Steel02 material constitutive model

Yield strength F_y was taken from the coupon test data. Tangent stiffness E_s was set constant and equal to 29,000 ksi. For NS bars, strain hardening ratio b was determined from the ratio between post-yield tangent and initial elastic tangent. Parameters that control the transition from elastic to plastic branches $R0$, $CR1$, and $CR2$ were set to 18, 0.925, and 0.15, respectively. For HS bars, b, $R0$, $CR1$, and $CR2$ were calibrated based on the coupon test result of HS steel and were found to be 0.001, 2.5, 0.925, and 15, respectively.

To identify the failure point (i.e, rebar fracture), low-cycle fatigue model using available "Fatigue" material in OpenSees was utilized. The material uses a modified rainflow cycle counting algorithm to accumulate damage in a material using Miners Rule. The material

was wrapped around "Steel02" material, but did not influence reinforcing steel stress-strain relationship. As the damage reaches 1.0, "Steel02" stress is dropped to zero.

5.3.3 Elements

5.3.3.1 Force-Based Beam-Column

The force-based beam-column element was utilized to model the column shaft and UHPC connection. The element takes into account the distributed plasticity at the integration points along element length and satisfies equilibrium at both the section and element levels directly based on the iterative force-based formulation. Force-based elements are more computationally expensive than displacement-based elements that only require equilibrium at the element level. However, fewer elements are required for force-based element and higher accuracy is ensured. Fiber sections are used to define the element cross section, where the concrete is discretized, and number and locations of reinforcement are specified. Detailed cross section discretization and number of integration points were specified in the modeling method.

5.3.3.2 Rotational Spring

A rotational spring element was used in this study to model bond-slip rotations caused by the inelastic strain penetration of longitudinal bars into concrete. The spring was defined by the "ZeroLength" element in OpenSees where the translational degrees of freedom were constrained and only the rotational degree of freedom was allowed. The rotational spring material was defined by the "Hysteretic" constitutive model (Fig. 5.9) that requires input of moment-rotation relationships and power β used to determine the degraded unloading stiffness based on ductility. Factors that determine the pinching effects and damage due to ductility and energy were not considered. Bond-slip modeling details in this study were

discussed in the following section along with existing modelings in the literature.

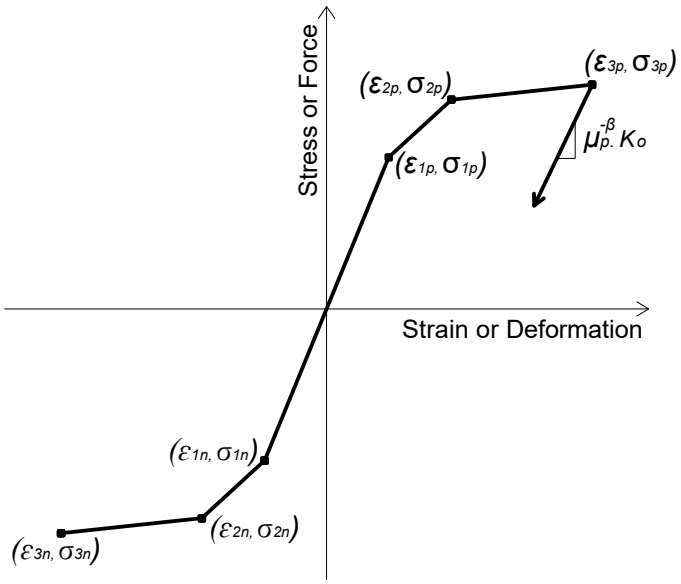

Figure 5.9: Hysteretic material for bond-slip model

5.3.4 Bond-Slip Modeling

Observation from the experimental results indicated the precast columns exhibited similar load transfer mechanism to a typical CIP bridge column, with the exception of the transfer location. Lateral load applied at column tip was initially transferred from NS bars through UHPC bond strength, which in turn ensured the force transfer to the HS footing dowels. For the CIP column, bar tensile stress was transferred directly into the footing through bond between reinforcing bar and footing concrete. When bond strength between reinforcing bar and UHPC or concrete is exceeded, strain penetration (slip) occurs. Bond-slip plays a key role in controlling the column lateral capacity and displacement ductility, particularly in the currently studied precast columns, in which a short splice length was utilized with no shear reinforcement in the connection region. This sections briefly reviews

the existing bond-slip modeling techniques used for numerical simulation of seismic bridge columns.

To include strain penetration effect from longitudinal reinforcement into the footing for CIP columns, Zhao and Sritharan [74] developed a stress-slip constitutive model for reinforcing steel to be used with a "ZeroLength" element in nonlinear fiber-section analysis at the member ends. Good correlation between the predicted and measured local and global responses in the column and joint tests were obtained. However, the proposed model was limited to displacement-based beam-column elements in OpenSees and was only calibrated with the experimental specimens having fully anchored steel reinforcement that exhibited slip along a portion of the anchorage length.

Tazarv [15] proposed the use of a modified stress-strain relationship for reinforcing steel directly without using additional "ZeroLength" element. Bond-slip effect is implicitly included in the modified bar material, typically resulted in softened reinforcing steel constitutive model. The modified material is applied to a specified integration point of either force-based or displacement-based beam-column elements, where slippage occurs. Tazarv [15] used the proposed model to simulate a conventional CIP column, and columns with UHPC-filled duct connection that used NS and shape memory alloy (SMA), showing good agreement between the predicted and experimental results. The proposed model is valid for fully anchored bars with no bond failure.

Al-Jelawy [75] proposed a 3D discrete fiber-based nonlinear analysis to model CIP and GS columns using OpenSees. The 3D model used a central nonlinear beam-column elements with fiber-section to represent cover and core concrete. Discrete reinforcing bars were modeled with truss elements connected to the central beam-column element using rigid elastic beam elements. At the locations where slip existed, bond-slip springs modeled with "ZeroLength" elements were used to connect between truss and rigid beam elements. The modeling method offers realistic physical representation with the use of uniaxial bond

stress-slip calibrated from pullout and tension GS tests. Test results showed similar global hysteretic force-drift response compared with the conventional 1D fiber-section. Yet, the initial, unloading and reloading stiffness were better captured by the 3D modeling. However, the 3D modeling is susceptible to spring stiffness issues that requires careful controlling steps of constant axial load.

The bond-slip modeling in this study utilizes the method proposed by Wehbe [76]. Schematic of the bond-slip calculation procedure is depicted in Fig. 5.10. To account for bond-slip of embedded bar in the footing of CIP columns, Wehbe [76] assumes that the bond-slip rotation occurs about the neutral axis of the column-footing interface cross section, and that the bond stress over the development length is uniform, resulting in a linear or bilinear distribution of bar strain depending on the extreme reinforcing steel stress-strain levels. The reinforcing steel stresses and neutral axis c can be determined using nonlinear moment-curvature analysis.

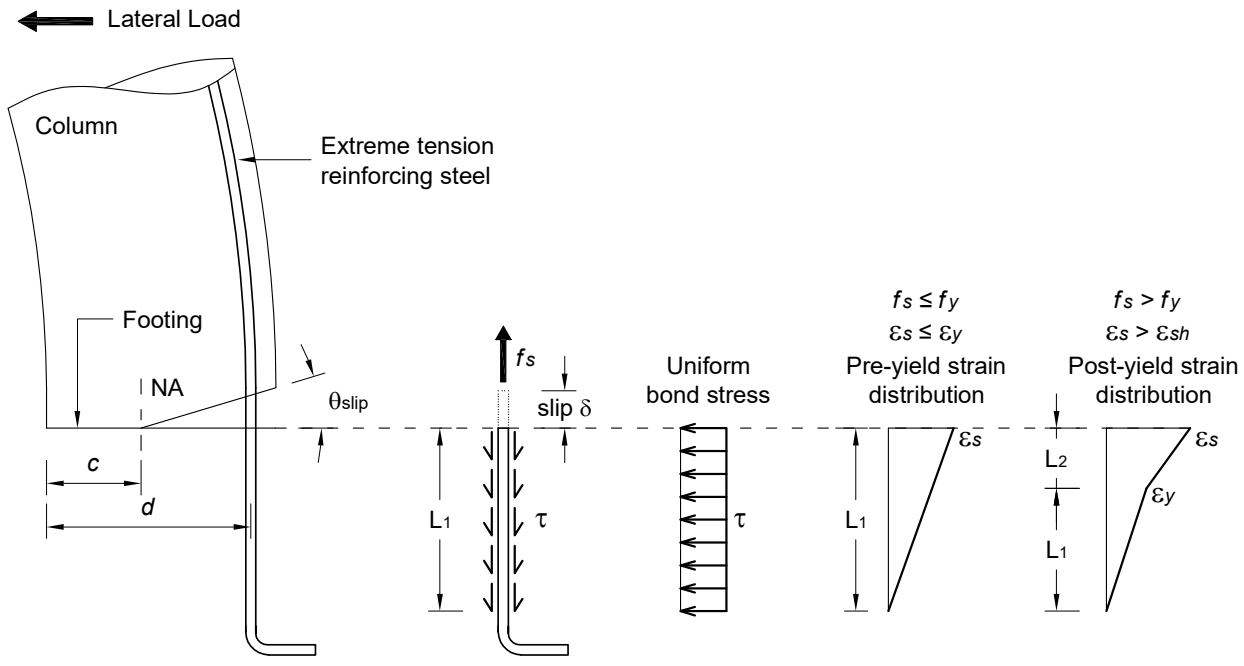

Figure 5.10: Wehbe's method for bond slip rotation of embedded steel

Subsequently, the slip in the extreme tension bar is determined by integrating the strain profile along the embedded bar length inside the footing (Eq. 5.1). With linear strain distribution up to yielding and bilinear strain after yielding occurs, Eq. 5.1 can be simplified to Eq. 5.2.

$$\delta_{slip} = \int_0^{l_d} \varepsilon(x) dx \tag{5.1}$$

$$\delta_{slip} = \begin{cases} \dfrac{\varepsilon_s l_1}{2} & \text{if } \varepsilon_s \leq \varepsilon_y \\ \dfrac{\varepsilon_s l_1}{2} + \dfrac{(\varepsilon_s + \varepsilon_y) l_2}{2} & \text{if } \varepsilon_s > \varepsilon_y \end{cases} \tag{5.2}$$

where the lengths l_1 and l_2 are calculated using Eq. 5.3 and Eq. 5.4, respectively, and u is the peak bond stress of reinforcing steel in concrete materials. With the known slip, the resulting rotation at the base of the column is calculated using Eq. 5.5 for each corresponding moment from $M - \phi$ analysis.

$$l_1 = \frac{f_s d_b}{4u} \tag{5.3}$$

$$l_2 = \frac{(f_s - f_y) d_b}{4u} \tag{5.4}$$

$$\theta_{slip} = \tan^{-1}\left(\frac{\delta_{slip}}{c - d}\right) \tag{5.5}$$

The obtained moment-rotation ($M - \theta$) envelope was idealized to a bilinear $M - \theta$ curve formed by the effective yield $M_{y,eff} - \theta_{y,eff}$ and $M_u - \theta_u$ at the onset of core concrete crushing. The bilinear $M - \theta$ curve was calculated such that the areas under the bilinear curve and the envelop after the first yield point (moment at the onset of rebar yielding) are equivalent. Lastly, a rotational spring element with "Hysteretic" material properties ($M_{y,eff} - \theta_{y,eff}$) and ($M_u - \theta_u$) was used to model the bond-slip rotation.

5.3.5 Column Modeling Method

5.3.5.1 CIP Columns

The two CIP columns [48] were modeled using one-dimensional fiber-section nonlinear analysis using OpenSees. Fig. 5.11 shows the schematic of the 1D modeling for CIP40, but also applicable to CIP25 by changing the column length. The column shaft was modeled with two force-based beam-column elements. The first element has the same length as the connection and has three integration points. The second element has seven integration points. Typically, one force beam-column element with five integration points is sufficient for CIP column shaft modeling, but two elements were utilized to be consistent with precast column modeling for comparison purposes. A single fiber-section was used for both elements. The section incorporates an unconfined concrete cover discretized into 4 circumferential and 24 radial fibers, a confined concrete core discretized into 16 circumferential and 24 radial fibers, and 10 reinforcing bars. A rotational spring was used to model the bond-slip rotation at the footing-column interface. The spring was created with a "ZeroLength" element connected with a fixed node and a node of the force beam-column element.

Material parameters for the unconfined and confined concrete modeled with "Concrete01", and for longitudinal reinforcing bars modeled with "Steel02" are shown in Table 5.2. The moment-rotation determined from $M - \phi$ analysis and Wehbe's method, and modeled with "Hysteretic" material is shown in Table 5.3. Axial load of 126 kips (560 kN) was applied to the top node. Gravity analysis was initially conducted to simulate the prestressed axial force. Lateral displacement was then applied based on the drift levels until failure occurred. Failure in this 1D analysis was enforced by limiting the damage level of low-cycle fatigue material to 1.0.

Table 5.2: Concrete and steel material parameters for CIP columns

Material Description	Parameters	CIP40	CIP25
Unconfined concrete (Concrete01)	f'_c (ksi)	7.4	7.6
	f'_{cu} (ksi)	0	0
	ε_{co} (in/in)	0.003	0.003
	ε_{cu} (in/in)	0.008	0.008
Confined concrete (Concrete01)	f'_c (ksi)	7.4	7.6
	f'_{cc} (ksi)	9.38	9.01
	f'_{cu} (ksi)	8.62	8.57
	ε_{cc} (in/in)	0.0071	0.0059
	ε_{cu} (in/in)	0.0147	0.0097
NS longitudinal bar (Steel02)	f_y (ksi)	68.6	65.3
	E_s (ksi)	29000	29000
	b	0.0106	0.0079
	$R0$	18	18
	$CR1$	0.925	0.925
	$CR2$	0.15	0.15

Table 5.3: Moment-rotation material parameters for CIP columns

Material Description	OpenSees Material	Parameters	CIP40	CIP25
Moment-rotation at the footing	Hysteretic (Multi-linear backbone)	M_1 (kip-in)	0	0
		M_2 (kip-in)	3654	2830
		M_3 (kip-in)	4140	3072
		θ_1	0	0
		θ_2	0.0022	0.0013
		θ_3	0.0432	0.0229
		B	0.5	0.5

Notes: Moment-rotation is formed by three positive and three negative backbone points
M_2 and θ_2 are the effective yield moment and rotation
M_3 and θ_3 are the plastic moment and rotation

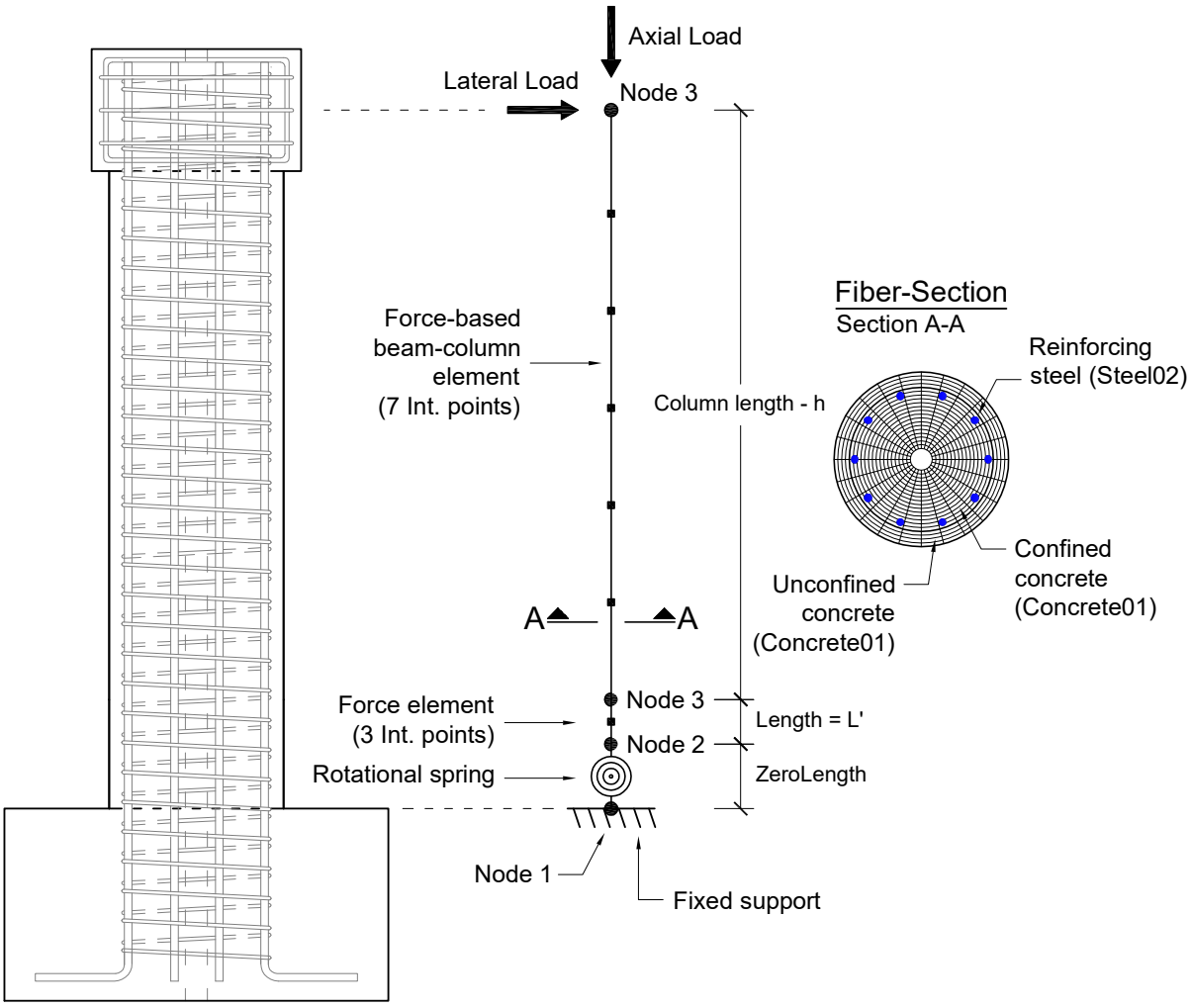

Figure 5.11: CIP40 1D fiber-section modeling schematic

5.3.5.2 Precast Columns

Fig. 5.12 depicts the schematic of the 1D modeling for PCU40. The modeling configuration is similar to that of CIP40. However, different fiber sections were used for the two force beam-column elements. The first element used for UHPC connection was modeled with unconfined concrete discretized into 20 circumferential and 24 radial fibers, and reinforced with 10 HS bars. The second element used to model the precast column shaft had unconfined cover and confined core with the same discretization scheme to the CIP columns and were

reinforced with 10 NS bars. An additional rotational spring was included at the column-connection interface to account for bond-slip rotation created by slip of longitudinal bars in the UHPC connection. $M - \phi$ analyses were performed at the section above the footing-connection interface and the section above the column shaft-connection interface. Peak bond stresses characterized from pullout modeling for HS and NS bars embedded in UHPC were utilized in Eq. 5.3 and 5.4 of Wehbe's method to determine the moment-rotation "Hysteretic" material parameters. Concrete and steel, and moment-rotation material parameters for the precast columns are listed in Table 5.4 and 5.5, respectively.

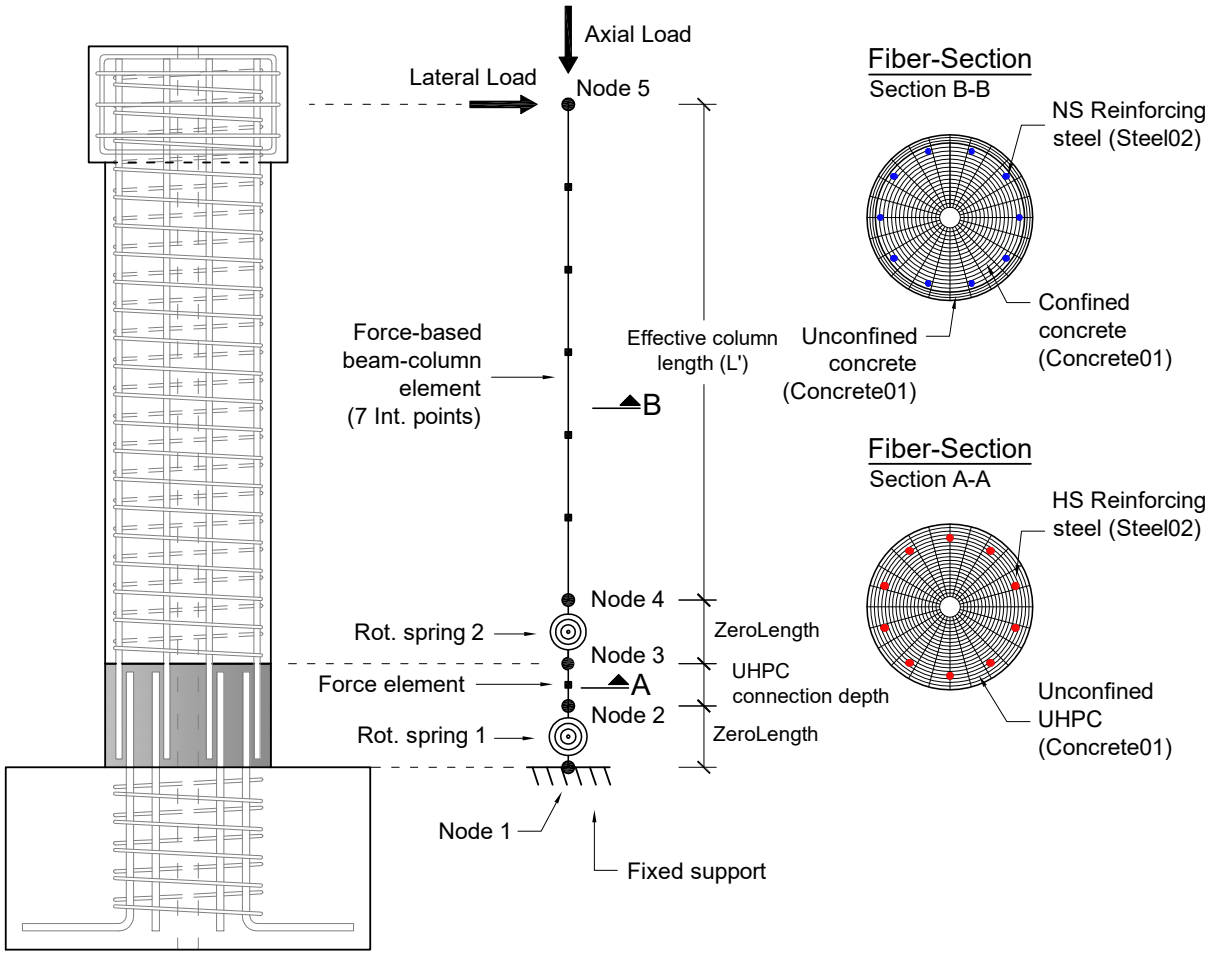

Figure 5.12: PCU40 1D fiber-section modeling schematic

Table 5.4: Concrete and steel material parameters for precast columns

Material Description	Parameters	CIP40	CIP25
Unconfined concrete (Concrete01)	f'_c (ksi)	8.02	8.29
	f'_{cu} (ksi)	0	0
	ε_{co} (in/in)	0.003	0.003
	ε_{cu} (in/in)	0.008	0.008
Confined concrete (Concrete01)	f'_c (ksi)	8.02	8.29
	f'_{cc} (ksi)	10.0	10.12
	f'_{cu} (ksi)	9.27	9.41
	ε_{cc} (in/in)	0.007	0.0067
	ε_{cu} (in/in)	0.0139	0.0127
Unconfined UHPC (Concrete01)	f'_c (ksi)	20.63	21.25
	f'_{cu} (ksi)	0	0
	ε_{co} (in/in)	0.004	0.004
	ε_{cu} (in/in)	0.008	0.008
NS longitudinal bar (Steel02)	f_y (ksi)	65.2	62.9
	E_s (ksi)	29000	29000
	b	0.0195	0.0183
	$R0$	20	20
	$CR1$	0.925	0.925
	$CR2$	0.15	0.15
Low cylce fatigue (Fatigue)	$E0$	0.191	0.191
	m	-0.4	-0.4
HS dowel (Steel02)	f_y (ksi)	65.2	62.9
	E_s (ksi)	29000	29000
	b	0.001	0.001
	$R0$	2.5	2.5
	$CR1$	0.925	0.925
	$CR2$	0.15	0.15

Table 5.5: Moment-rotation material parameters for precast columns

Material Description	OpenSees Material	Parameters	CIP40	CIP25
Moment-rotation above connection	Hysteretic (Multi-linear backbone)	M_1 (kip-in)	0	0
		M_2 (kip-in)	3412	2664
		M_3 (kip-in)	4174	3211
		θ_1	0	0
		θ_2	0.0011	0.0006
		θ_3	0.0298	0.0205
		B	0.5	0.5
Moment-rotation at the footing	Hysteretic (Multi-linear backbone)	M_1 (kip-in)	0	0
		M_2 (kip-in)	7480	5780
		M_3 (kip-in)	7480	5982
		θ_1	0	0
		θ_2	0.003	0.0021
		θ_3	0.0128	0.0077
		B	0.5	0.5

Notes: Moment-rotation is formed by three positive and three negative backbone points
M_2 and θ_2 are the effective yield moment and rotation
M_3 and θ_3 are the plastic moment and rotation

5.4 Two-Dimensional (2D) Modeling for Columns

5.4.1 General Concepts

Previous sections discuss the typical modeling methods utilizing one-dimensional force-based beam-column elements with fiber sections to model seismic CIP and precast bridge columns. Longitudinal bar slip in the footing or connection concrete is either implicitly included in the constitutive model of reinforcing bars or indirectly assumed from bond-slip rotation that occurs at the column-footing and column-connection interfaces. Although good correlation between the predicted and measured responses were observed in past studies, the assumptions in the 1D modeling may not realistically represent the load transfer in the footing and the connection. This section examines the use of two-dimensional

plane stress finite element continuum models for both the CIP and precast columns. The advantage of continuum modeling is the ability to explicitly apply the uniaxial bond stress-slip relationship determined from pullout test to model slip between reinforcing bar and concrete. Responses are compared with the 1D modeling responses and the experimental results.

5.4.2 Modeling Method

5.4.2.1 CIP Columns

The two CIP columns were modeled using 2D plane stress FEM software VecTor2. The software employs a smeared, rotating-crack formulation for reinforced concrete following the modified compression field theory (MCFT) and the disturbed stress field model (DSFM). Fig. 5.13 depicts the schematic of the 2D modeling for CIP40 (also applicable to CIP25 with reduced column length). The modeling simplified the circular cross section of the column shaft to an equivalent combined rectangular cross sections with varying thicknesses. Four-noded rectangular elements were used to model the unreinforced concrete cover and the concrete core reinforced with smeared transverse steel. Longitudinal reinforcing bars were modeled with discrete truss elements. Link elements were used to connect between all the discrete truss and rectangular elements to represent bond-slip. The link elements are zero-length two-noded elements with two orthogonal springs that allow slippage between rebar and concrete elements [77]. The footing concrete was modeled with four-noded rectangular elements with smeared longitudinal and transverse steel ratio. Pinned and roller supports were applied to the footing base and top surface, respectively to prevent overturning and sliding. A line of truss elements with large cross sectional areas were used at the loading point to avoid stress concentration.

Concrete material properties in plane stress elements differ from the uniaxial material. Concrete exhibits the increase or decrease of compressive strength depending on

multiple factors such as transverse cracking, tensile straining, lateral expansion, and confinement due to transverse reinforcement. In VecTor2, only unconfined average test-day concrete compressive strength, strain at peak stress, and elastic modulus were input. The reduced and increased compressive strength were internally calculated based on transverse cracking and tensile straining levels, and the ratio of smeared transverse steel using predefined models. Various concrete constitutive models are described in VecTor2 manual [78] and are not repeated here. "Popovic (NSC)" , "Modified Park-Kent", "Vecchio-Collins 1986", and "Kupfer-Richart" were used for compression pre-peak, post-peak, softening, and strength enhancement, respectively. The models were selected based on the pre-calibration of a single concrete element to prevent significant difference of concrete constitutive models used in the OpenSees 1D modeling. "Modified Bentz 2003" and "bilinear" models were chosen for tension stiffening and tension softening, respectively. Both tension constitutive models may not significantly influence the column behavior, but ensure smooth modeling convergence. Assumed $7.5\sqrt{f'_c}$ (f'_c is in psi) and no tensile strengths were used for the confined concrete core and concrete cover, respectively. "Plastic offsets nonlinear with cyclic decay" based on "Palermo" model was used for compression and tension hysteretic responses.

"Bauschinger Effect-Seckin" constitutive model was utilized for both NS and HS reinforcing bars. NS and HS used the same material properties as listed in Table 2.5. However, hardening strain ε_{sh} of 0.009 and 0.00345 were used for NS and HS, respectively to obtain similar stress and strain relationships that match the tension test data. "Eligenhausen" bond-slip model with full confinement was employed for CIP columns.

The column model was subjected to a constant axial load of 126 kips distributed equally to 19 nodes of the column head. Displacement-based loading was imposed at the center of the column head, and cyclically increased based on drift targets from the experiment. To reduce the computation time in VecTor2, the cyclic response of the FEM modeling was started at 1% drift. In addition, it was necessary to disable the crack width check criteria

of concrete to ensure numerical convergence in VecTor2. Realistically, a well-detailed seismic column is still capable of supporting lateral load after spalling of unconfined concrete cover prior to crushing of concrete core or fracture of longitudinal reinforcement.

5.4.2.2 Precast Columns

Fig. 5.14 depicts the schematic of the 2D modeling for PCU40. The modeling configuration is similar to that of CIP40 with the exception of the modeling details in the connection region. Compressive and tensile strength of concrete in the connection region used the average test-day compressive and post-peak tensile strength of UHPC, respectively. Column longitudinal reinforcing bars and footing dowels were lapped in the connection, requiring finer mesh size of the four-noded rectangular elements to accommodate the discrete truss elements at approximately the same locations to those in the physical specimen. Link elements were used to connect between all the discrete truss and rectangular elements to represent bond-slip. Bond-slip model that has matched bond stress-slip constitutive to the calibrated pullout test is not available in VecTor2. Therefore, "Eligehausen" model was employed as the bond-slip constitutive model for both NS and HS reinforcing bars. Initially, unconfined model that exhibits approximately the same peak bond stress to the calibrated value in the pullout test was selected. The final value of confinement pressure factor of 0.2 resulted in better correlation with experimental results. It is important noting that "Eligehausen" model has larger slip δ_3 of 0.12 in than the calibrated value. Bond stress-slip between the NS and UHPC, and between HS and UHPC can be slightly different due to the different bar diameters. For PCU25, the same material constitutive models, element types, and loading based on target drift levels were applied with reduced column shaft length and UHPC connection height.

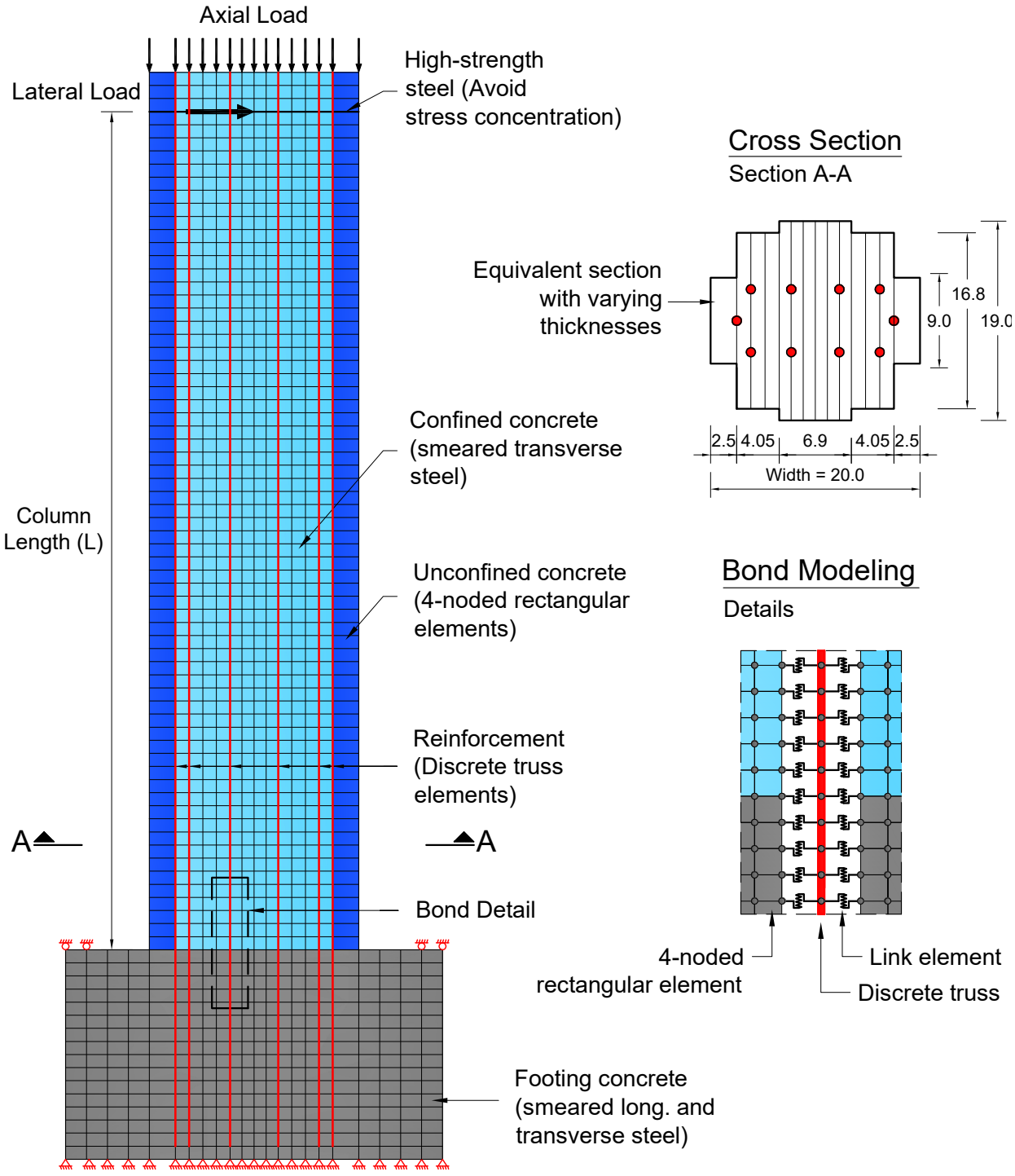

Figure 5.13: CIP40 2D plane stress modeling schematic

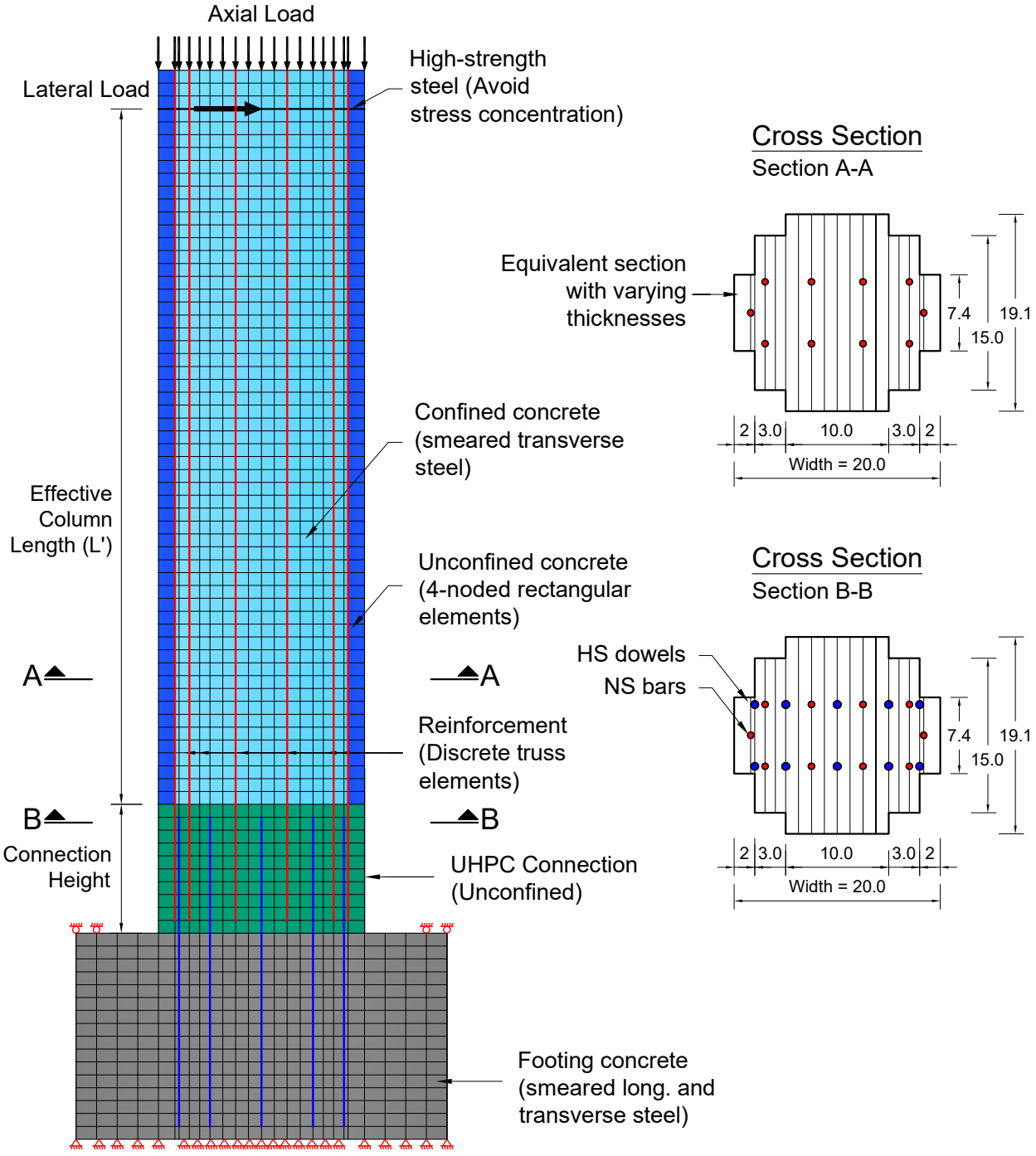

Figure 5.14: PCU40 2D plane stress modeling schematic

5.5 Analytical Modeling Results

5.5.1 Force-Drift Relationships

Fig. 5.15 and 5.16 show the side-by-side comparison of the calculated force-drift hysteresis loops for CIP columns using 1D fiber-section and 2D plane stress modelings with reference to the measured curves. For CIP40, the predicted and measured responses showed good agreement in terms of overall strength, unloading and reloading stiffness, and the pitching locations. However, the two modelings overestimated approximately 10% lateral load at 1% drift and after 3% drift. Cover loss may contribute to the measured load drop at 3% drift. For CIP25, the modeling methods were also able to predict reasonably the hysteretic responses, with exception of the initial stiffness that may be reduced due to out of plane loading during the test. The difference of lateral load approximately 8% was observed in the push direction, which was attributed to the unsymmetrical side cover due to construction error. Better unloading and reloading stiffness was captured by the 2D plane stress in CIP25 modeling. It should be noted that both CIP columns ultimately failed due to longitudinal bar buckling. This failure mode could not be captured by the two modeling methods.

Fig. 5.17 and 5.18 depicts the predicted and measured force-drift hysteresis loops for the precast columns. Better correlation of the initial, unloading and reloading stiffness was predicted in the precast column using 1D fiber-section and 2D plane stress modelings. Strength of PCU40 was well quantified by both methods. The 2D modeling had better prediction on strength of PCU25. In regard to the local responses, the 1D fiber-section was able to determine bar fracture of PCU40 using low cycle fatigue material, yet unable to simulate bond failure of PCU25. On the other hand, low cycle fatigue material does not exist in VecTor2. Only bond failure of PCU25 was captured by the 2D modeling.

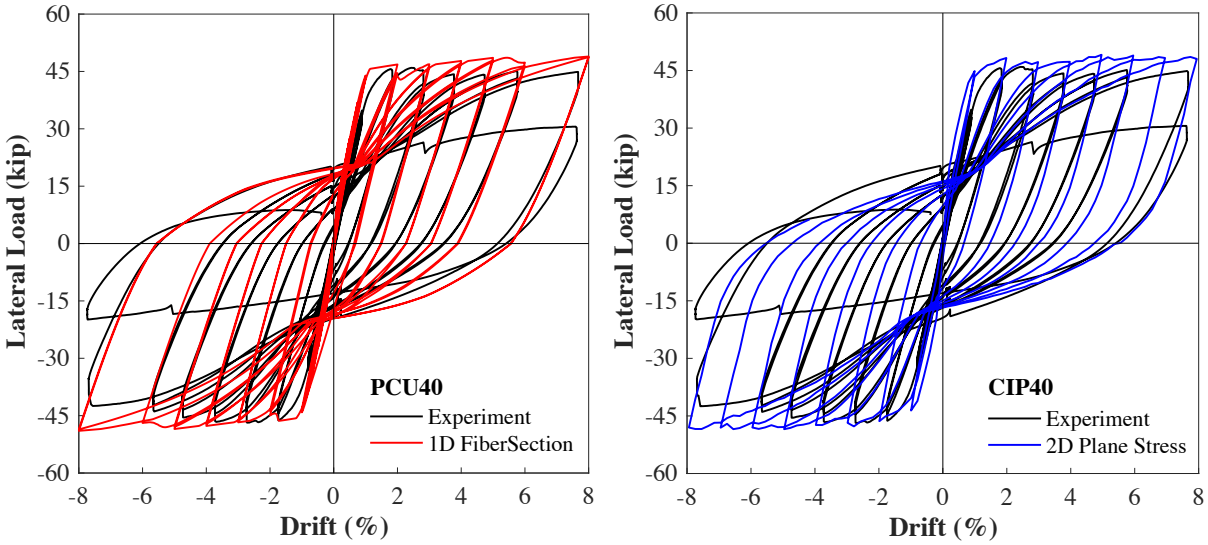

(a) CIP40 1D fiber-section

(b) CIP40 2D Plane Stress

Figure 5.15: Measured and calculated force-drift hysteresis curves for CIP40

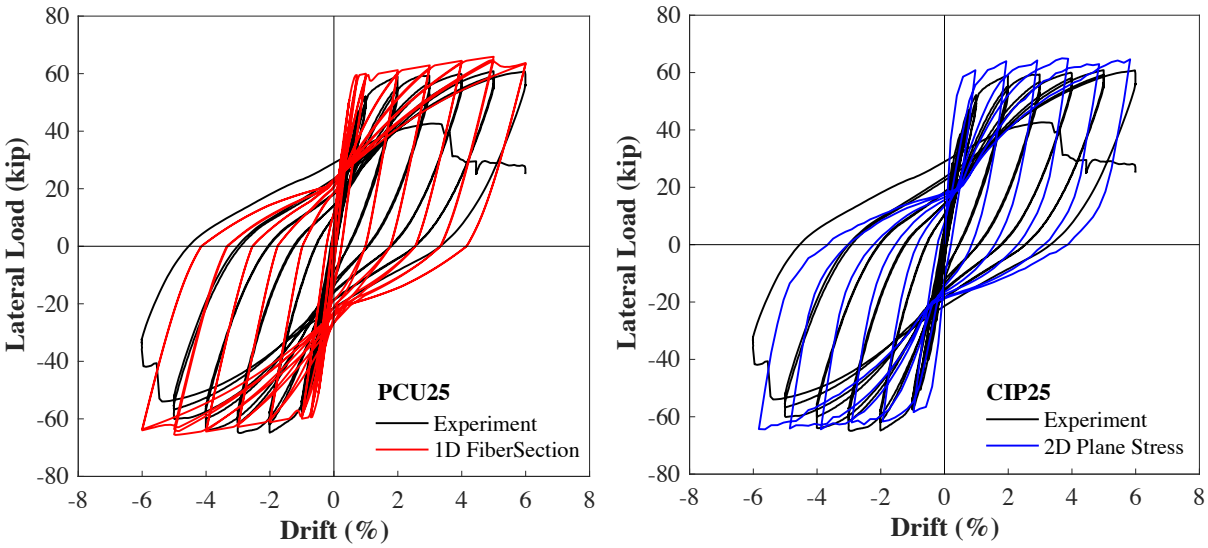

(a) CIP25 1D fiber-section

(b) CIP25 2D Plane Stress

Figure 5.16: Measured and calculated force-drift hysteresis curves for CIP25

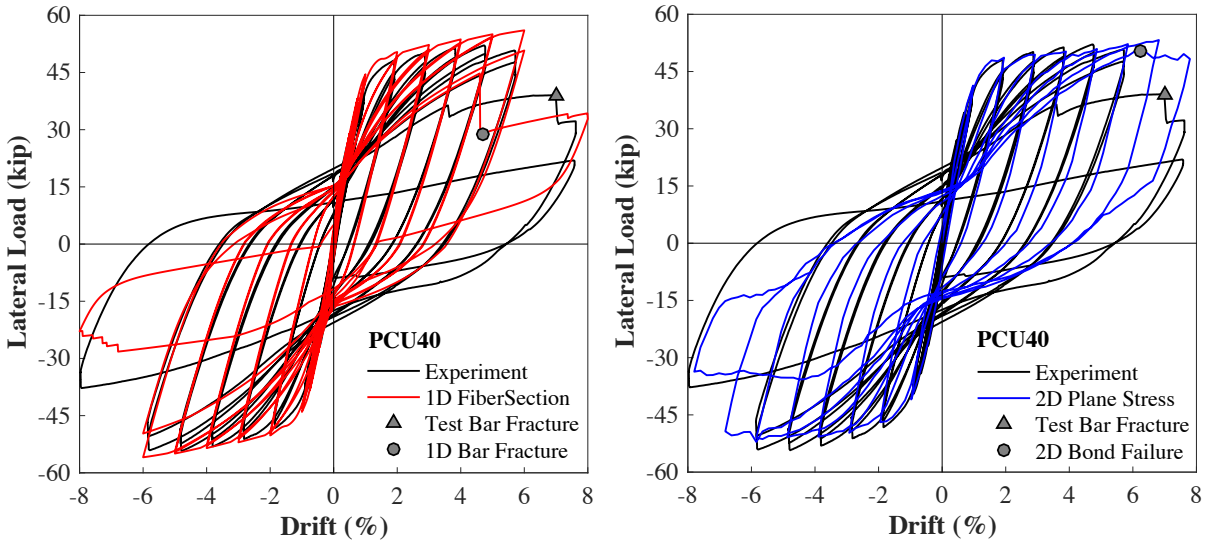

(a) PCU40 1D fiber-section

(b) PCU40 2D Plane Stress

Figure 5.17: Measured and calculated force-drift hysteresis curves for PCU40

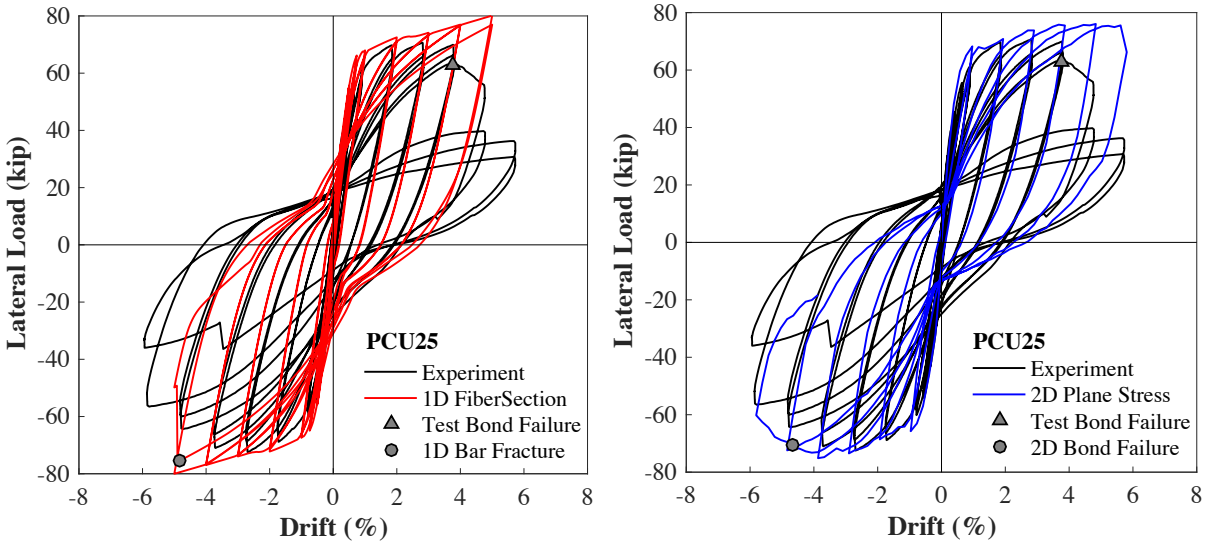

(a) PCU25 1D fiber-section

(b) PCU25 2D Plane Stress

Figure 5.18: Measured and calculated force-drift hysteresis curves for PCU25

5.5.2 Energy Dissipation

The measured and predicted cumulative energy dissipation for CIP and precast columns was illustrated in Fig. 5.19 and 5.20. The energy dissipation was determined by calculating the area enclosed by each hysteresis loop. Only one loading cycle was simulated using 2D plane stress. Therefore, the first loading cycle energy dissipation was compared for consistency. For CIP columns, the calculated energy dissipation slightly exceeded the measured values. At 2% drift the differences ranged between 22% and 28%, and eventually dropped to an average of approximately 18% and 12% at the failure drift for 1D and 2D modelings, respectively. The higher calculated energy dissipation was not unexpected due to the slightly higher predicted strength, and unloading and reloading stiffness. For precast columns, energy dissipation simulated by the 2D modeling was almost the same to measured values with only 3% difference at the failure drift. Similarly, the 1D modeling obtained close prediction for PCU40, but overestimated the energy dissipation of approximately 27% for PCU25.

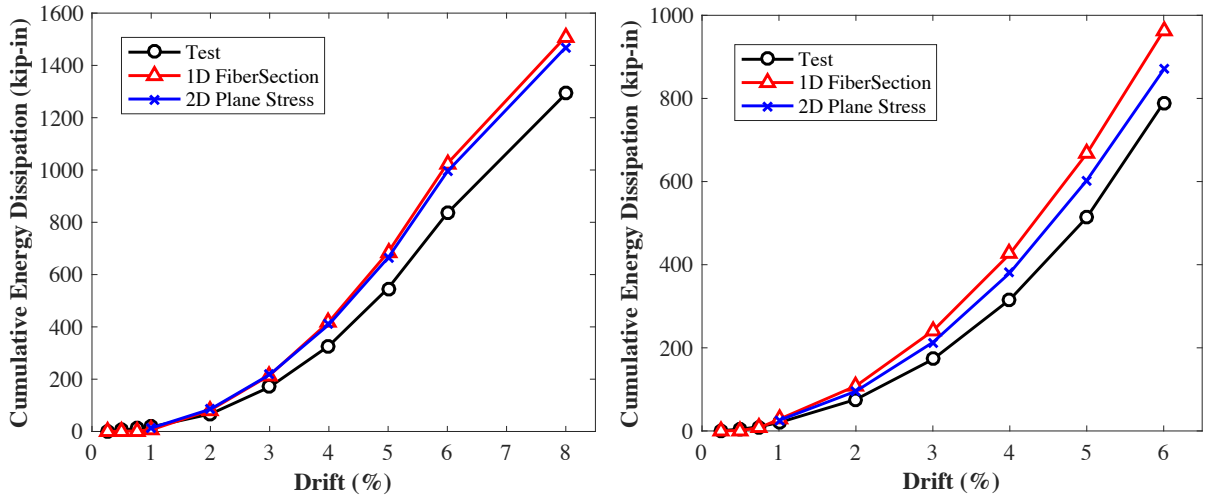

(a) CIP40 (b) CIP25

Figure 5.19: Measured and calculated cumulative energy dissipation for CIP columns

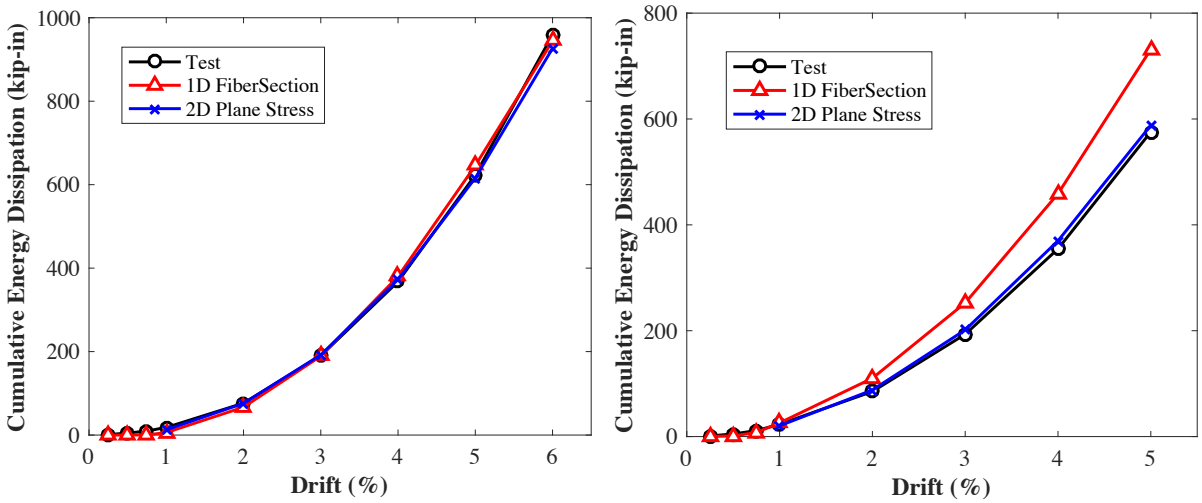

(a) PCU40

(b) PCU25

Figure 5.20: Measured and calculated cumulative energy dissipation for precast columns

CHAPTER 6: SUMMARY, CONCLUSIONS, AND FUTURE WORKS

6.1 Summary

Accelerated bridge construction (ABC) is bridge construction or rehabilitation that uses innovative design, materials, and construction techniques to expedite construction time, reduce traffic disruption, increase quality control, and provide promising cost-effective long-lasting bridge. ABC has been increasingly used for bridge elements in low seismic regions. However, its applications in medium and high seismic regions remain limited, particularly for precast columns where the connections typically coincide with plastic hinge (PH) regions that can undergo major damage after a strong earthquake event. Ultra-high performance concrete (UHPC), characterized by high compressive and tensile strength, and superior bond properties that can significantly reduce rebar embedment length, is a potential candidate to enhance the seismic performance of precast bridge column connections.

A new and simple damage-tolerant precast column connection utilizing UHPC was proposed in this research for use in medium and high seismic regions. The connection laps the column longitudinal reinforcement with footing dowels using a short splice length, a practical concrete cover, with no shear reinforcement in the connection region. In addition to utilizing UHPC, the connection uses the shifted plastic hinge (SPH) design concept to re-locate the PH above the connection region and prevent footing damage. The proposed connection was investigated experimentally by testing two 0.42-scale precast columns (one flexural and one flexural-shear) under reversed cyclic loading. Responses of the precast columns were compared with two reference cast-in-place (CIP) columns from previous study.

The research in current study further investigated the local bond performance of reinforcing steel embedded in UHPC under varying parameters including embedment length,

side cover, bar size and bar strength and under different stress states. Twenty-one specimens were tested using a simplified direct tension pullout test and six lap splice beams were subjected to bending load. The study focuses on reinforcing bars embedded in UHPC that has small side cover with limited data available in the literature. The primary findings from the component-level tests were used to recommend the unconfined bond strength and suggest the minimum embedment length required to develop NS and HS reinforcing steel in UHPC.

Finally, the pullout specimens were analytically simulated using OpenSees framework to propose the bond-slip models of reinforcing steel embedded in UHPC. The models were incorporated into the numerical modeling of the precast columns to predict the column responses using one-dimensional fiber-section and two-dimensional plane stress nonlinear analyses. The analytical results were compared with the experiments to validate the modeling methods.

6.2 Conclusions and Recommendations

Based on the experimental program and results of the two precast column tests, several main conclusions are summarized as follows:

1. Utilization of a non-contact lap splice without shear reinforcement provided large field tolerance and avoided congested reinforcement. The simple use of PVC vent installed at the base of the precast column shaft worked well in the proposed connection construction that prevented retention of air voids in the interface between UHPC connection and precast column.

2. Damage in the precast columns occurred above the UHPC region with no apparent cracks at the footing surface. Strains below yielding were measured in the HS footing dowels that confirmed the shift of PH formation as per the design objective.

3. Minor flexural and splitting cracks in the UHPC connection and fracture of the extreme NS longitudinal bars above the connection showed the efficient use of UHPC in reducing connection damage and developing the short lap-spliced reinforcement under strong seismic loading.

4. The precast columns using the proposed UHPC connection exhibited high lateral load and displacement ductility capacity due to two main contributions: the shift of PH formation and the bond-slip of NS longitudinal bars into UHPC connection. Deformation results also revealed the shear deformation contribution was not significant in the proposed UHPC connection. In addition, the well-distributed plastic reinforcing strains in the hinge region above the connection represented the larger PH length of the precast columns compared with CIP columns.

5. Bond-slip response of UHPC lap splice is affected by the large inelastic deformations, cyclic loading, and high shear demands, which resulted in bond failure south of the short precast column. Despite the critical splitting cracks of UHPC due to pullout failure, the proposed UHPC connection maintained stiffness, and displayed stable hysteresis response and comparable energy dissipation relative to the reference CIP column. Either larger splice length than $12d_b$ or minimal shear reinforcement is recommended for short precast column utilizing UHPC lap splice connection to prevent bar pullout failure and critical splitting cracks. Shear reinforcement could also be added in the connection region to improve confinement and column displacement ductility.

On the other hand, experimental results of component-level specimens and the analytical modeling results contribute to the following conclusions and recommendations:

1. Bond stress-slip relationship of reinforcing bar embedded in UHPC is affected by concrete side cover and bar strength. The increase of side cover increases peak and residual

bond stresses and the corresponding slips. The bond strength is less affected by embedment length and bar size.

2. A minimum embedment length of $10d_b$ with side cover of $1.4d_b$ is recommended to develop NS Gr. 60 reinforcing steel under pure tension or bending stress states.

3. Unconfined bond strength of $0.29\sqrt{f'_c C_s/d_b}$ and $0.32\sqrt{f'_c C_s/d_b}$ are recommended for NS and HS reinforcing steel embedded in UHPC respectively (where f'_c is in ksi).

4. The proposed peak bond stress utilized with the typical 1D fiber-section modeling in OpenSees provides a good prediction of the CIP and precast column responses.

5. The 2D plane stress modeling provides alternative prediction of the global and local responses of the CIP and precast columns with realistic representation of bond stress-slip.

6.3 Future Work

Current research shows the applicability of a simple but efficient UHPC lap splice connection for use in medium and seismic regions. Suggested analytical modeling methods are also able to capture the responses of the precast columns. However, there are several knowledge gaps for this connection type and possible areas for expanding future research studies. The following aspects can be considered for the future work:

1. The findings of current study were based on two precast column tests with limited design parameters. Additional studies are required to validate the applicability of the proposed UHPC lap splice connection for different reinforcing ratios, splice lengths, side cover, aspect ratios, and axial load levels.

2. Unconfined bond stress-strain slips of reinforcing steel embedded in UHPC under direct tension and bending stress states were the focus of the current research. The study of

the bond-slip models can be extended to specimens with different confinement levels and under different stress states such as combined flexural-shear and cyclic loading.

3. Design guidelines for this connection type to obtain desired lateral capacity and displacement ductility is another interesting topic that requires further investigation.

4. The UHPC connection in this study is proposed for ABC precast column construction, yet similar connection details can be extended for accelerated repair and retrofitting of sub-structural elements.

APPENDIX : INSTRUMENTATION DETAILS OF PRECAST COLUMNS

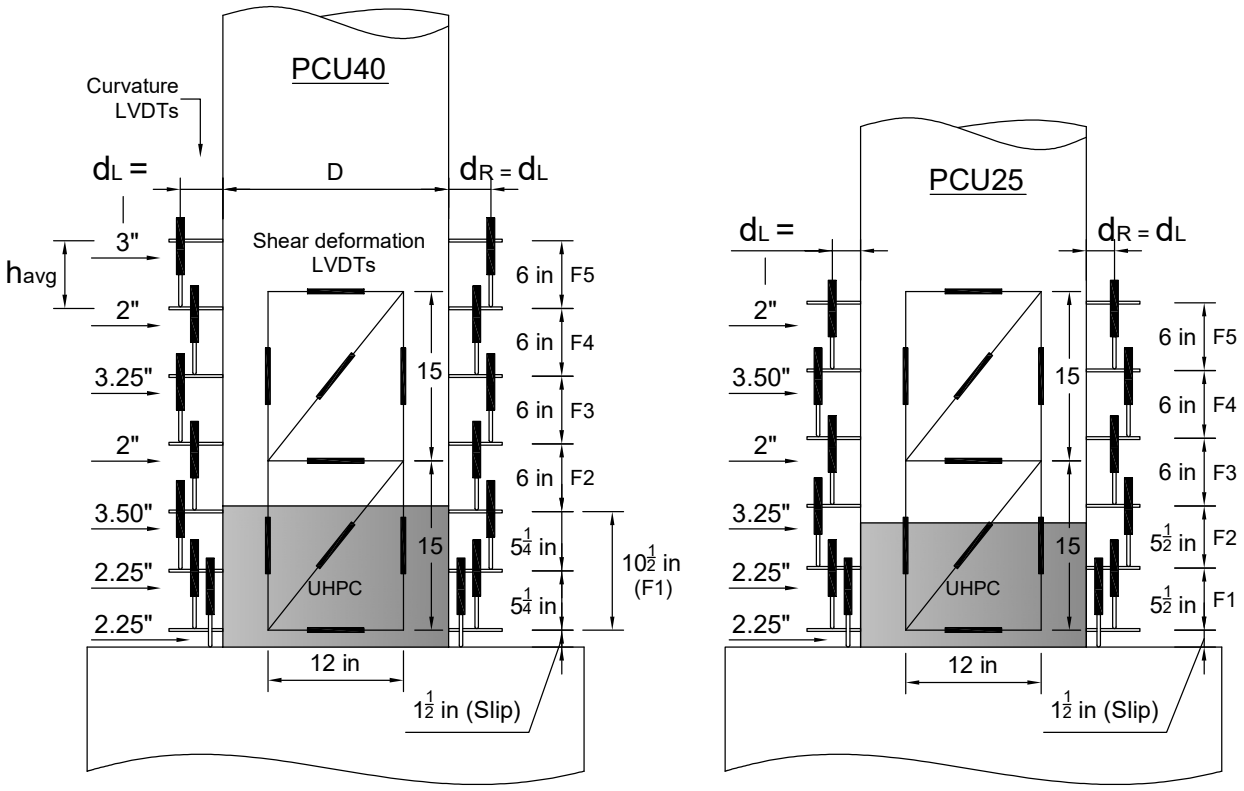

Figure .1: Details of LVDT instrumentation for precast columns

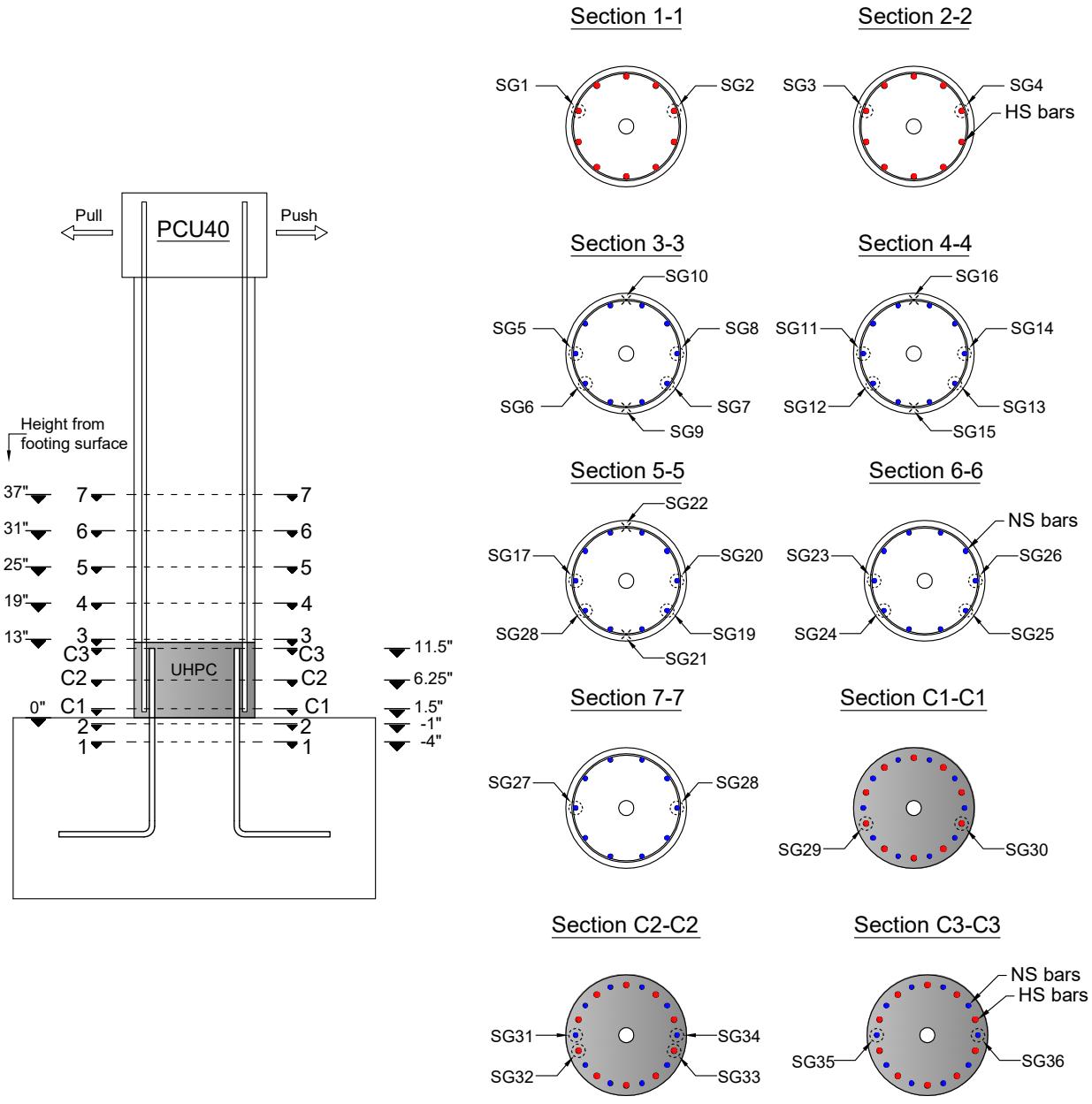

Figure .2: Details of strain gauges instrumentation for PCU40

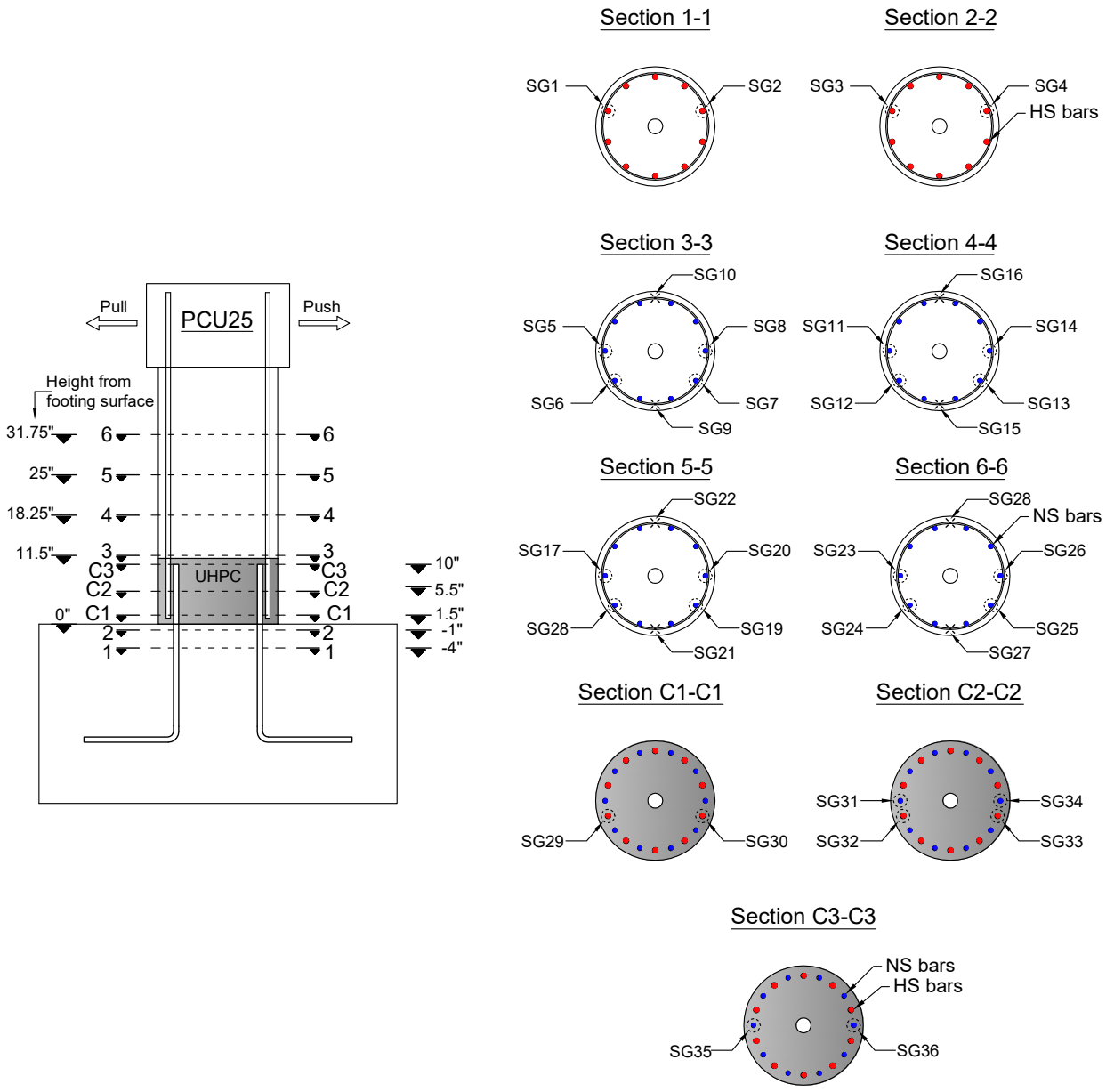

Figure .3: Details of strain gauges instrumentation for PCU25

LIST OF REFERENCES

[1] ASCE, *2017 infrastructure report card*, ASCE Reston, VA, 2017.

[2] INRIX Traffic, *http://www.inrix.com*, 2018, (accessed 02.26.2019)

[3] Culmo, M.P., *Accelerated bridge construction-experience in design, fabrication and erection of prefabricated bridge elements and systems*, Report No. FHWA-HIF-12-013, 2011.

[4] Restrepo, J. I, Tobolski, M. J., and Matsumoto, E. E., *Development of a Precast Bent Cap System for Seismic Regions*, NCHRP Report No 681, Transportation Research Board, Washington, DC, 2011, 106pp.

[5] Blaise, P.Y. and Couture, M., *Precast, Prestressed Pedestrian Bridge—World's First Reactive Powder Concrete Structure*, PCI Journal, Vol. 44, No. 5, September/October 1999, pp. 60–71.

[6] Ricciotti, R., *The Footbridge of Peace, Seoul, South Korea*, Concrete, Vol. 36, No. 10, November/December 2002, pp. 11–13.

[7] Hajar, Z. et al., *Design and Construction of the World First Ultra-High Performance Concrete Road Bridges*, Proceedings of the International Symposium on Ultra High Performance Concrete, Ed., Schmidt, M., Fehling, E., and Geisenhansluuke, C., Kassel University Press, Kassel, Germany, 2004, pp. 39–48.

[8] Bierwagen, D. and Abu-Hawash, A., *Ultra High Performance Concrete Highway Bridge*, Proceedings of the 2005 Mid-Continent Transportation Research Symposium, Ames, IA, August 2005.

[9] Lafargeholcim, *https://www.lafargeholcim.com/ductal*

[10] Russell, H. G., and Graybeal, B. A., *Ultra-High Performance Concrete: A State-of-the-Art Report for the Bridge Community*, Report No. FHWA-HRT-13-060, FHWA, Washington, DC, 2013.

[11] Marsh, M. L., Wernli, M., Garrett, B. E., Stanton, J. F., Eberhard, M. O., and Weinert, M. D., *Application of accelerated bridge construction connections in moderate-to-high seismic regions*, NCHRP Report 698, 2011.

[12] Haber, Z. B., Saiidi, M. S., and Sanders, D. H., *Seismic Performance of Precast Columns with Mechanically Spliced Column-Footing Connections*, ACI Structural Journal, V. 111, No. 3, 2014, pp. 639–650.

[13] Ameli, M., Parks, J. E., Brown, D. N., and Pantelides, C. P., *Seismic Evaluation of Grouted Splice Sleeve Connections for Reinforced Precast Concrete Column-to-Cap Beam Joints in Accelerated Bridge Construction*, PCI Journal, V. 60, No. 2, 2015, pp. 80-103.

[14] Ameli, M. J., Brown, D. N., Parks, J. E., and Pantelides, C. P., *Seismic Column-to-Footing Connections Using Grouted Splice Sleeves*, ACI Structural Journal, V. 113, No. 5, 2016, pp. 1021–1030.

[15] Tazarv, M., *Next Generation of Bridge Columns for Accelerated Bridge Construction in High Seismic Zones*, PhD thesis, University of Nevada, Reno, 2014, 400pp.

[16] Haber, Z. B., Mackie, K. R., and Al-Jelawy, H. M., *Testing and Analysis of Precast Columns with Grouted Sleeve Connections and Shifted Plastic Hinging*, Journal of Bridge Engineering, ASCE, V. 22, No. 10, 2017, p. 04017078.

[17] Matsumoto, E., Waggoner, M., Sumen, G., Kreger, M., Wood, S., and Breen, J., *Development of a Precast Bent Cap System*, Report No. 1748-02. Center for Transportation Research, The University of Texas at Austin, 2001.

[18] Matsumoto, E. *Emulative Precast Bent Cap Connections for Seismic Regions: Component Test Report—Grouted Duct Specimen (Unit 2)*, Report No. ECS-CSUS-2009-02. California State Univer- sity, Sacramento, 2009b.

[19] Pang, J. B., Eberhard, M. O., and Stanton, J. F., *Large-bar connection for precast bridge bents in seismic regions*, Journal of Bridge Engineering, 15(3), 2009, 231-239.

[20] Mehraein, M., *Seismic Performance of Bridge Column-Pile-Shaft Pin Connections for Application in Accelerated Bridge Construction*, PhD thesis, University of Nevada, Reno, 2016, 734pp.

[21] Haraldsson, O., Janes, T., Eberhard, M., and Stanton, J., *Seismic Resistance of Socket Connection between Footing and Precast column*, Journal of Bridge Engineering, ASCE, V. 18, No. 9, 2013, pp. 910–919.

[22] Mehrsoroush, A. and Saiidi, M.S., *Experimental and Analytical Seismic Studies of Bridge Piers with Innovative Pipe Pin Column-Footing Connections and Precast Cap Beams*, Report No. CCEER-14-07, Center For Civil Engineering Earthquake Research, University of Nevada, Reno, Nevada, 2014, 711 pp.

[23] Motaref, S., Saiidi, M.S., and Sanders, D., *Seismic Response of Precast Bridge Columns with Energy Dissipating Joints*, Report No. CCEER-14-07, Center For Civil Engineering Earthquake Research, University of Nevada, Reno, Nevada, 2011, 760 pp.

[24] Marriott, D., Palermo, A., and Pampanin, S., *Quasi-static and Pseudo- Dynamic Testing of Damage Resistant Bridge Piers with Hybrid Connections*, Proceeding of the First

European Conference on Earthquake Engineering and Seismology, Geneva, Switzerland, Paper No. 794, 2006.

[25] Yamashita, R. and Sanders, D. H. , *Seismic performance of precast unbonded prestressed concrete columns*, ACI structural journal, 106(6):821, 2009.

[26] Vachon, D. and Massicotte, B., *Seismic retrofitting of rectangular bridge piers with FRC jackets*, Proceeding of the sixth RILEM symposium of fibre-reinforced concrete, Varrena, Italy, 2004, pp. 1247-1256.

[27] Dagenais MA, Massicotte B, Boucher-Proulx G., *Seismic Retrofitting of Rectangular Bridge Piers with Deficient Lap Splices Using Ultrahigh-Performance Fiber-Reinforced Concrete*, Journal of Bridge Engineering. 2017 Nov 21;23(2):04017129.

[28] Tazarv, M., and Saiidi, M. S., *UHPC-Filled Duct Connections for Accelerated Bridge Construction of RC Columns in High Seismic Zones*, Engineering Structures, V. 99, No. 3, 2015, pp. 413–422.

[29] Tazarv, M., and Saiidi, M. S., *Low-Damage Precast Columns for Accelerated Bridge Construction in High Seismic Zones*, Journal of Bridge Engineering, ASCE, V. 21, No. 3, 2015, p. 04015056.

[30] Zohrevand, P., and Mirmiran, A., *Cyclic Behavior of Hybrid Columns Made of Ultra High Performance Concrete and Fiber Reinforced Polymers*, Journal of Composites for Construction, V. 16, No. 1, 2012, pp. 91-99.

[31] Ichikawa, S., Matsuzaki, H., Moustafa, A., ElGawady, M., and Kawashima, K., *Seismic-Resistant Bridge Columns with Ultrahigh-Performance Concrete Segments*, Journal of Bridge Engineering, ASCE, V. 21, No. 9, 2016, p. 04016049.

[32] Yang C, and Okumus P., *Ultrahigh-Performance Concrete for Posttensioned Precast Bridge Piers for Seismic Resilience*, Journal of Structural Engineering, ASCE, V. 143, No. 12, 2017, p. 04017161.

[33] Mohebbi, A., Saiidi, M. S., and Itani, A. M., *Shake Table Studies and Analysis of a PT-UHPC Bridge Column with Pocket Connection*, Journal of Structural Engineering, ASCE, V. 144, No. 4, 2018, p. 04018021.

[34] Haber, Z.B., De la Varga, I., Graybeal, B.A., Nakashoji, B. and El-Helou, R., *Properties and behavior of UHPC-class materials*, No. FHWA-HRT-18-036, Federal Highway Administration. Office of Infrastructure Research and Development, 2018.

[35] King Packaged Materials Company, *UP-FX poly technical data sheet*, http://www.kpmindustries.com/KingConstructionProducts/product/up-f2-poly-concrete, 2018.

[36] Graybeal, B.A., *Material property characterization of ultra-high performance concrete*, Report No. FHWA-HRT-06-103, Federal Highway Administration. Office of Infrastructure Research and Development, 2006.

[37] Association Francaise de Genie Civil, *Ultra high performance fibre-reinforced concretes-Interim Recommendations*, Paris, France, 2002.

[38] Chanvillard, G. and Rigaud, S., *Complete characterization of tensile properties of Ductal UHPFRC according to the French recommendations*, In Proceedings of the 4th International RILEM workshop High Performance Fiber Reinforced Cementitious Composites, 2003, pp. 21-34.

[39] Graybeal, B.A. and Baby, F., *Development of Direct Tension Test Method for Ultra-High-Performance Fiber-Reinforced Concrete*, ACI Materials Journal, 2013, 110(2).

[40] Zhou, Z., and Qiao, P., *Direct tension test for characterization of tensile behavior of ultra-high performance concrete*, Journal of Testing and Evaluation, V. 48, No. 4, 2018.

[41] Berke, S., *Reinforcing steel comparative durability assessment and 100 year service life cost analysis report*, Tourney Consulting Group, May 2012, p. 63.

[42] Williamson, G. S., Weyers, R. E., Sprinkel, M. M., and Brown, M. C., *Concrete and steel type influence on probabilistic corrosion service life*, ACI Materials Journal, V. 106, No. 1, 2009, p. 82.

[43] Ansley M. H., *Investigation into the structural performance of MMFX reinforcing bars*, MMFX Steel Corporation: Technical Resources, 2002, 12 pp.

[44] Saleem, M. A., Mirmiran, A., Xia, J. and Mackie, K., *Ultra-high-performance concrete bridge deck reinforced with high-strength steel*, ACI Structural Journal, V. 108, No. 5, 2011.

[45] Chan, T., Mackie, K. R., and Haber, Z. B., *Precast seismic bridge column connection utilizing ultra-high performance concrete lap splice*, ACI Structural Journal, 2019 (Accepted).

[46] Graybeal, B. A., *Design and construction of field-cast UHPC connections*, FHWA-HRT-14-084, Federal Highway Administration, Washington, DC, 2014.

[47] Yuan, J., and Graybeal, B. A., *Bond of reinforcement in ultra-high- performance concrete*, ACI Struct. J., 112(6), 2015, pp. 851–860.

[48] Al-Jelawy, H. M., Mackie, K. R., and Haber, Z. B., *Shifted Plastic Hinging for Grouted Sleeve Column Connections*, ACI Structural Journal, V. 115, No. 4, 2018, pp. 1101-1114.

[49] Caltrans, S. D. C., *Caltrans Seismic Design Criteria Version 1.7*, California Department of Transportation, Sacramento, 2013.

[50] Scott, B., Park, R., Priestley, M., et al., *Stress-strain behavior of concrete confined by overlapping hoops at low and high strain rates*, ACI Journal, V. 79, No. 1, 1982, pp.13–27.

[51] Mander, J., Priestley, M., and Park, R., *Theoretical stress-strain model for confined concrete*, Journal of Structural Engineering, V. 114, No. 8, 1988, pp. 1804–1826.

[52] Priestley, M. and Park, R., *Strength and ductility of concrete bridge columns under seismic loading*, ACI Structural Journal, V. 84, No. 1, 1987.

[53] Chang, G.A., and Mander, J.B., *Seismic Energy Based Fatigue Damage Ananlysis of BridgeColumns: Part 1 – Evaluation of Seismic Capacity*, NCEER Technical Report No. NCEER-94-0006, 1994.

[54] ASTM C39/C39M-15a, *Standard test method for compressive strength of cylindrical concrete specimens*, ASTM International, West Conshohocken, PA, 2015, 4 pp.

[55] ASTM C1856/C1856M-17, *Standard practice for fabricating and testing specimens of ultra-High performance concrete*, West Conshohocken, PA, 2017, 8 pp.

[56] ASTM A615/A615M-16, *Standard specification for deformed and plain carbon-steel bars for concrete reinforcement*, West Conshohocken, PA, 2016a, 8 pp.

[57] ASTM A1064/A1064M-17, *Standard specification for carbon-steel wire and welded wire reinforcement plain and deformed, for concrete*, West Conshohocken, PA. 2017, 11 pp.

[58] ASTM A1035/A1035M-16b, *Standard Specification for Deformed and Plain, Low-Carbon, Chromium, Steel Bars for Concrete Reinforcement*, West Conshohocken, PA, 2016b, 8 pp.

[59] ASTM A370-17a, *Standard Test Methods and Definitions for Mechanical Testing of Steel Products*, International, West Conshohocken, PA, 2017, 50 pp.

[60] Graybeal, B.A., *Behavior of field-cast ultra-high performance concrete bridge deck connections under cyclic and static structural loading*, No. FHWA-HRT-11-023, United States Federal Highway Administration, 2010.

[61] Saleem, M.A., Mirmiran, A., Xia, J. and Mackie, K., *Development length of high-strength steel rebar in ultrahigh performance concrete*, Journal of Materials in Civil Engineering, 25(8), 2012, pp.991-998.

[62] Alkaysi, M. and El-Tawil, S., *Factors affecting bond development between Ultra High Performance Concrete (UHPC) and steel bar reinforcement*, Construction and Building Materials, 144, 2017, pp.412-422.

[63] Haber, Z.B. and Graybeal, B.A., *Lap-Spliced Rebar Connections with UHPC Closures*, Journal of Bridge Engineering, 23(6), 2018, p.04018028.

[64] Fehling, E., Lorenz, P. and Leutbecher, T., *Experimental Investigations on Anchorage of Rebars in UHPC*, In Proceedings of Hipermat 2012 3rd International Symposium on UHPC and Nanotechnology for High Performance Construction Materials, 2012, pp. 533-540.

[65] Lagier, F., Massicotte, B. and Charron, J.P., *Bond strength of tension lap splice specimens in UHPFRC*, Construction and Building Materials, 93, 2015, pp.84-94.

[66] Zhou, Z. and Qiao, P., *Bond behavior of epoxy-coated rebar in ultra-high performance concrete*, Construction and Building Materials, V. 182, 2018, pp.406-417.

[67] Ronanki, V.S., Aaleti, S. and Valentim, D.B., *Experimental investigation of bond behavior of mild steel reinforcement in UHPC*, Engineering Structures, V. 176, 2018, pp.707-718.

[68] Harajli, M., Hamad, B. and Karam, K., *Bond-slip response of reinforcing bars embedded in plain and fiber concrete*, Journal of Materials in Civil Engineering, 14(6), 2002, pp.503-511.

[69] Mo, Y.L. and Chan, J., *Bond and slip of plain rebars in concrete*, Journal of materials in Civil Engineering, 8(4), 1996, pp.208-211.

[70] Hwang, H. and Park, S.Y., *A study on the flexural behavior of lap-spliced cast-in-place joints under static loading in ultra-high performance concrete bridge deck slabs*, Canadian Journal of Civil Engineering, 41(7), 2014, pp. 615-623.

[71] Eligehausen, R., Popov, E.P. and Bertero, V.V., *Local bond stress-slip relationships of deformed bars under generalized excitations*, Proceedings of the 7th European Conference on Earthquake Engineering. Vol. 4, Athens: Technical Chamber of Greece, 1982, pp. 69-80.

[72] Karsan, I. D. and Jirsa, J. O., *Behavior of concrete under compressive loadings*, Journal of the Structural Division, 1969.

[73] Filippou, F. C., Popov, E. P., Bertero, V. V., *Effects of Bond Deterioration on Hysteretic Behavior of Reinforced Concrete Joints*, Report EERC 83-19, Earthquake Engineering Research Center, University of California, Berkeley, 1983.

[74] Zhao, J. and Sritharan, S., *Modeling of strain penetration effects in fiber-based analysis of reinforced concrete structures*, ACI structural journal, V. 104, No. 2, 2007, p.133.

[75] Al-Jelawy, H. M., *Shifted plastic hinge column connections using grouted sleeves for accelerated bridge construction*, PhD dissertation, University of Central Florida, 2018.

[76] Wehbe, N.I., Saiidi, M.S. and Sanders, D.H., *Seismic performance of rectangular bridge columns with moderate confinement*, ACI Structural Journal, V. 96, No. 2, 1999, pp.248-258.

[77] Ngo, D. and Scordelis, A.C., *Finite element analysis of reinforced concrete beams*, In Journal Proceedings, V. 64, No. 3, March 1967, pp. 152-163.

[78] Wong, P.S., Vecchio, F.J. and Trommels, H., *VecTor2 and FormWorks user's manual*, Department of Civil Engineering, University of Toronto, 2002, pp.54-58.